Development of a Cryogenic Microcalorimeter

by

David Stuart Junkin

A dissertation submitted to the faculty of the University of North Carolina at Chapel Hill in partial fulfillment of the requirements for the degree of Doctor of Philosophy in the Department of Physics & Astronomy.

Chapel Hill

1997

Approved:

A. Champagne, Advisor

D. Haase, Reader

T. Clegg, Reader

J. Engel, Reader

S. Washburn, Reader

©1997
David Stuart Junkin
ALL RIGHTS RESERVED

ABSTRACT

DAVID STUART JUNKIN: Development of a Cryogenic Microcalorimeter
(Under the Direction of A. Champagne)

The motivation for this project has been to measure β-decay using a low background detector which encapsulated the β source (4π coverage). It was realized that the ideal detector for this measurement was a microcalorimeter (a small cryogenic detector consisting of an absorber, thermistor and thermal link). Presently microcalorimeters are an active area of research and development because of possible applications in weak interaction physics, x-ray astronomy and dark matter searches. The development of such a detector requires an interdisciplinary effort involving nuclear physics, solid state physics, electronics, and statistical mechanics. We have designed, constructed and characterized microcalorimeters employing two types of thermistors ($Au_xGe_{(x-1)}$ and P:Si). In the process we constructed a dilution refrigerator, assembled the necessary electronics, and built a data acquisition and analysis system based on networked desktop computers. This stage of the project has concluded by characterizing the performance of the $Au_xGe_{(1-x)}$ based microcalorimeters by measuring αs and low energy γs. The measured energy spectra have been compared to theoretical predictions, and the linearity of the devices has been tested. Future work will permit these devices to be used to measure β spectra.

ACKNOWLEDGMENTS

I would like to thank the students, faculty, and staff at the North Carolina Microelectronics center for their instruction and help; specifically, Tad Grider, Joan O'Sulivan, and Dick Kueen. I am grateful for the instruction and use of the wire bonder that I received from Professor Washburn and his students. The successes of this project has hinged on the $Au_xGe(1-x)$ thermistors which were developed by Professor X. X. Wang and Professor J. Martoff. Their cooperation, and insights into microcalorimetry have been invaluable. I also appreciate all of the assistance provided by the Duke Instrument Shop and TUNL support staff.

I am grateful to the members of my doctoral committee for taking the time and effort to encourage and direct this work. I am especially grateful to my advisor, Professor Champagne, for allowing me to undertake this project; and Professor Haase, whose low temperature expertise has transformed that realm of black magic into a science that I have grown to love.

I am very grateful for the persons that came before me allowing this project to succeed: Tim Murphy for his development of the dilution refrigerator and gas handling system and Chris De Pree for his background work on thermistors, microcalorimeters, and electronics. I am grateful to Mike Seely for his dedication and hard work redesigning the dilution refrigerator.

My deepest and heartfelt thanks are extended to Brian Raichle and Joe Walston for their friendship and camaraderie without which I would not have enjoyed coming to work. They empathized with the failures and celebrated the successes. I am grateful to Brian for his advice and encouragement on long runs (both experimental and recreational). Joe Walston for providing a friendship that has

allowed discussions and discourses on all areas of life. I am also grateful for the LaTeX support and the hours of editing he provided.

To my family for allowing me to discuss and perform physics experiments at home and encouraging me to pursue them elsewhere. Your emotional and physics support has always and continues to be without reservation. To my dear wife, Margaret J. Junkin, thank you for financing, tolerating and understanding my graduate student hours and years with a smile. Your cheerful attitude is what has made life fun.

I thank God for creating such a wonderful and interesting world using just a few fundamental particles and forces and for filling it with all the wonderful people.

David S. Junkin

July 1997

To: $\sum_{i=II}^{III}$ William F. Junkin i

who both showed me the beauty in engineering and problem solving.

CONTENTS

Page

LIST OF TABLES . . . xv

LIST OF FIGURES . . . xvii

Chapter

I. Theory of Cryogenic Microcalorimeters . . . 1

1.1 Background . . . 2

1.2 Energy Resolution . . . 5

1.3 Signal Size . . . 6

1.4 Specific Heat . . . 8

1.5 Thermal Conductivity . . . 9

II. Thermistors . . . 11

2.1 Production of P:Si Wafers . . . 11

2.1.1 PREDICT . . . 12

2.1.2 Mask Production . . . 14

2.1.3 Wafer Production . . . 15

2.2 Resistance versus Temperature Measurements . . . 19

2.2.1 Resistance versus Temperature Data . . . 19

2.3 $Au_xGe_{(1-x)}$ . . . 21

2.3.1 Mask Production . . . 22

2.3.2 Fabrication . . . 22

2.4 Resistance versus Temperature Measurements . . . 24

III. Dilution Refrigerator System . . . 27

3.1 Dilution Refrigerator . . . 27

3.1.1 Cold Plate . . . 28
3.1.2 Condenser . . . 30
3.1.3 Still . . . 30
3.1.4 Heat Exchanger . . . 31
3.1.5 Mixing Chamber . . . 31
3.2 Gas Handling System . . . 33
3.2.1 ^{4}He System . . . 33
3.2.2 ^{3}He System . . . 34
3.3 Thermal Isolation . . . 35
3.4 Specifics of Bolometer Dilution Refrigerator . . . 39
IV. Calorimeter Assembly . . . 43
4.1 Absorber . . . 43
4.2 Weak Thermal Link . . . 45
4.3 Chip Carrier . . . 50
V. Data Acquisition and Analysis . . . 55
5.1 Electronics . . . 55
5.1.1 JFET Preamplifier . . . 57
5.1.2 Differential Preamplifier . . . 59
5.1.3 Differential Amplifier . . . 60
5.2 Data Acquisition . . . 64
5.3 Data Analysis . . . 67
5.4 Software . . . 71
VI. Data . . . 75
6.1 Determining Bias Conditions . . . 76
6.2 Comparison of Analysis Methods . . . 78
6.3 Voltage and Energy Correlation . . . 81
6.3.1 Energy Calibrations from ^{241}Am Photons . . . 82
6.3.2 Energy Calibration from ^{137}Cs γs . . . 83
6.4 Linearity of Microcalorimeter Response . . . 86

6.5 Improving the Resolution 89
VII. Conclusion 91
VIII. Appendix A: Gaussian Fit Routines 93
IX. REFERENCES 99

LIST OF TABLES

2.1 Silicon wafer doping concentration and junction depth 14

2.2 Length to width ratios for the mask patterns. 16

2.3 Ion Implantation Energy and Dosage Specifications 17

3.1 Thermal conduction through the signal leads. 38

4.1 Heat capacities of materials used in microcalorimeters. 45

4.2 The measured thermal conductivity constants for Al at various temperatures. 49

5.1 Noise sources for bias circuitry. 57

6.1 Comparison of the three analysis methods. 81

6.2 α and photon intensities from ^{241}Am relative to an ^{241}Am decay [Fir96, Kno89]. 83

6.3 Energy and voltage peak values (gain = 10251) used for energy calibration. 88

LIST OF FIGURES

1.1 Schematic of microcalorimeter showing the physical setup and the materials typically used for the specific parts. 5

2.1 Predicted phosphorus dopant profiles for silicon wafers. 13

2.2 Overlay of all three mask layers. 15

2.3 Picture of two chip patterns on a P:Si wafer. 18

2.4 Cross section of P:Si thermistor after all production stages. 19

2.5 Resistance versus temperature curves for eleven different samples from 5 different wafers. 20

2.6 Mask used for the patterning the contact pads of the $Au_xGe_{(1-x)}$ Wafers. 23

2.7 Cross section of $Au_xGe_{(1-x)}$ thin film thermistor. 24

2.8 Resistance versus temperature for a thermally anchored $Au_xGe_{(1-x)}$ thermistor. 25

2.9 Resistance versus temperature for $Au_xGe_{(1-x)}$ thermistors. 26

3.1 Schematic of the bolometer dilution refrigerator. 29

3.2 Vapor pressure of ^{3}He and ^{4}He versus temperature. 30

3.3 Phase diagram of ^{3}He/^{4}He as a function of temperature. 32

3.4 The ^{3}He and ^{4}He gas handling system. 34

3.5 Wooden tube to provide physical support between the mixing chamber and still. 35

3.6 Centering ring used to stabilize the mixing chamber. 36

3.7 JFET preamplifier thermal isolation. 37

4.1 Power versus T^4 for Al wires at operating temperatures from 142–191 mK. 47

4.2 Power versus T^4 for Al wires at operating temperatures from 212–305 mK. 48

4.3 Chip carrier used for wirebonding the microcalorimeter. 50

4.4 Vacuum chuck used for wirebonding. 52

4.5 Chip carrier and microcalorimeter setup. 53

5.1 Bias resistor arrangement for the thermistor. 56

5.2 Thévenin's equivalent for the bias circuit. 57

5.3 Biasing and JFET preamplifier. 59

5.4 Differential Preamplifier. 60

5.5 Differential Amplifier. 61

5.6 Variable gain differential amplifier. 62

5.7 Gain versus frequency for the amplifier system. 63

5.8 Voltage noise spectral density 64

5.9 Data acquisition and analysis computer system. 66

5.10 Schematic of a signal data file. 67

5.11 Windowing a voltage sweep of a pulse in the signal file. 69

5.12 Gaussian least squares fit a histogram data file. 70

5.13 The front panel of the master data analysis routine. 72

5.14 The diagram for the master data analysis routine. 73

6.1 The microcalorimeter voltage response and energy resolution due to a 5.5 MeV α–particle versus bias voltage. 77

6.2 Amplified voltage response due to an incident α particle. 78

6.3 Voltage histogram of data analyzed using the *exponential* fit method. 79

6.4 Histogram showing the lower region of the energy spectrum from an open source ^{241}Am. 82

6.5 ^{241}Am voltage spectra which are proportional to energy spectra. . . . 84

6.6 ^{137}Cs and ^{241}Am voltage spectrum acquired in 12.1 hours. 85

6.7 Comparison of predicted and recorded energy spectrum from ^{137}Cs. . . 87

6.8 Log plots of spectrum used for energy calibration from the ^{137}Cs data. 88

6.9 Voltage response of microcalorimeter (gain of 10251) versus energy deposited from the ^{241}Am and ^{137}Cs sources. 89

Chapter 1

Theory of Cryogenic Microcalorimeters

The motivation for this project has been to measure β–decay using a low background detector which encapsulated the β source (4π coverage). It was realized that the ideal detector for this measurement was a microcalorimeter (a small cryogenic detector consisting of an absorber, thermistor and thermal link). Presently microcalorimeters are an active area of research and development because of possible applications in weak interaction physics, x–ray astronomy and dark matter searches. The development of such a detector requires an interdisciplinary effort involving nuclear physics, solid state physics, electronics, and statistical mechanics. We have designed, constructed and characterized microcalorimeters employing two types of thermistors ($Au_xGe_{(x-1)}$ and P:Si). In the process we constructed a dilution refrigerator, assembled the necessary electronics, and built a data acquisition and analysis system based on networked desktop computers. This stage of the project has concluded by characterizing the performance of the $Au_xGe_{(1-x)}$ based microcalorimeters by measuring αs and low energy γs. The measured energy spectra have been compared to theoretical predictions, and the linearity of the devices has been tested. Future work will permit these devices to be used to measure β spectra.

1.1 Background

Dark matter (non-luminous material) was hypothesized as early as 1933 to explain the observed velocity dispersion in clusters of galaxies [Fab85]. In 1974, dark matter began to achieve wide acceptance due to similar velocity observations in spiral and elliptical galaxies [Ree94]. Theoretical justification was provided by models of big bang nucleosynthesis. These models placed constraints, derived from the abundances of the light elements, that could not be supported without the existence of dark baryonic matter [Pra95]. Further evidence that dark matter exists and has been reported by a number of authors [Khl95, Ger95, Fuk88, Bah87a].

The composition of dark matter has been extensively discussed. Some of the predominantly mentioned candidates have been: massive neutrinos, massive compact halo objects, weakly interacting massive particles, and massive, conventional astronomical dark matter [Bah87b, Cal88, Cor93, Man94, Cro96]. Experimental evidence for massive neutrinos was furnished by Simpson in a 1985 article [Sim85]. In this study, the shape of the β-decay spectrum of tritium seemed to reveal the presence of a 3% admixture of neutrinos with $m_\mu c^2 = 17$ keV. Further work followed both supporting and arguing against the existence of such a particle in a variety of different beta decays with a variety of different admixtures. In 1991, there was a reported 1.4 % admixture of 17 keV neutrinos in the β-decay spectrum of ^{14}C [Sur91]. These measurements were made using a germanium detector.

To verify this measurement, an effort was made to measure a β-decay spectrum without the use of a Ge detector which was hypothesized to distort the spectral shape of the earlier measurements. A suitable detector would have a predictable efficiency over the measurement energy range; and should also have a minimal background. In 1987, a system based on detection of particles through a non-ionizing process was proposed [Sad87] which also seemed to meet

the performance criteria for the measurement of the neutrino mass. The detector proposed, a cryogenic detector, measures either the breaking of Cooper pairs in superconductors, or the formation of phonons in crystals. The phonon detectors are called bolometers or microcalorimeters.[1]

The sensors proposed for the development of microcalorimeters were rather diversified and each type presented individual advantages and disadvantages. Superconducting granules are predominantly threshold detectors and do not reveal detailed energy information. They are very sensitive to both changes in the temperature and to changes in the external magnetic field [Kot87]. Superconducting tunnel junctions hold great promise for energy resolution, but require special development methods [Sad87]. Thermistors were also proposed which would measure a temperature change of an absorber. The advantage of thermistors lies in the diversity of the available materials with which to produce thermistors and they can be made using standard microelectronics techniques. This is important in order to allow for further development of an array of detectors. The standard microelectronics techniques could also enable a design with the possibility of integrated preamplifier circuitry [Dep92].

The initial goal of the present work was a measurement of the *beta*-decay spectrum of ^{14}C. There were two reasons for this, one being a check of the 17 keV neutrino hypothesis. Carbon-14 was chosen because of its low endpoint energy. This would allow a measurement of the region of interest (17 ± 1 keV below the endpoint energy) in a reasonable period of time. The second reason for looking at the β-decay spectrum of ^{14}C was to measure the weak magnetism form factor, a term arising from the possible renormilization of the weak interaction vector coupling due to the strong force. This effect was calculated and discussed by various groups [Gar95, Cal76, Jin88, Wu64, DeB97].

[1] Calorimeters were initially used as particle detectors in 1903 by Curie and Laborde [Low88]. Calorimetry experiments were also pivotal in providing evidence for the missing energy in the beta decay of $^{210}RaE_{83}$ (^{210}Bi) by Ellis and Wooster [Wu66].

By 1993, a variety of nuclear beta decays had been studied and the evidence was against the existence of a 17 keV neutrino. Spectrometer-based measurements of ^{37}S were reported to show no evidence for the existence of a 17 keV neutrino [Ber93]. Similar conclusions were reached from studies of ^{107}Pd using a microcalorimeter. [Low93, Dep94]. The 17 keV neutrino issue is considered to be an instrumental artifact and not a manifestation of a non-zero mass neutrino.

However, there are still a number of measurements for which a microcalorimeter is ideally suited. One of these is the previously mentioned measurement of the shape of the ^{14}C beta decay spectrum. These detectors have been shown to be good candidates for low energy X-ray measurements [Kel93], double β-decay measurements [Ale93], and dark matter detectors [Mar93].

A microcalorimeter is composed of three parts: an absorber, a thermistor, and a weak thermal link which is schematically represented in Figure 1.1. When radiation strikes the absorber which is attached to a thermistor, the radiation causes a temperature increase. This temperature change will be measured by the thermistor which will reach thermal equilibrium with the absorber. These two parts will then thermally decay back to the ambient operating temperature through the weak thermal link between the thermistor and a heat sink.

Microcalorimeters have a number of advantages over semiconductor detectors, which are normally used for this kind of measurement. Semiconductor detectors rely on the collection of electron-hole pairs that are created by incident particles. The energy to create one pair is determined by the band gap in the semiconductor, and is of the order of 3 eV for Si detectors. The energy resolution is determined by the number of pairs, but it is limited by thermal losses, as incident particles will deposit some energy in the form of phonons which can not be detected. These devices are also susceptible to charge loss from recombination and trapping. These effects place a statistical limit on the energy resolution. By comparison a microcalorimeter detector relies on the collection of phonons created by incident particles. For a calorimeter operating at 0.1 Kelvin the nominal

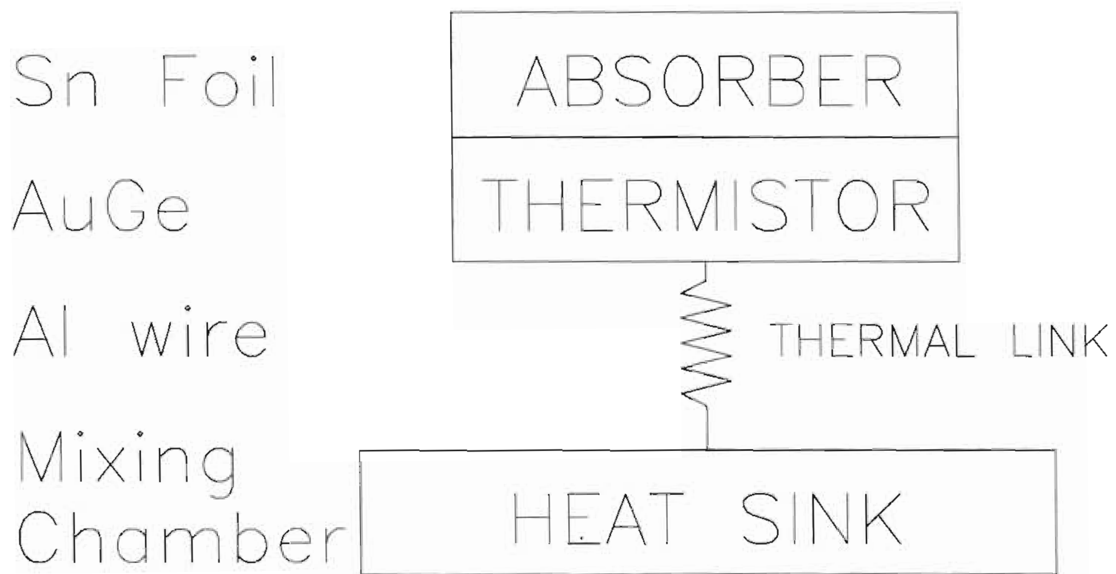

Figure 1.1: Schematic of microcalorimeter showing the physical setup and the materials typically used for the specific parts.

photon energy is E=k_B T $\approx$ 100 μeV, an intrinsic resolution advantage of 10^4 over silicon. If appropriate materials are chosen so that all radiation is quickly thermalized, then all of the deposited radiation will be measured [Low88]. This is independent of whether the incident particle deposits its energy through ionization, photoelectric effect, or nuclear recoil. Because these devices operate at low temperatures, low-temperature electronics are used which have lower input-noise characteristics than traditional room temperature devices [Gon88].

1.2 Energy Resolution

The energy resolution of a microcalorimeter is limited by thermal and electrical noise. The electrical noise is discussed in section 5.1. The thermal noise is due to statistical fluctuations in the temperature of the system. This places a lower limit on the energy resolution of

$$\Delta E = 2.35\xi\sqrt{k_B T^2 C} \tag{1.1}$$

where k_B is Boltzmann's constant, T is the operating temperature of the thermistor, C is the heat capacity of the device, and ξ is a constant that depends on the sensitivity of the thermistor. The constant ξ is on the order of 3 for typical resistive thermistors [Mos84].

Equation 1.1 emphasizes the importance of operating at a low temperature and having a minimal heat capacity. The low temperature requirements can be achieved through the use of a dilution refrigerator which is discussed in section 3. The heat capacity of these devices is reduced by using small devices and through choosing materials with minimal specific heat at the operating temperature.

1.3 Signal Size

The theoretical energy resolution of a microcalorimeter is only realized if a measurement of the energy deposited in the device is made. The energy deposited in the device is related to the temperature by

$$\Delta T = \frac{E}{C_p(T)} \tag{1.2}$$

where E is the energy deposited in the microcalorimeter (thermistor, absorber, and thermal link) and C_p is the heat capacity of the device. For small changes in energy relative to the heat capacity, C_p can be approximated as a constant. Therefore, the change in temperature will be proportional to the energy deposited. However, this is not correct for large amounts of energy and small heat capacities. If there is a significant change in the temperature, the heat capacity can not be assumed to be a constant. Therefore if a significantly large amount of energy is deposited in the microcalorimeter, the temperature response will be less than calculated (assuming that the heat capacity increases with temperature).

For the thermistors used in this work (discussed in section 2) the conduction decreases as the temperature is decreased. The resistance of these devices is

characterized by

$$R(T) = R_0\, exp\left(\frac{T^*}{T}\right)^n \tag{1.3}$$

where R_0 is a constant depending on the resistivity and geometry. T^* is dependent upon the doping concentration and n varies with the conduction method. Thermistors are characterized by the sensitivity α given by

$$\alpha = \frac{d\,ln(R)}{d\,ln(T)} \tag{1.4}$$

which when using the specific resistivity versus temperature relation stated in equation 1.3 is

$$\alpha = n\left(\frac{T}{T^*}\right)^n \tag{1.5}$$

where n is typically $\frac{1}{2}$ and the constant T^* is obtained from the resistance versus temperature curves discussed in section 2.4 and 2.2.

While operating a microcalorimeter, there will be an equilibrium established between the power entering the microcalorimeter via resistive heating and radiation and the part leaving through the thermal link attached to the cold bath. This is stated as

$$G(T - T_0) = \underbrace{I_{bias}^2 R}_{P} + E \tag{1.6}$$

where G is the thermal conductivity of the leads, T_0 is the bath temperature, and I_{bias} is the bias current flowing through the thermistor. The power term (P) will also include external continuous sources of heating but these are negligible compared to the resistive heating. Due to the input power, the operating temperature of the microcalorimeter will be greater than the bath temperature, therefore, an effective operating temperature T_0' can be defined such that

$$G(T_0' - T_0) = P \quad . \tag{1.7}$$

Under operating conditions $P >> E$, and therefore $T_0' \approx T_0$, making this temperature the steady state condition [Low61]. T_0 will also be referred to as the zero energy level or condition.

In order to measure the change in resistance across the thermistor, a voltage is applied through the thermistor and a series bias resistor. The voltage across the thermistor is given by:

$$V = R \times I_{bias} \qquad I_{bias} = \frac{V_{bias}}{R_{bias} + R} \tag{1.8}$$

where R is the resistance of the thermistor; and I_{bias}, V_{bias}, and R_{bias} are the bias current, voltage, and resistors.

From equation 1.2, it is realized that the quantity to be measured in order to determine the energy deposited in the microcalorimeter is the *change* in temperature, instead of the *absolute* temperature. This will correspond to a change in resistance as opposed to the absolute resistance. If the change in resistance is significantly less than the total resistance ($R_{bias} + R$), the bias current is constant. Therefore, the change in voltage across the thermistor is

$$\Delta V = I_{bias} \frac{dR}{dT} \Delta T \tag{1.9}$$

where ΔT is given by equation 1.2. The voltage response can be rewritten as

$$\Delta V = I_{bias} \frac{R}{T} \alpha \frac{E}{C_P} \tag{1.10}$$

1.4 Specific Heat

The specific heat of a material is a measurement of the amount of energy that must be absorbed to reach a given temperature at either a constant pressure (C_P) or at a constant volume (C_V)[2]. The specific heat for a material can be calculated from

$$C_p = C_E + C_{PH} \tag{1.11}$$

which is the sum of the electron and phonon contributions respectively.

[2] $C_P = C_V + 9\kappa\alpha VT$ which can be approximated as $C_P \approx C_V$ for temperatures below $\Theta/2$ (where κ, α, and Θ are the compressibility coefficient, thermal expansion coefficient, and Debye temperature respectively) [Pob96]

This work is limited to the low temperature regime, therefore we will only examine the low temperature limit for the thermal properties of materials. The low temperature region for the two factors will be defined relative to the respective temperature constants. For the phonon portion this is the Debye temperature which is typically on the order of 10^2 K. The electron contribution is defined relative to the Fermi temperature for the electron which is around 10[illegible] K [Kit86].

In most metals, the electronic portion of the specific heat dominates below 1 K which is calculated by assuming a free electron model. This contribution is

$$C_E = 41\frac{T}{T_F} = \gamma T \tag{1.12}$$

where T_F is the Fermi temperature and is typically parameterized by the constant γ, called the Sommerfeld parameter [Kit86, Pob96].

The phonon portion of the specific heat for most materials can be accurately calculated using the Debye model. This model assumes simple modes of vibration of the crystal lattice. The specific heat can then be stated as

$$C_{PH} = 1944\left(\frac{T}{\Theta}\right)^3 \quad \frac{J}{K\ mol} \tag{1.13}$$

where Θ is the Debye temperature for a given material and T is the temperature [Pob96, Ash76, Zem81]. Therefore, if properly chosen materials are used that have heat capacities dominated by the phonon portion, the energy resolution given by equation 1.1 becomes proportional to $\mathbf{T}^{\frac{5}{2}}$ further emphasizing the need for low temperatures.

1.5 Thermal Conductivity

The count rate of these devices is limited by the time required for the energy to leave the thermistor and absorber through the thermal link. This thermal relaxation time (τ) is given by Low [Low61] as

$$\tau = \frac{C_p}{(G - \frac{\alpha}{T}P)} \tag{1.14}$$

where G is the thermal conductivity of the thermal link. In the low power limit τ can be approximated as C_P/G.

Thermal conductivity is a material property that governs the heat flow through the material. This is written as

$$G = \frac{A}{L}\int_{T}^{T_0} \kappa(T)dT \tag{1.15}$$

where A is the cross section, L is the length, and κ is the thermal conductivity coefficient of the link. As is the case with heat capacities, there are two contributing terms to the thermal conductivity coefficients written as

$$\kappa = \kappa_E + \kappa_{PH} \tag{1.16}$$

where κ_E and κ_{PH} are the electron and phonon parts respectively. These coefficients can both be calculated as

$$\kappa_x = \frac{1}{3}C_x v_x \lambda_x \tag{1.17}$$

where C_x is the heat capacity per unit volume, v_x is the velocity of carriers and λ_x is the mean free path. In the low temperature limit, the electronic thermal conductivity coefficient is

$$\kappa_E \propto C_E \propto T \tag{1.18}$$

due to a constant electron velocity, the temperature-independent nature of the mean free path at low temperatures, and the heat capacity as calculated in equation 1.12. An identical argument is made for the phonon thermal conductivity coefficient, yielding

$$\kappa_{PH} \propto C_{PH} \propto T^3 \quad . \tag{1.19}$$

Since we are using a superconducting wire as a thermal link, the dominant contribution to the thermal conductivity will come from the phonon term [Pob96].

Both the thermal conductivity and the heat capacity are functions of T^3, therefore, in the low power limit, there should be no temperature dependence to the thermal relaxation time.

Chapter 2

Thermistors

In order to perform a calorimetry experiment, it is necessary to be able to measure accurately changes in temperature. There are a number of transducers that are capable of operating at low temperatures [Pre93, Boo93, Fio93, Irw96], but this work has concentrated on resistive devices.

Two different thermistor designs were developed for the present work. The first device was a phosphorus doped silicon (P:Si) thermistor similar in concept to those used by other groups [Sta93, Ale88, Lui93]. The second design was a gold germanium Au_xGe_{1-x} thin-film device. The latter thermistor has also been used in a variety of calorimetry experiments [Wan93, Kno93]

2.1 Production of P:Si Wafers

It has been shown [Ros83, Mou74] that when silicon wafers have been lightly doped with phosphorus at the metal-insulator transition and cooled below a few degrees Kelvin, the resistivity of the doped region changes significantly with a change in temperature. Theoretically, the log of the resistivity should be proportional to temperature to the negative $\frac{1}{4}$ power:

$$\rho = a e^{b\,T^{-\frac{1}{4}}} \quad . \tag{2.1}$$

This resistivity relationship is caused by an effect known as variable range hopping (VRH) which describes the tunneling of the current-carrying electrons between the "holes" in the silicon lattice [Mot90]. These holes are produced when the implanted phosphorus atoms displace some of the silicon atoms in the lattice. Therefore, the crucial parameter in the production of this resistive effect is the spacing of the phosphorus atoms. The ideal spacing can be produced by doping the silicon such that there are 3.75×10^{18} phosphorus atoms/cm^3. If the silicon is doped too heavily it will not have as significant change in resistivity (if any) with a change in temperature. Conversely, if it is too lightly doped, the silicon will be an insulator below a few degrees Kelvin.

2.1.1 PREDICT

Ion implantation was used in order to achieve the desired doping of 3.75×10^{18} atoms/cc. In ion implantation, the adjustable parameters are the implantation energy and dosages, not the final doping concentration within the wafer. In order to work backwards from the desired doping to energy and dosage, an experimentally-based program, PREDICT, was used. This program is maintained and calibrated by the North Carolina Microcomputer Center against the wafers produced by their ion implantation processes. PREDICT is used to model what the final dopant concentration will be in a wafer, given the implantation specifications and production process. The program uses the initial wafer resistivity, the energy and dosage of all the ion implantations being made, and the annealing time and temperature to model the dopant concentrations as a function of depth. Since this is not an exact process, a variety of doping sequences were calculated that produced a range of concentrations encompassing the ideal value.

Ten wafers were processed with five different ion implantation energies and doses (See Figures 2.1). Wafers 1 & 2 have the same profile, as do 3 & 4, 5 & 6, 7 & 8, and 9 & 10. The predicted dopant levels and junction depths are shown in table 2.1 with the related depth profiles shown in Figure 2.1.

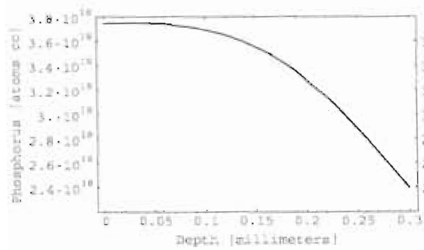

(a) Wafers 1 and 2

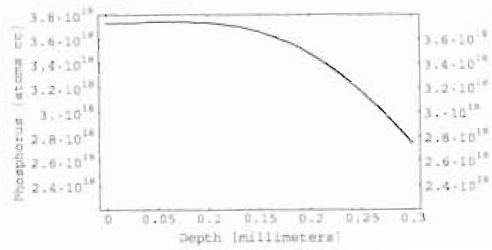

(b) Wafers 3 and 4

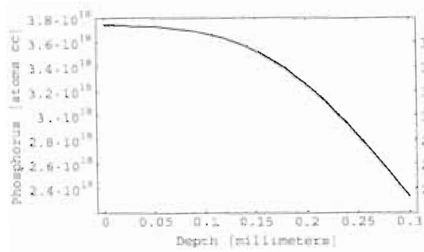

(c) Wafers 5 and 6

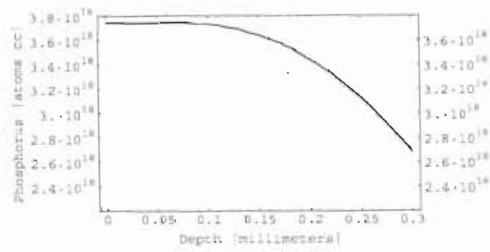

(d) Wafers 7 and 8

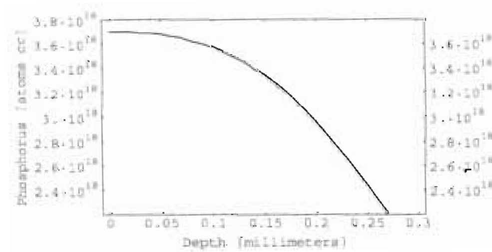

(e) Wafers 9 and 10

Figure 2.1: Predicted phosphorus dopant profiles for silicon wafers.

Wafer Number	Predicted Maximum Dopant Concentration	Predicted Junction Depth
1 & 2	3.75 10^{18}	50 μm
3 & 4	3.73 10^{18}	40 μm
5 & 6	3.74 10^{18}	30 μm
7 & 8	3.74 10^{18}	90 μm
9 & 10	3.70 10^{18}	30 μm

Table 2.1: Silicon wafer doping concentration and junction depth

2.1.2 Mask Production

For an effective microcalorimeter, one desires an operating resistance on the order of a few MΩ. The resistivity is a property of the material and a function of the ion implantation. Suitable thermistors will have an effective junction depth of only about 30–90 microns at operating temperatures. With the junction depth and resistivity known, the resistor geometry can be calculated in terms of the aspect ratio (or number of squares) as in

$$R = \frac{\rho}{depth} \underbrace{\frac{length}{width}}_{number\ of\ squares} . \tag{2.2}$$

The number of squares can then be varied to bracket the desired operating resistance. Once the number of squares and hence the resistor patterns were determined, the patterns were drawn out on a simple computer aided design program, L-EDIT. Contact regions were located at either end of the resistor path. Contact pad patterns were designed so that they would lie directly on top of the contact regions.

Figure 2.2 shows part of the mask layout which was rotated and repeated across the wafer surface. The light gray color shows the contact pad (aluminum or gold) layer (third mask), and the dark gray shows the second mask which is the contact region. The black region shows the actual resistor pattern the regions

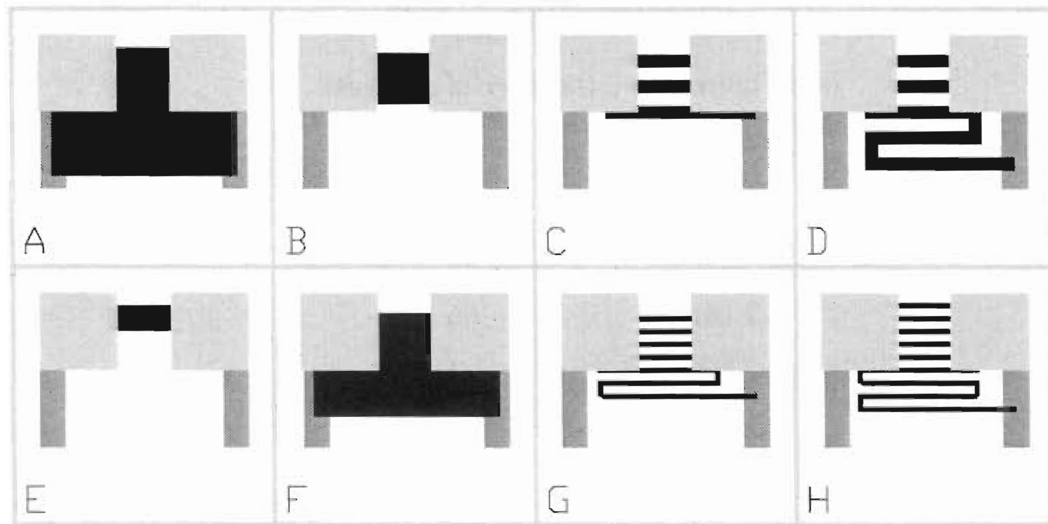

Figure 2.2: Overlay of all three mask layers.

opened up for ion implantation. Table 2.2 shows the length to width ratios for these patterns. The greater the ratio, the greater the resistance of the device.

These three layers of drawings were then transferred individually from the computer design program to a machine designed to produce glass masks. The mask designs were converted to physical glass masks by a machine in which a controlled light source is used to selectively develop the light sensitive film located on the glass plates. The plates were then removed from the controlled light source machine and developed. One glass mask for each layer of the design was produced (three in total).

2.1.3 Wafer Production

Four-inch p type wafers were used as a substrate on which to develop the P:Si thermistors.[3] Initially the wafers were labeled, cleaned and coated with 8000 Å of SiO_2 by baking them at 1000 $°C$ in flowing oxygen. The SiO_2 was needed as a masking layer so that the resistors could be patterned by opening

[3] These were obtained from the North Carolina Microelectronics Center. The wafers were lightly doped with boron to make them p-type.

Pattern (see Figure 2.2)	length/width (number of squares)
2.2 (a)	1.2
2.2 (b)	2.8
2.2 (c)	40
2.2 (d)	65
2.2 (e)	6.5
2.2 (f)	1.4
2.2 (g)	180
2.2 (h)	230

Table 2.2: Length to width ratios for the mask patterns necessary to insure the proper operating resistance.

up regions in this layer for later ion implantation.

The SiO_2 was patterned by photolithographic techniques: The surface of the wafers were first coated with 1.5 μm of photoresist[4]. Then, the photographic mask was aligned above each of the wafers and exposed to UV light. The wafers were then developed,[5] which removed the exposed photoresist, and hard baked. Next, the SiO_2 (in the region opened in the photoresist) was chemically etched with a buffered oxide etchant[6]. Finally, the photoresist was removed and the wafers were cleaned. They were then sent to the Microelectronic Center of North Carolina where they were implanted with phosphorus as was calculated and shown in Table 2.3. The wafers were then re-coated with a thin layer of SiO_2 using diethylsilane at $410°C$ which provided protection for the active region so that another layer could be patterned[7].

[4]Shipley 1400-27 Photoresist

[5]Shipley MF351

[6]NH_4F and HF acid; commonly known as BOE

[7]This and the later processes also served to anneal the wafers.

Wafer Number	Implantation Energy	Dosage
1 & 2	80 KeV	$6.0\ 10^{13}$
	150 KeV	$7.4\ 10^{13}$
3 & 4	30 KeV	$6.5\ 10^{13}$
	180 KeV	$8.4\ 10^{13}$
5 & 6	30 KeV	$6.2\ 10^{13}$
	150 KeV	$7.0\ 10^{13}$
7 & 8	30 KeV	$6.7\ 10^{13}$
	180 KeV	$8.0\ 10^{13}$
9 & 10	25 KeV	$5.3\ 10^{13}$
	110 KeV	$6.1\ 10^{13}$

Table 2.3: Ion Implantation Energy and Dosage Specifications

At that point in the process, the resistive regions were completed and it was only necessary for contact to be made to the patterns. To do this, photolithography was used to again pattern the SiO_2 using the second mask. The exposed areas were etched, exposing regions at either end of the resistor patterns. The wafers were then baked in a gas of pockle[8] at $900°C$. The pockle is used to create a heavily doped phosphorus region with a density of about 10^{20} phosphorus atoms/cc (which is sufficient to conduct at all temperatures) at the ends of the resistors.

After the wafers were removed from the pockle oven and cleaned, they were coated with a metal contact layer. Aluminum was used for the initial batch of wafers but for the second batch, a layer of titanium was laid down before the aluminum layer. The titanium was needed to prevent the aluminum from diffusing through the silicon wafer when annealed, which produced a good metal to pockle region contact. The metal was then patterned with photolithography (using the third mask) and the excess was chemically etched, leaving contact

[8] $POCl_3$ or phosphorus oxychloride

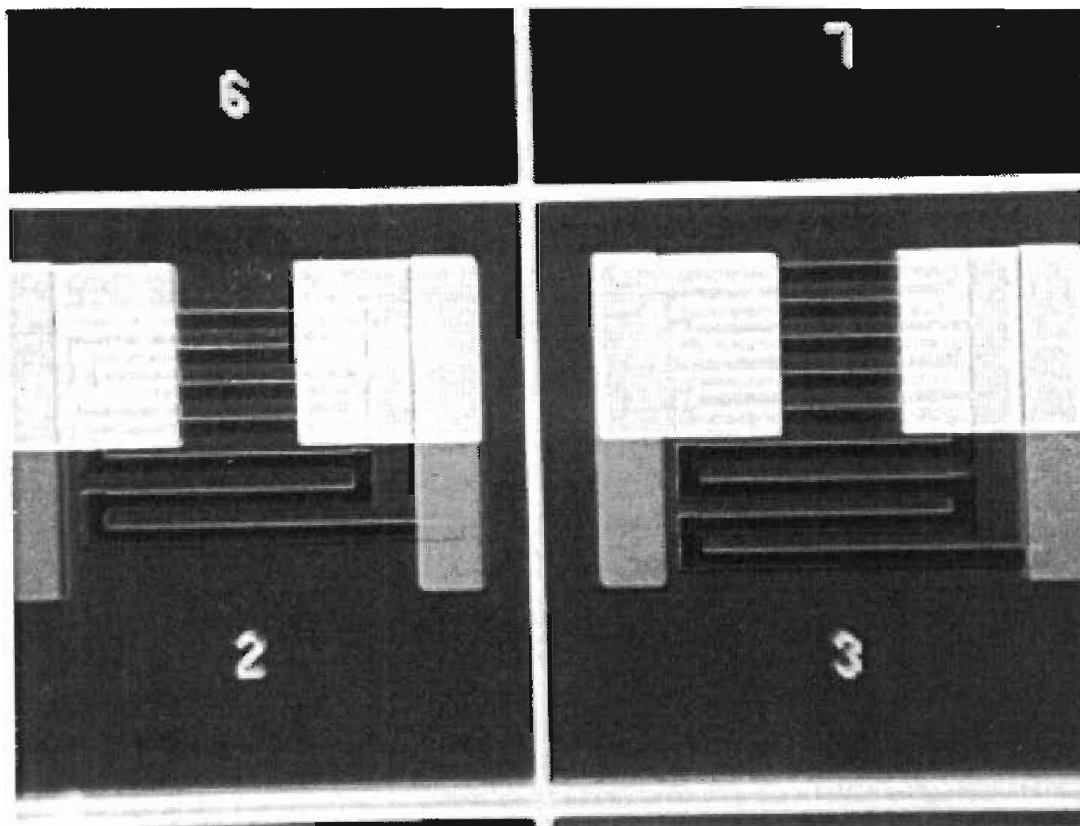

Figure 2.3: Picture of two chip patterns on a P:Si wafer.

pads.

Figure 2.3 shows two of the 5000 resistors on a wafer. The color scheme is identical to that used for the mask as described on page 15. The white metallic pads are only in contact with the pockle region (light gray) as there is a layer of SiO_2 between the resistor patterns and the metal pads. A cross sectional view is shown in Figure 2.4.

The wafers were diced with a manual, diamond-blade dicing machine. The blade makes cuts that were $\approx 50\ \mu m$ wide, which produced chips that were 1.1 mm square. The saw did not fully separate the chips, but scribed them deeply enough so that they could easily be snapped off the wafer for wire bonding and assembly into microcalorimeters.

Figure 2.1: Cross section of P:Si thermistor after all production stages.

2.2 Resistance versus Temperature Measurements

The Si chips were epoxied to a leadless chip carrier with silver epoxy. This provided physical support and thermal anchoring for the chips. The chips were then wire bonded with 0.025 mm (1 mil) Au wire from the chip to the carrier. The carrier was plugged into a sockets on the refrigerator cold finger and on a dipping stick for dip tests in liquid nitrogen (LN) at 77 K and LHe at 4.2 K.

The resistance was then measured with an electrometer[9] at room temperature (≈ 300 K) and a conductance bridge with a maximum excitation energy of 30 $\mu Volts$.

2.2.1 Resistance versus Temperature Data

For optimally doped devices, the resistance versus temperature (RT) curves should follow equation 2.1 at low temperatures. For dopant values differing from the optimal and for temperatures above LHe, one would expect the resistivity to reproduce the values shown by Rosembaum [Ros83]. Above 10 K, the resistivity is not sensitive to small deviations in the phosphorus concentration. For this reason, the effective junction depth for these devices will be on the order of 0.2 mm (as can be seen from the predictions shown in Figure 2.1). In this

[9] Keithley 614 Electrometer

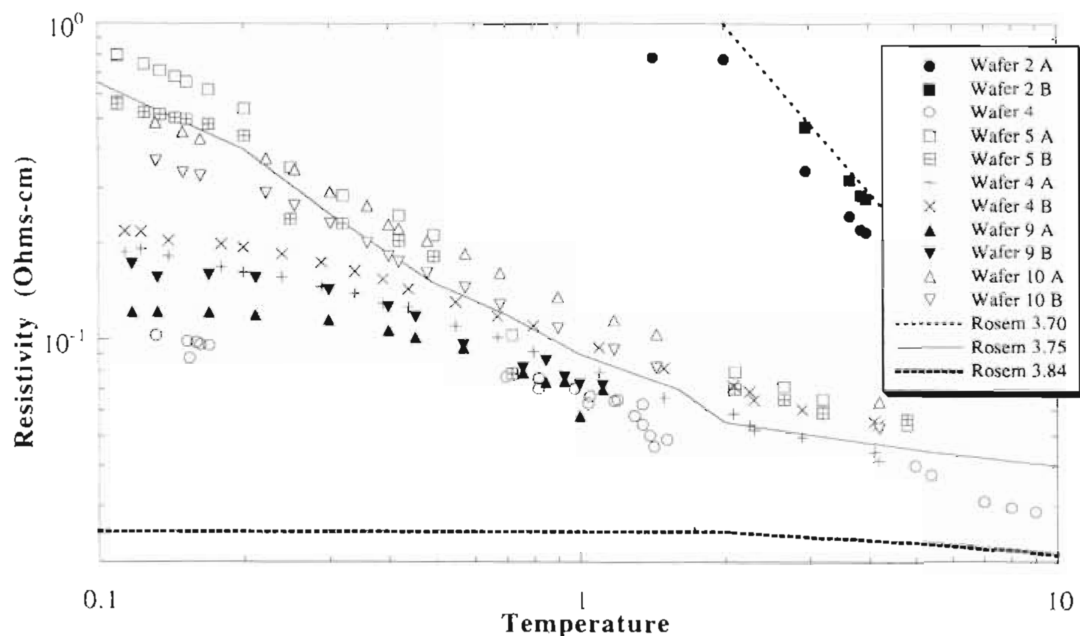

Figure 2.5: Resistance versus temperature curves for eleven different samples from 5 different wafers.

temperature regime, a 20% variation of the dopant concentration from ideal will still contribute nominally the same resistance, and even regions that are significantly under-doped will contribute to the resistance. By contrast, below 1 K a decrease in doping concentration around the critical concentration of as little as 2% will cause the underdoped region to become an insulator and devices that are overdoped by 2% will have metallic behavior with little or no temperature dependence to the resistivity. Since all slightly underdoped regions are insulators in the low temperature regime, they do not contribute to the total resistance. This will be manifested as a change in the effective junction depth. The effective junction depth is significant because the resistance is measured, not the resistivity. Since the resistance is inversely proportional to the junction depth, a decrease in junction depth will mimic an increase in the resistivity.[10] For this reason, RT curves measured above 1 K are not directly indicative of

[10] $R = \rho\frac{l}{A} = \rho\frac{l}{effective\ junction\ depth \times width}$

the doping concentration. Therefore, in order to accurately measure the temperature dependence of the thermistors, RT curves were measured below 1 K, where the effective junction depth is essentially constant. The results are shown in Figure 2.5. As stated above, these curves are not true resistivity curves, but are instead resistance divided by the number of squares which contributes to the resistivity only if the junction depth is a constant (see equation 2.2).

There are three important pieces of information to be gleaned from this plot. Wafers 9 and 10, which were both doped at the same energy and dosages, differ greatly in their resistivity curves. Secondly, samples taken from the same wafer have different curves. Finally, there is no correlation between the predicted dopant level and the measured dopant level as deduced from the measured RT curves. This implies that the ion implantation process employed is neither accurate nor precise. Similar problems with P:Si thermistors have been realized by a variety of other groups [Mar96, McC93, Lui93, Boo96]. Proposed solutions to these problems have included boron doping and additional annealing. Owing to the lack of predictability of these chips, it was found necessary to resort to a more reliable and predictable thermistor.

2.3 $Au_xGe_{(1-x)}$

A number of investigators have shown that the resistance of a Au-Ge mixture in the mK temperature regime has a strong dependence on temperature [Dod81, Chi86]. In principle, these devices are more reliable and are also easier to produce than implanted P:Si thermistors. Further documentation on the development of $Au_xGe_{(1-x)}$ devices used in this work is available from Wang [Wan95].

At low temperatures the thermal conductivity of $Au_xGe_{(1-x)}$ thermistors is dominated by VRH (as discussed in section 2.1). The impurities are produced by the Au atoms that occupy sites within the Ge lattice. This produces a resistance

versus temperature relationship of the form

$$R = \rho_o \frac{length}{width\ thickness}\ exp\left(\frac{T^*}{T}\right)^{\frac{1}{2}} \quad . \tag{2.3}$$

where T^* is a function of the Au concentration: T is the device operating temperature; the length and area are both determined by the device geometry: and ρ is very loosely dependent on the Au concentration. and is typically on the order of one Ω-cm in the concentration regime where VRH is the dominant effect.

2.3.1 Mask Production

Since the resistivity of the $Au_xGe_{(1-x)}$ film is different from that for P:Si wafers. it was necessary to form patterns that had a different numbers of squares than those developed for the P:Si. Patterns previously developed were used to produce devices that were six by six millimeters. a size that would introduce an unacceptably large heat capacity. New masks were developed for the production of 1 mm^2 devices.

To produce a thermistor, a $Au_xGe_{(1-x)}$ film is first uniformly evaporated on a substrate. On this surface. a film of Au is deposited. The Au is the only layer requiring a pattern. Any area that does not have a Au contact will only conduct through the $Au_xGe_{(1-x)}$ film and therefore the area/length ratio will be determined by the area not covered by the contact pads. The $Au_xGe_{(1-x)}$ film made by this process is 2000 Å thick. A range of masks were fabricated in order to produce the desired resistivity. The mask patterns are shown in Figure 2.6. These patterns range from 5.4 to .0023 squares (as defined in equation 2.2).

2.3.2 Fabrication

$Au_xGe_{(1-x)}$ thermistors are also made using normal microprocessing techniques. but they require only one photolithography cycle. Overall. they require significantly fewer steps than the P:Si devices.

Figure 2.6: Mask used for the patterning the contact pads of the $Au_xGe_{(1-x)}$ Wafers. The dark areas represent the gold pads and the rest of the area will be the resistive region.

The resistive region is a thin film which is grown on the surface of a substrate. High-purity 5 cm (two inch) Si wafers were cleaned, polished and placed into an evaporator. At atmospheric pressure, Au and Ge evaporate at $1100°C$ and $1050°C$ respectively. In our case, the Au and Ge were evaporated onto the surface of the wafer at a pressure below 10^{-5} torr so that the two elements would evaporate simultaneously (within the normal fluctuations in heating). The evaporation rate was maintained between 50 to 60 Å/sec to produce a film of 2000 ± 200 Å [Wan95].

Afterwards, without breaking vacuum, a 600 ± 400 Å layer of Au was deposited on the surface of the wafer, covering the $Au_xGe_{(1-x)}$ film. The devices were slowly cooled and stored at $50°C$ to $60°C$ for 10 to 12 hours. The devices were then patterned with photolithography[11] through a process similar to that described in section 2.1.3. As there was only one mask and one pattern, it was

[11] Shipley Microdeposit S1813 Photoresist, Shipley Microdeposit 351 Developer and Shipley Microdeposit Remover 1165 were used in this process.

Figure 2.7: Cross section of $Au_xGe_{(1-x)}$ thin film thermistor.

not necessary to align the mask. The exposed and developed wafers were then etched using an ammonium iodide-based etchant which removed Au, leaving two contact pads, but did not attack the underlying $Au_xGe_{(1-x)}$ [Wan95].

In order to use these devices it was necessary to dice them. The dicing process uses ionized-tap water as a cooling medium which flows over the surface of the wafer during the dicing process. Some of the thermistors' room temperature resistances were found to be significantly higher after the dicing process compared with their initial value. From this, it was realized that the water was destroying the film and it was therefore necessary to protect the film by coating the surface. A 1000 Å thick layer of photoresist[12] was spun onto the surface prior to dicing. The wafers were diced as quickly as permitted in order to limit the amount of exposure time to the water. After dicing, the photoresist was stripped off and the wafers were then separated into individual chips for wire bonding and mounting.

2.4 Resistance versus Temperature Measurements

This measurement was made with the devices epoxied to a metallic surface in good thermal contact with the mixing chamber. This enabled the $Au_xGe_{(1-x)}$ thermistors to be calibrated using the commercial standard thermistor. The

[12]Shipley Microdeposit S1813

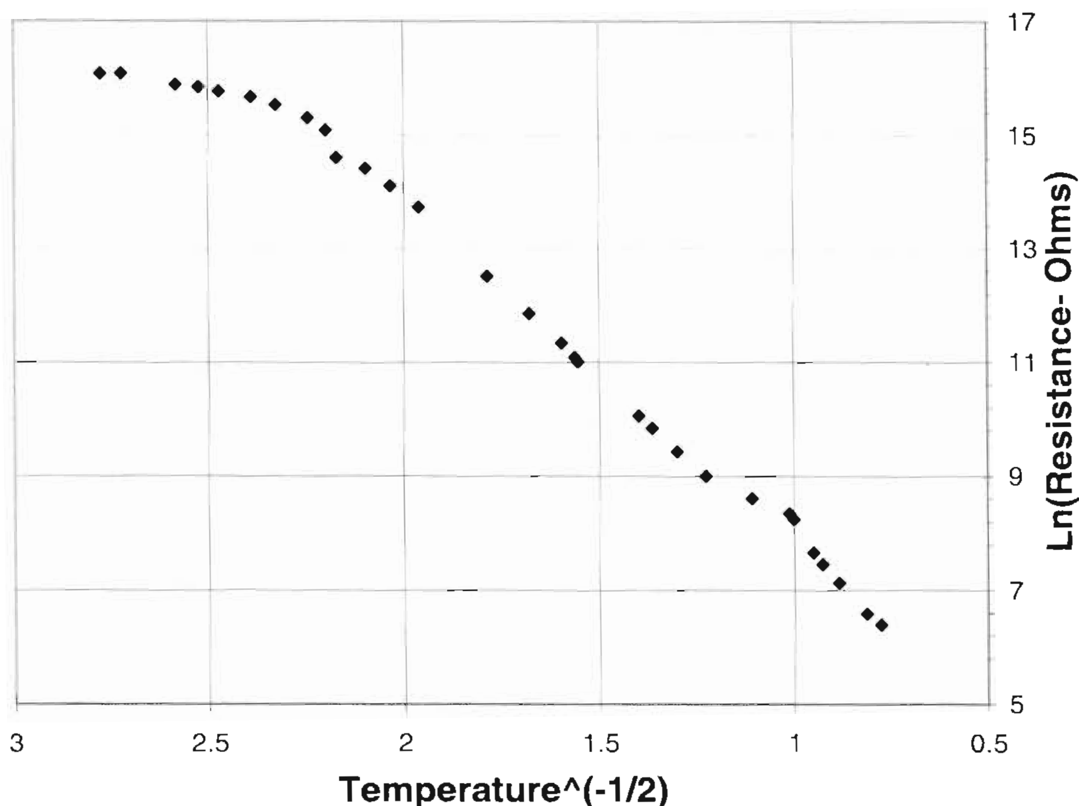

Figure 2.8: Resistance versus temperature for a thermally anchored $Au_xGe_{(1-x)}$ thermistor. The natural log of the resistance is plotted versus temperature to the $-\frac{1}{2}$ power such that the square of the slope of the line equals $\sqrt{T^*}$.

resistance versus temperature curve for a $Au_xGe_{(1-x)}$ thin film thermistors is shown in Figure 2.8. In this case, T^* has a value of 35 K which is useable, but not ideal as this produces a device with a sensitivity of ≈ 6 at operating temperatures. The desired sensitivity is between 3 and 4. Similar RT curves were also been measured through a cycle of five successive cool downs. These are shown in Figure 2.9 and display good reproducibility with no significant shifts. Because of the reproducibility and the predictability of these RT curves, the $Au_xGe_{(1-x)}$ devices are reliable thermistors for calorimetry work.

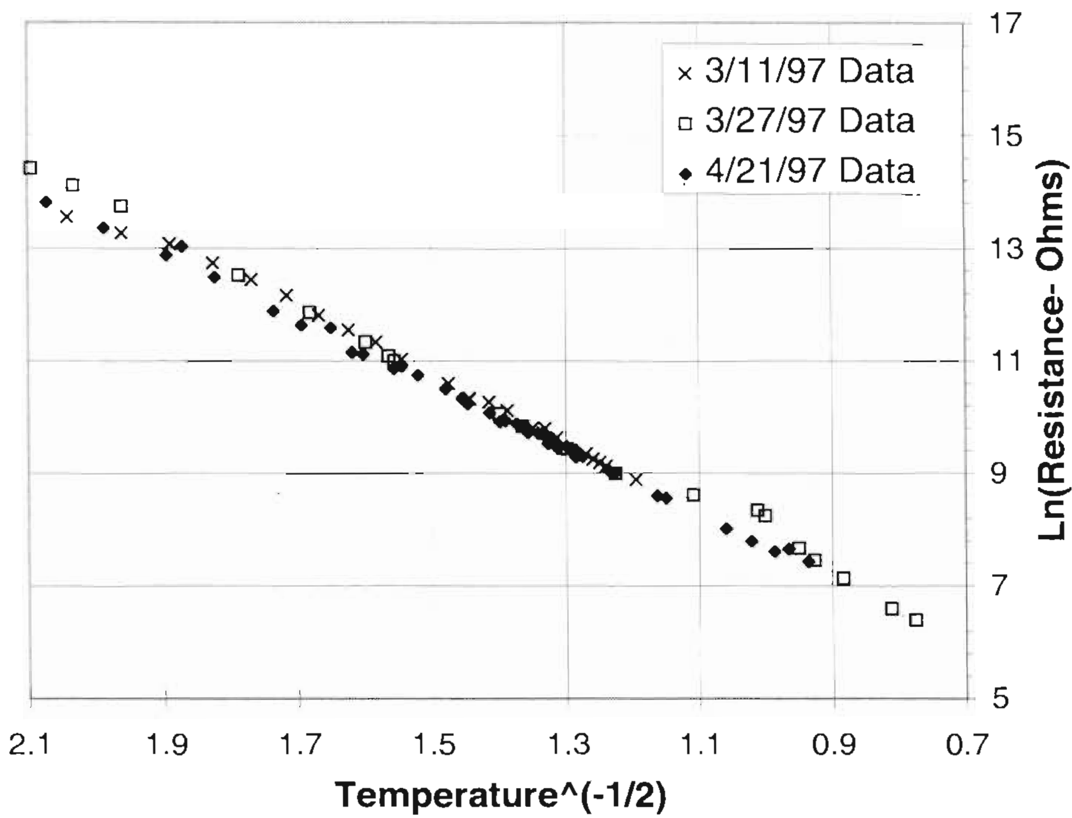

Figure 2.9: Resistance versus temperature for $Au_xGe_{(1-x)}$ thermistors. These devices were only weakly thermally linked to the mixing chamber as is needed for a functional microcalorimeter.

Chapter 3

Dilution Refrigerator System

For our experiment, a small dilution refrigerator was constructed. The specifications for this refrigerator were two-fold: one, an operating temperature near 100 mK and two, the capability to cool down quickly and easily from room temperature to its base temperature, and then return to room temperature again [Mur93]. The operation of our dilution refrigerator will be described in three parts: the dilution refrigerator itself, room temperature gas handling system that powers this refrigerator, followed by a discussion of the thermal isolation and shielding issues inside the vacuum can and other specifics of this system.

3.1 Dilution Refrigerator

Dilution refrigerators have been used since 1965 for applications requiring continuous cooling in the temperature range from 5 to 300 millikelvin. The operating principle was first proposed by London in 1951, who realized that heat could be removed from a system by using the properties of a ^{3}He/^{4}He mixture [Lon74].

The general discussion of a dilution refrigerator system will be presented from room temperature to the coldest portion of the refrigerator where the experimental area is attached. This method presents the individual elements as cooling stages. Each stage provides additional cooling which is required to reach

the base operating temperature. The cooling process used by dilution refrigerators is displayed in Figure 3.1. All of the elements showed are used to cool the ^{3}He/^{4}He gas mixture (the "mash") from a room temperature gas to a liquid in the bottom of the refrigerator. A copper cold finger is attached to the bottom, coldest, element of the refrigerator (the mixing chamber) to provide an area for the experimental setup.

3.1.1 Cold Plate

The first cooling element in the refrigerator is the cold plate which uses the latent heat of evaporation of liquid helium (LHe)[13] to provide cooling. The boiling point of LHe can be reduced by lowering the pressure above the surface of the liquid [Wil67]. As is shown in Figure 3.2, when the pressure is lowered, it is easier for the LHe molecules to leave the liquid and enter the gas phase. As additional pumping removes the gaseous He, the vapor pressure of the liquid will eventually reach equilibrium with the gas.[14]

Our microcalorimeter dilution refrigerator uses a continuously-filled, small evaporator type cold plate which is located inside the vacuum can. The cold plate is filled through a capillary from the external LHe bath in the cryostat [DeL71]. With a small mechanical pump removing the He gas, the cold plate operates at approximately 1.2 K.

[13] unless specifically stated otherwise, liquid helium will refer to commercially available liquid ^{4}He.

[14] The vapor pressure of all cryogenic liquids decreases with temperature. Due to this relationship, an additional heat load is applied to the system, the temperature of the cold plate increases. This in turn, increases the amount of helium entering the gas phase which provides additional cooling.

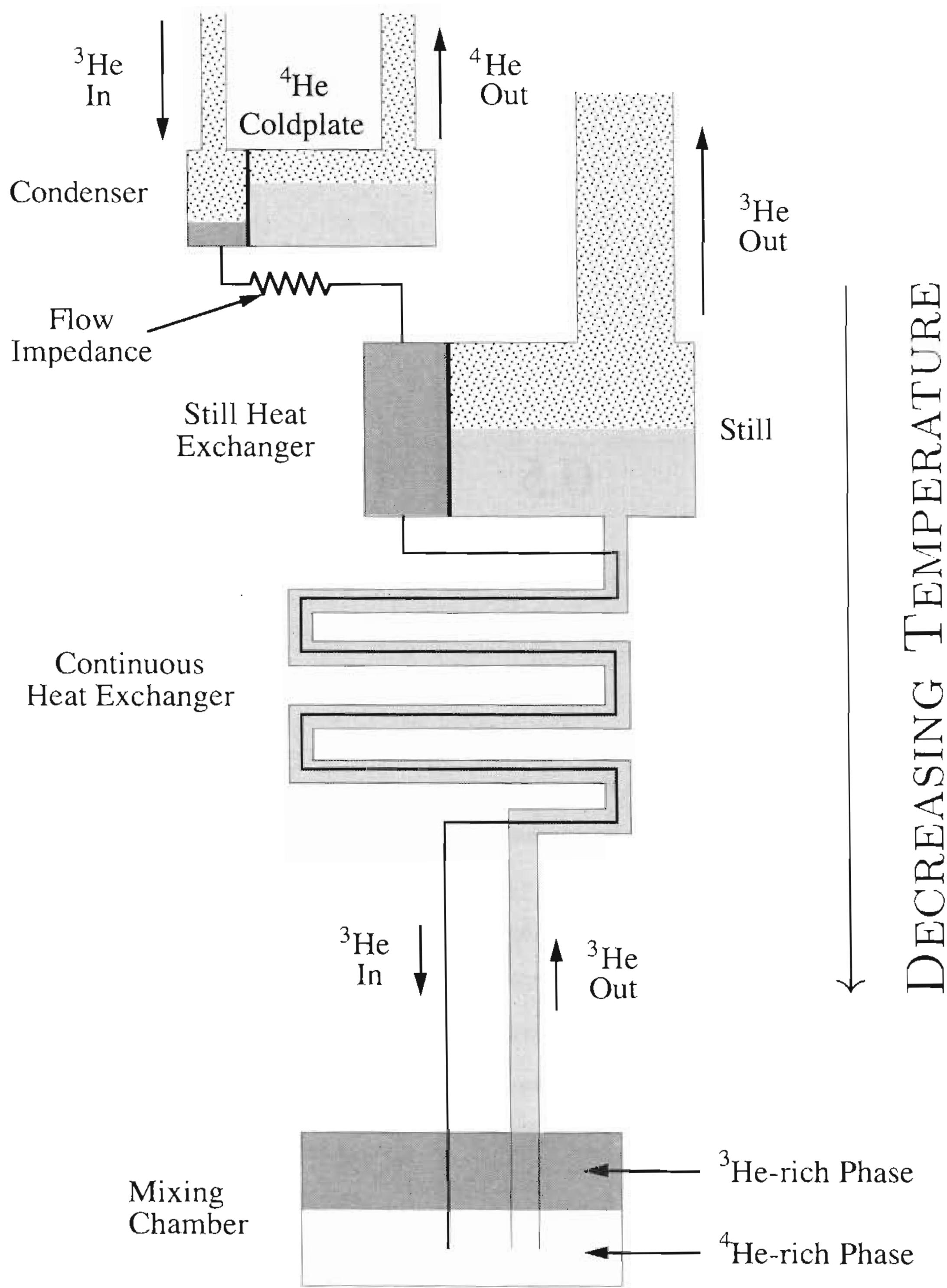

Figure 3.1: Schematic of the bolometer dilution refrigerator.

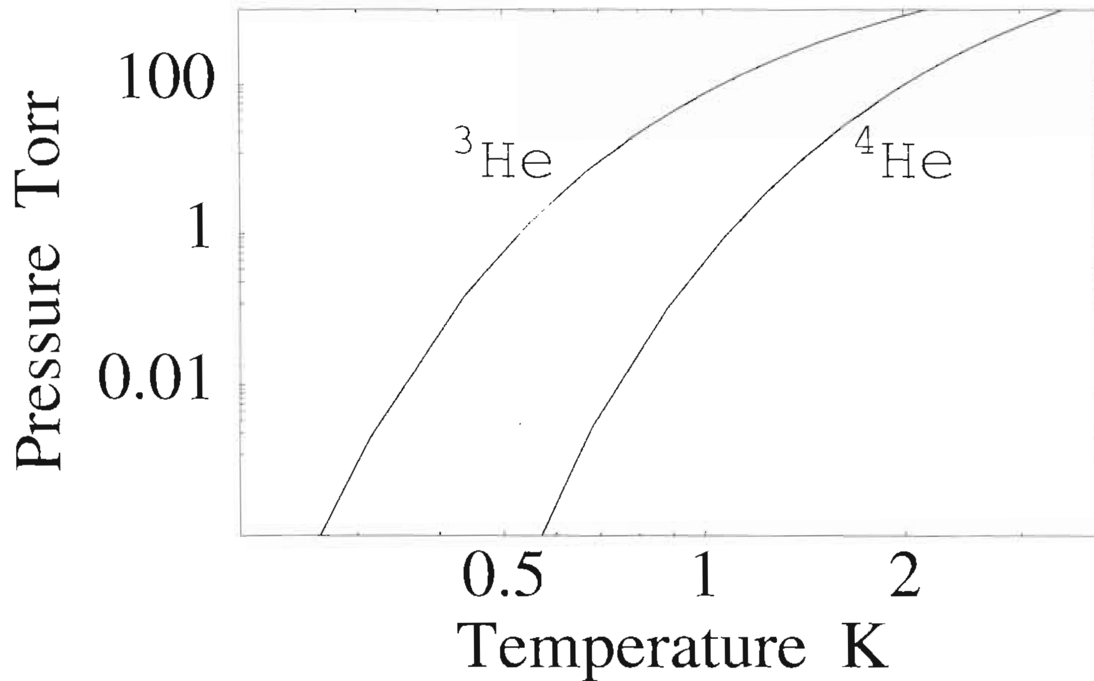

Figure 3.2: Vapor pressure of ^{3}He and ^{4}He versus temperature.

3.1.2 Condenser

The next cooling element is the condenser, which is thermally anchored to the cold plate. Directly following the condenser is a flow impedance which regulates the recirculation rate of the dilution refrigerator. The mash condenses from a gas to a liquid on the high pressure inlet side of the impedance and is forced to the low pressure side providing for additional cooling, via the Joule-Thompson effect. The ^{3}He leaving the condenser will be at its vapor pressure as determined by the cold plate operating temperature [And70].

3.1.3 Still

The still is a copper can located below the cold plate. It is cooled to about 500 mK by virtue of the latent heat required to vaporize ^{3}He. At this temperature, the vapor pressure of the ^{3}He is approximately 10^5 times greater than that of the ^{4}He [Lou74]. Therefore, the ^{3}He is preferentially pumped off by the recirculating

pump (which is often referred to as the ^{3}He pump).

With a uniform pumping rate supplied by the recirculating pump, the actual base temperature of the still was 350 mK. This temperature limit is reached because the vapor pressure of the ^{3}He decreases exponentially with temperature while the latent heat of vaporization is approximately constant [Bet89]. This allows the still to reach easily a stable equilibrium below the desired operating temperature. To raise the temperature of the still, which in turn increases the recirculation rate, additional heat is applied by using a resistive heater.

At the still operating temperature, the ^{4}He is in its superfluid state(He II). Since only ^{3}He provides the cooling, any ^{4}He that is recirculated is an additional heat load to the entire system. To reduce the flow of the superfluid film out of the still, the still is pumped through a small hole. This orifice is polished to present a minimal surface area, thereby limiting the superfluid flow [Pob96].

3.1.4 Heat Exchanger

The still heat exchanger is in direct contact with the still. The incoming mash is cooled to the still temperature before being introduced to the main heat exchanger. This main heat exchanger then cools the mash from the still temperature to that of the mixing chamber by thermal conduction between the ^{3}He rich, entering mash and the dilute mash leaving the mixing chamber (see section 3.1.5). This is usually either a continuous device or a few discrete heat exchangers connected with a single continuous heat exchanger. The microcalorimeter dilution refrigerator has a one meter long continuous heat exchanger. It is composed of two coiled concentric counterflowing tubes in a Linde pattern [Whi79].

3.1.5 Mixing Chamber

The mixing chamber operates at temperatures below 500 mK where the mash separates into two distinct phases. These two phases are called the dilute and

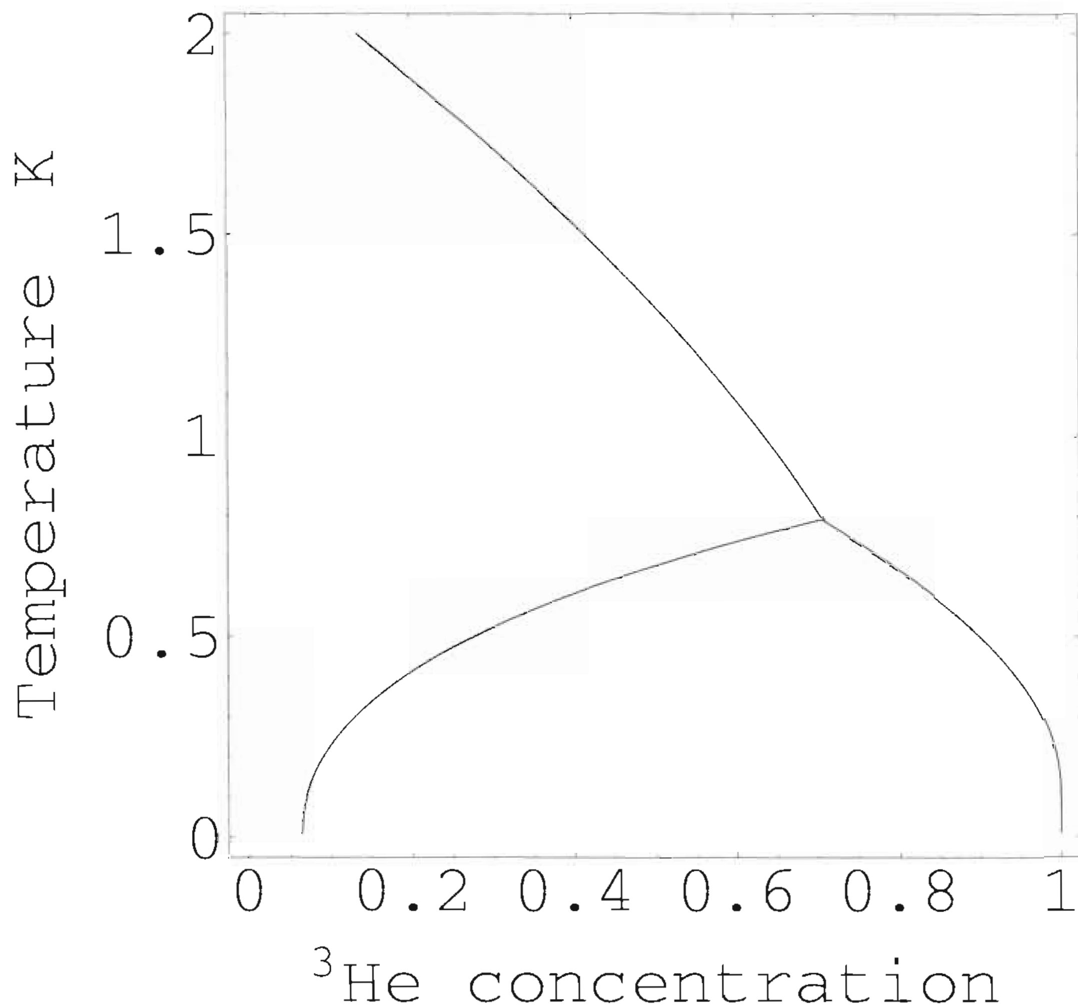

Figure 3.3: Phase diagram of ^{3}He/^{4}He as a function of temperature.

rich phases of ^{3}He. The dilute mixture consists of approximately 7 % ^{3}He and the balance ^{4}He. The rich mixture is 99.9 % ^{3}He with the rest being ^{4}He. The ratio of ^{3}He to ^{4}He is temperature dependent, and approaches a zero temperature value of 6.4 % as can be seen in Figure 3.3 [Bet76, Lou74]. Since this ratio is non-zero at all temperatures, this phase separation can be used as a tool to gain further cooling.

The ^{3}He moves across the phase boundary because of the osmotic pressure difference between the two phases. As the ^{3}He moves from the rich to the dilute

phase, it absorbs an amount of energy equal to the difference between the latent heat of ^{3}He in the two phases. This will cool the mixing chamber until the chemical potentials of the two phases have reached equilibrium [Pob96]. The dilute phase of the mixing chamber is directly connected through the heat exchanger to the still in which ^{3}He is removed (discussed in section 3.1.3). Since ^{3}He is preferentially recirculated through the system it has to be re-introduced into the mixing chamber to prevent the depletion of the concentrated mixture.

3.2 Gas Handling System

The gas handling system is composed of two separate systems, both shown in Figure 3.4. The first system is the ^{4}He system. The second system recirculates the mash. The two systems are independent in normal operation. The only time the two systems are connected is during testing and leak chasing.

The majority of the system is composed of 0.64 cm (1/4 inch) stainless steel tubing. There are exceptions to this for the pump inlet lines where pumping speed is a consideration and for various refrigerator components that need to be electrically isolated. The design and construction of this system was documented by Murphy [Mur93].

3.2.1 ^{4}He System

The ^{4}He gas handling system has a single roughing pump connected directly to the cold plate. The back of the pump is vented directly to atmosphere. This pump does not have to be hermetically sealed as the ^{4}He is not recycled. It has a valve to allow for the cold plate to be purged externally with ^{4}He gas during cool down.

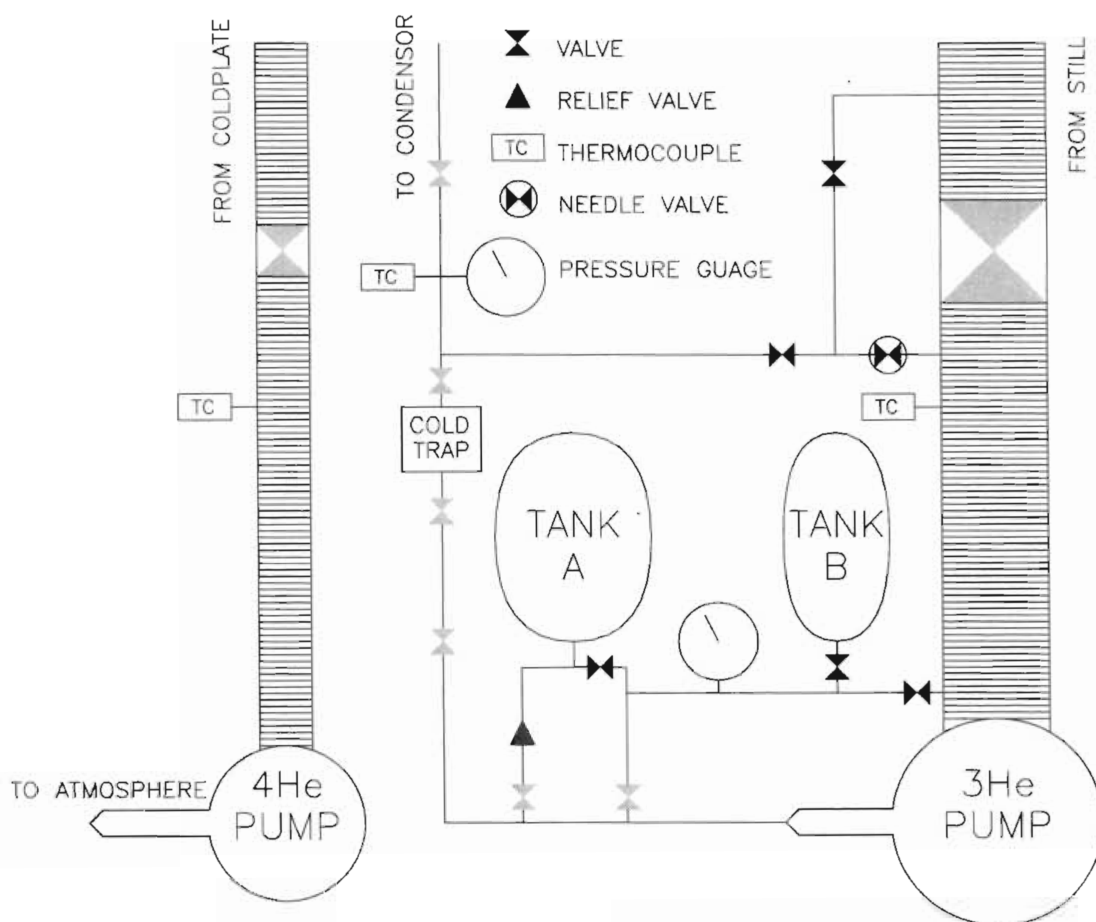

Figure 3.4: The ^{3}He and ^{4}He gas handling system. The gray valves are typically open while the mash is recirculating through the dilution refrigerator.

3.2.2 ^{3}He System

The dominant portion of the gas handling system is for manipulating and circulating the mash. The pump associated with this system is a hermetically sealed roughing pump that is connected to the still. During normal operation, this pump recirculates ^{3}He primarily. The back of this pump is attached to two tanks for storing the mash while the refrigerator is not operating.

The other significant piece of the gas handling system is the cold trap through which the mash is circulated before it is introduced into the refrigerator. This is a charcoal filled trap that is capable of condensing out most non-helium impurities to prevent them from clogging the refrigerator. It has been found that

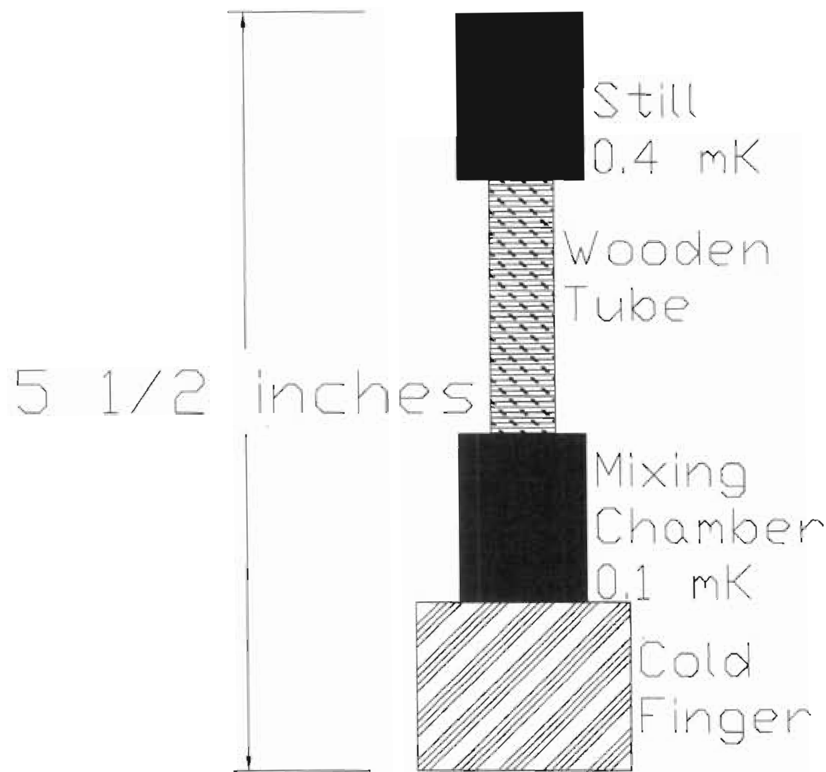

Figure 3.5: Wooden tube to provide physical support between the mixing chamber and still.

it is necessary to filter the output from the trap to prevent charcoal dust from destroying the valve seals.

3.3 Thermal Isolation

Since the parts of the dilution refrigerator are operating at different temperatures, it is necessary to thermally separate the individual components. Hard wood has been shown to have a very low thermal conductivity at our operating temperatures [Wag94]. Therefore, the physical support for the mixing chamber is provided by small wooden rods as shown in Figure 3.5. A 1.27 cm (half inch) wooden tube provides the support from the still to the mixing chamber.

A centering device shown in Figure 3.6 was added to physically stabilize the mixing chamber and to reduce microphonics without increasing the thermal load

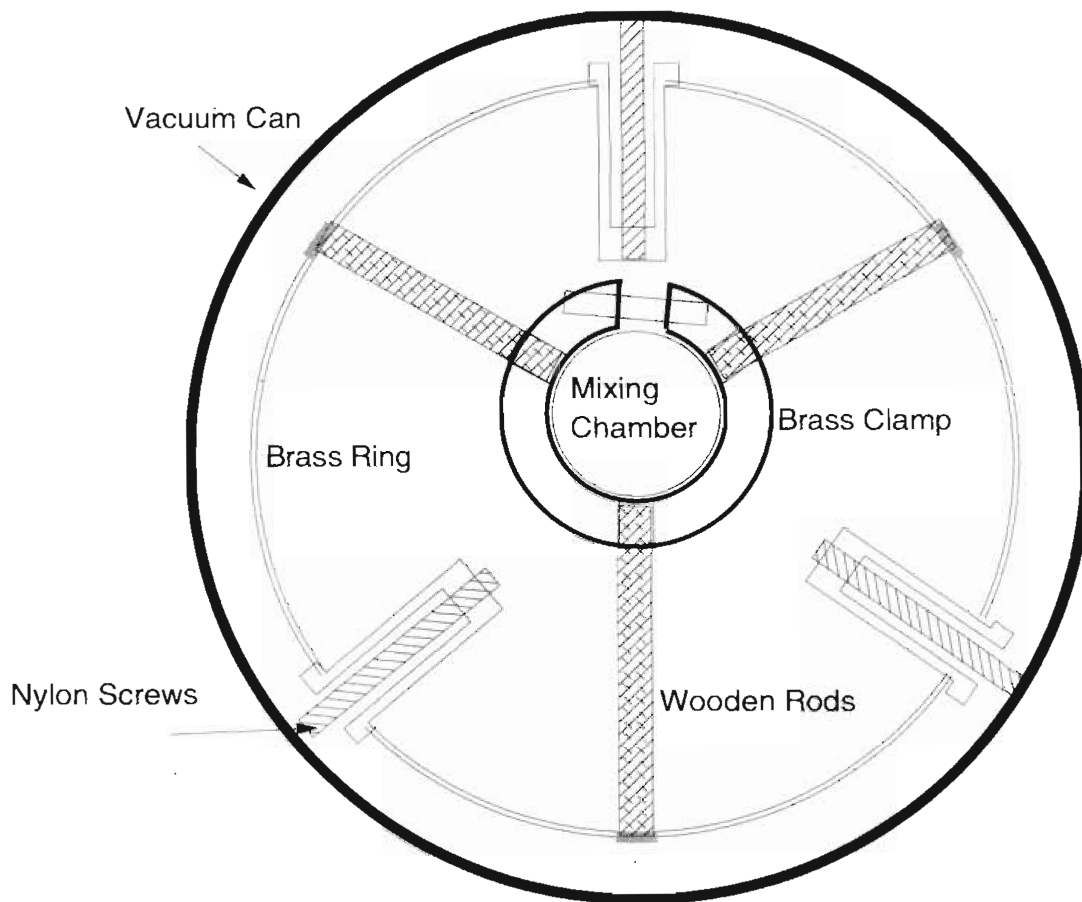

Figure 3.6: Centering ring used to stabilize the mixing chamber.

to the refrigerator. This allows the refrigerator to reach a lower, more stable base temperature, and reduces the measured noise of the microcalorimeter. This design was proposed and discussed by Henderson [Hen71]. The centering ring was secured to the mixing chamber by a brass clamp. The clamp was connected to an intermediate brass ring anchored at the still's operating temperature using three 0.48 cm (3/16 inch) diameter hard wood rods. The support between the vacuum can and the intermediate ring was made using three sets of Delrin tubes and nylon screws.

The JFET preamplifier electronics are operated at 100 Kelvin and are required to be located physically close to the microcalorimeter (located on the cold finger of the mixing chamber). The JFET preamplifier is placed in a cop-

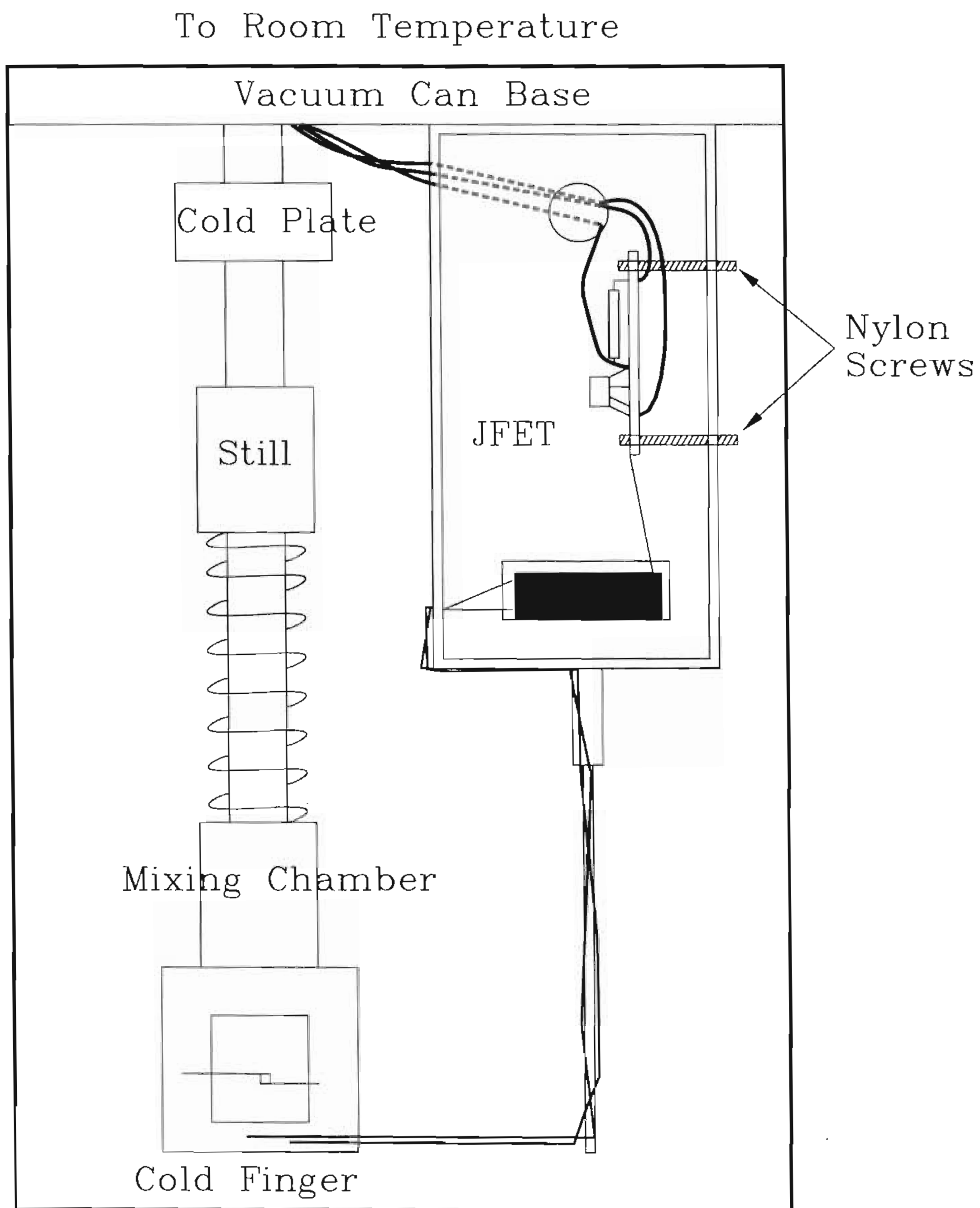

Figure 3.7: JFET preamplifier thermal isolation.

Material[15]	$\dot{Q}$ ($\frac{W}{K}$)	Temperature Range (K)
NbTi wire	$5.3\ 10^{-12}\ T^{2}\ \Delta T$	0.5 0.13
Brass wire	$1.9\ 10^{-7}\ T\ \Delta T$	0.13
Stycast	$1.25\ 10^{-1}\ T^{2}\ \Delta T$	0.13

Table 3.1: Thermal conduction through the signal leads between the JFET and Mixing chamber.

per box that is thermally anchored to the base of the vacuum can at 1.2 K. All holes out of the JFET box were covered to prevent radiative heating of the microcalorimeter. Micro-coax leads from the pre-amp to room temperature are shielded with foil and thermally anchored on the vacuum can base.

The entire JFET preamplifier board is thermally isolated from the preamplifier box by nylon screws as shown in Figure 3.7. The box is screwed down to the vacuum can to insure that it sits at ambient temperature. All leads to and from the board are thermally anchored and chosen for their minimal thermal conductivity. The leads from the JFET gates to the microcalorimeter are cooled through a series of thermal anchors [Hus70]. The first anchor is created by epoxying small resistive wires to a brass plate with Stycast [Ols93]. The brass plate is secured to the interior walls of the JFET box. The resistive wire connects to NbTi superconducting wire using a crimp connection. The NbTi wires are varnished to a rod which is maintained at the still temperature. From the rod, the wires are connected to the cold finger. On the cold finger, the wires are connected to a second set of resistive leads that are epoxied to a brass plate at the mixing chamber temperature before being connected to the microcalorimeter chip carrier.

To calculate the heat introduced to the mixing chamber and microcalorimeter system, the heat flow along the NbTi superconducting wire and brass wires in the thermal shunts is shown in Table 3.1. The energy is removed from the wires

[15] Thermal conductivity values are compiled by Pobell [Pob96].

through the Stycast epoxy attaching the brass wires to the brass plates anchored to the mixing chamber.

The entire cryostat is placed in a wooden box and secured with sandbags. The box is placed on small inner tubes inflated to a low pressure to isolate it from room vibrations. The pumping lines are anchored in a smaller sandbox secured by concrete blocks and lead bricks. Flexible bellows tubing is on either side of the smaller sandbox to decouple the room and pump vibration from the cryostat [Ric88] This was tested by temporarily cutting off the pumps for short periods of time while measuring the noise of the systems. For room isolation the opposite effect was tried: noise levels were monitored while noise and vibration was made near the cryostat.

3.4 Specifics of Bolometer Dilution Refrigerator

The cryostat has a 33 cm (13 inch) long, 12.7 cm (five inch) diameter vacuum can that is positioned in a double dewar with a 15.2 cm (six inch) bore. The cold plate fill tube is positioned 2 cm above the bottom of the dewar to enable operation with minimal amounts of LHe. It is important to keep the cold plate fill tube off the very bottom of the dewar in order to prevent it from being clogged with ice and other sediment in the LHe.

The base temperature of the refrigerator is 100 mK. The mixing chamber can normally be regulated at 130 mK with the preamplifier 10 cm away operating at 100 K. The mixing chamber temperature is monitored by using a commercially-calibrated, four lead germanium thermometer from Lakeshore[16]. Temperatures of other components of the refrigerator are monitored with 1 $K\Omega$ Speer resis-

[16]Model GR-200A-50 with a calibration documented from 6 to 0.1 Kelvin; serial number 25659; and calibration report number 198916.

tors [Rot78] All of these resistors are connected to a conductance bridge[17]. The JFET preamplifier board temperature (inside the preamplifier box) was measured with a Pt resistor[18].

The still is maintained at 0.43 K by a resistive heater which provides 500 μW of power. An additional 250 μW of heating coming from the preamplifier. The JFET temperature is maintained at 100K by a resistive heater on the pre-amp board which provides 5.6 mW of power with an additional 3 mW being supplied by the self heating of the preamplifier. The still and pre-amp heater are both powered via battery supplies in order to minimize 60 Hz noise in the system.

The refrigerator can be cooled from 77 K to the operating base temperature in approximately eight hours by using ^{4}He as an exchange gas. The base temperature is found to be independent of the use of an exchange gas. The refrigerator may be safely warmed up to room temperatures in a few hours, permitting the refrigerator to be cycled from room temperature to base temperature and back to room temperature within a 24 hour period.

One of the major reasons for the relatively quick cool down time is the small amount of mash that is used. The refrigerator has a total charge of 7.8 liters of gas, of which 5.4 liters are condensed in the refrigerator. This leaves the balance in the back of ^{3}He Pump and condenser side of the gas handling system. Under normal operating conditions, the refrigerator had a circulation rate of 70 μmoles/sec which provides for a base temperature of 100 mK and an additional cooling power of 4 μW at 130 mK. This temperature is regulated by a Linear Research style temperature controller [Ban81].

In order to improve the resolution of the current devices, the stable base operating temperature for the dilution refrigerator should be decreased to permit operation at below 0.1 K with the JFET-preamplifier operating. This will

[17]Potentiometric Conductance Bridge, Model PCB; SHE Corporation

[18]Model number Omega F3141 which are valid from well above room temperature to 73 K

require better thermal isolation of the preamplifier and additional heat sinking of the leads attached to the mixing chamber. The flow impedance will need to be reconstructed to allow a recirculation rate of 100 μmol/s. It would also be necessary to introduce a discrete heat exchanger to further pre-cool the mash entering the mixing chamber. This would have an additional benefit as it would introduce an additional stage for heat sinking all incoming leads to the mixing chamber. Not as a design concern: but as an operational concern, it would be desirable to replace the cold trap in order to increase the functional time between baking out. The current cold trap is able to operate for a maximum of a few days before being warmed up and cleaned out.

Chapter 4

Calorimeter Assembly

A microcalorimeter consists of three basic parts: the thermistor (discussed in sections 2.1 and 2.3), the absorber, and a weak thermal link. This chapter will discuss the later two parts and also how the system is put together.

4.1 Absorber

In order to minimize the physical amount of material that is needed to stop a particle (and therefore its heat capacity), a high–Z material (where Z is the atomic number) is needed. This material should also have a small specific heat to produce a good energy resolution (as discussed in section 1.2). Radiation of different types will generally require different absorbers so that the overall heat capacity is kept as small as possible. For low energy photons, the dominant absorption method is the photoelectric effect which has an absorption probability that is roughly proportional to Z^4. For higher energy photons, the dominant absorption methods are Compton scattering and pair production. The total cross sections for these mechanisms increase proportionally to Z. For heavy particles the range has also been shown to be dependent on Z [Kra88].

An absorber is needed to rapidly thermalize all the incident radiation that has impinged upon its surface. To accomplish this one must avoid using materials that can trap charge, thereby creating long–lived states. A variety of metals and

semi-metals have been analyzed for use as microcalorimeter absorbers. Of those considered, Au, Ag, Bi, Ge, HgTe, InSb, Nb, sapphire, and Sn have been shown to make reasonably good absorbers [Mos84, McC90, Kel93].

One of the limitations in the choice of an absorber is the heat capacity, which is typically linear in T for normal metals as was discussed in section 1.4. For this reason, Sn was used which, in its superconducting state (below 3.72 K [Pob96]), has a T^3 heat capacity dependence which is discussed in section 1.4. It has a Z of 51 and is very malleable allowing a small amount to provide for 4π coverage of a source. Tin was shown by a variety of groups to be a reliable absorber [Dep94, Sta93, Sta97] with only a small percentage of the deposited energy being trapped in long-lived states. It also has a relatively high Debye temperature (200 K) [Pob96] allowing it to have a relatively low specific heat at the operating temperature.

A 50 μm thick Sn foil (99.99% pure)[19] was used for this project. It was annealed in a flowing He atmosphere at 215 $^\circ C$ for 8 hours. Thinned GE 7031 varnish was used to attach the Sn foil to the back of the silicon chip. A small drop of thinned varnish was applied to the Sn and foil was then attached to the back of the Si chip. The device was allowed to dry for 6 hours before being cooled down.

The heat capacities of the elements composing the microcalorimeter are presented in Table 4.1. The Si wafer values are presented only as a comparison for the $Au_xGe_{(1-x)}$ values reported. Aluminum is included for completeness as it will be used for the thermal link discussed in section 4.2. The total does not include the Si heat capacity and includes only $\frac{1}{3}$ of the heat capacity of the Al wires.

[19]Goodfellow SN000240/10: tempered as rolled when purchased.

Material	Specific Heat ($\frac{J}{g\ K}$)		Heat Capacity (J/K) at 150 mK
$Au_xGe_{(1-x)}$ chip	5.31 10^{-11} +	1.36 10^{-8} T	5.8 10^{-12}
Si chip		6.6 10^{-7} T^3	1.2 10^{-12}
GE 7031	6.5 10^{-6} T +	1.9 10^{-5} T^3	4.9 10^{-13}
Au pads	3.5 10^{-7} T +	2.1 10^{-6} T^3	9.8 10^{-14}
Tin		2.1 10^{-6} T^3	1.3 10^{-11}
Al		9.2 10^{-7} T^3	3.1 10^{-14}
Total			1.9 10^{-11}

Table 4.1: Heat capacities of materials used in microcalorimeters. The $Au_xGe_{(1-x)}$ values are reported by Wang [Wan95]. The Si values assume the chip heat capacity was dominated by the wafer (ignoring the thin film) [Pob96]. The GE 7031 data is from Stevens [Ste73]. The heat capacity for the Au contact pads is calculated and confirmed by empirical data for pure Au [Lou74]. The Sn formula is taken from a fit to existing data [ONe65]. The Al wire numbers are calculated using the Debye model [Ash76].

4.2 Weak Thermal Link

The weak thermal link connects the rest of the microcalorimeter (namely, the thermistor, absorber, and strong thermal link between them) to the mixing chamber. This thermal link will determine the base operating temperature of the device relative to the mixing chamber and its thermal relaxation time. The choice of thermal-link parameters will depend on the operating temperature, the heat capacity of the device and the electronic response time.

Ideally, the weak thermal link would not significantly increase the heat capacity of the device. Calculations show that as the heat capacity of the thermal link increases relative to the rest of the microcalorimeter the thermal decay is no longer a single exponential. Instead, there is a thermal decay with two time constants: the device (thermistor and absorber) initially thermalizes with the thermal link and then the thermal link and device together decay back to the

mixing chamber temperature. Since the second decay time characterizes the thermal relaxation of the device, it is desirable to minimize the initial thermalization time.

Approximately one third of the heat capacity of the thermal link will contribute to the total device heat capacity [Gal86]. For this reason, it is important to use materials with minimal ratios of specific heat to thermal conductivity. This allows one to reduce the amount of material used for the link until the desired thermal conductivity is achieved. In practice, physical dimensions and material selection will be limited by physical constraints and commercial availability.

The weak link has two other duties besides providing the thermal conductivity between the mixing chamber and the rest of the microcalorimeter: it also provides the physical support for the device and electrical connections to the thermistor. Additional physical support can also be provided, but this requires that either the additional support have a significantly weaker thermal link to the device or that it have a negligible heat capacity. The requirement of making proper electrical connection requires the use of at least two wires.

Throughout this work, three materials were used for weak thermal links: brass, Au, and $Al_{99\%}Si_{1\%}$ (which will be referred to as Al wire). Brass has been used only in initial tests using Speer resistors [Lov87] and small resistive heaters [Moy83]. The Au wire was used to make the initial thermistor resistance versus temperature curves (see section 2.4 and 2.2) as it supplied strong thermal coupling between the thermistor and the cold finger. Al was used in a majority of our experiments because it is a superconductor below 0.922 K in the absence of a magnetic field. The electrons in superconductors form Cooper pairs and these pairs are unable to carry thermal energy. Therefore, the thermal energy is carried primarily by the lattice phonons. This usually produces a thermal conductivity that is proportional to T^3 [Sha67, Glo90]. For non-superconducting metals like Au, the dominant thermal carriers are the electrons. Their thermal conduction is limited by lattice vibrations and the concentration of impurities

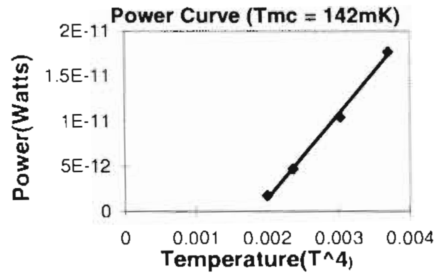

(a) Power curve at 142 mK

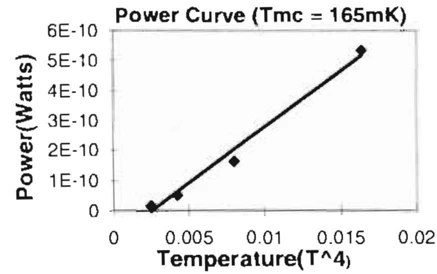

(b) Power curve at 165 mK

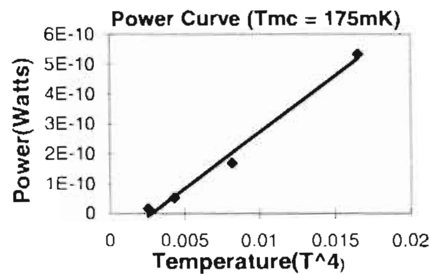

(c) Power curve at 175 mK

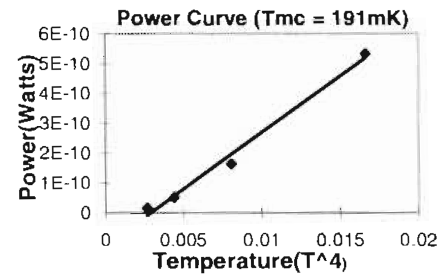

(d) Power curve at 191 mK

Figure 4.1: Power versus T^4 for Al wires at operating temperatures from 142-191 mK.

within the lattice. The presence of impurities will reduce the electron conduction to a level comparable to that of the phonons.

The thermal conductivity of the Al wires was measured using a "steady state" method [Sha67] where one end of the Al wire was thermally attached to the mixing chamber while the other end was heated by a bias voltage. The temperature difference between the two ends was then measured by two different resistors. A calibrated germanium resistor measured the mixing-chamber temperature, and the other resistor was the microcalorimeter thermistor which was calibrated against the germanium thermistor by applying a negligible amount of heating. The power curves are shown in Figure 4.1 and 4.2. The devices were allowed to

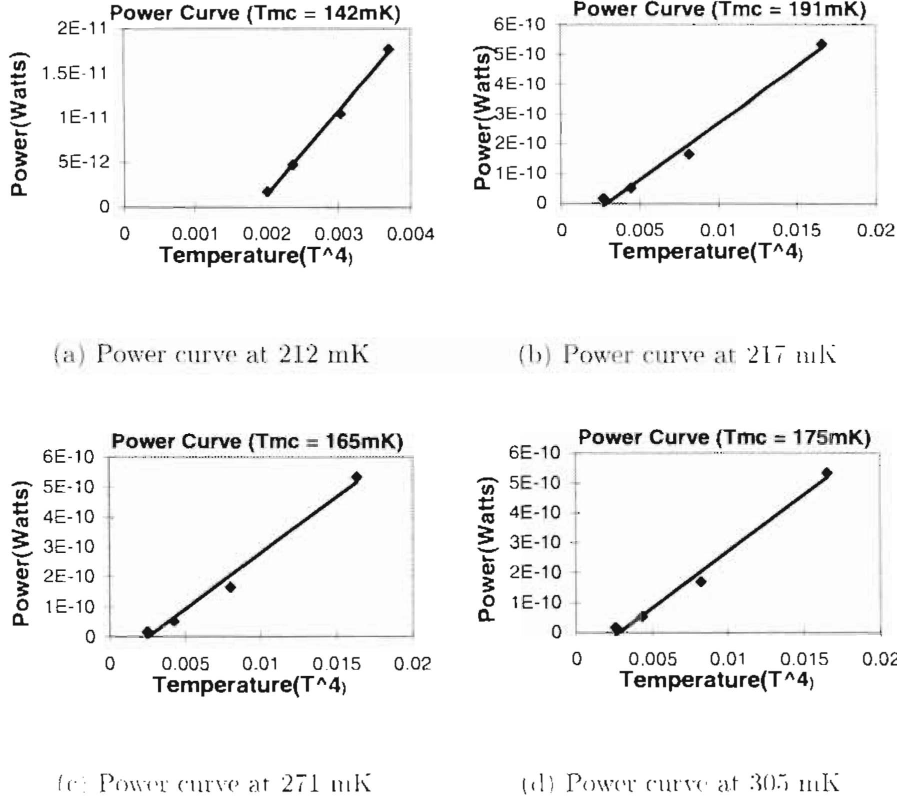

(a) Power curve at 212 mK

(b) Power curve at 217 mK

(c) Power curve at 271 mK

(d) Power curve at 305 mK

Figure 4.2: Power versus T^4 for Al wires at operating temperatures from 212 305 mK.

reach equilibrium, so therefore, the power in must equal the power out.

$$\dot{Q}_{IN} = \dot{Q}_{OUT} \tag{4.1}$$

The power in is simply the resistive heating ($\dot{Q}_{IN} = I^2R$). The power is carried out of the device by the Al wires and the energy loss is given by:

$$\dot{Q}_{OUT} = \frac{A}{l}\lambda \int_{T}^{T_{MC}} t^3 dt \tag{4.2}$$

where A and l are the dimensions of the wires, λ is the thermal conductivity constant. T^3 represents the temperature dependence of the heat capacity for a superconductor which is integrated from the device temperature to the mixing chamber temperature. Combining equations 4.2 and 4.1 one arrives at 4.3

$$\dot{Q}_{IN} = \frac{A}{4l}\lambda \left(T^4 - T_{MC}^4\right) \tag{4.3}$$

Operation temperature	Value of λ $\left(\frac{W}{K^4\ cm}\right)$
112 mK	.00367
165 mK	.0116
175 mK	.0116
191 mK	.0147
212 mK	.0151
217 mK	.0152
271 mK	.0158
305 mK	.0133

Table 4.2: The measured thermal conductivity constants for Al at various temperatures.

The slope of the linear fit to $\dot{Q}_{TN}$ versus T^4 gives the conductivity constant (λ). Fits to the data using this relationship are shown in Figure 4.1 and 4.2 and the resulting values for λ shown in table 4.2. These values yield a thermal conductivity of

$$\kappa(T) = 0.013 \pm .004T^3 \frac{W}{K\ cm} \tag{4.4}$$

which are lower than reported values for Al 5056[20] taken below 1 K which show a value of .023 W/(K^4 cm) for λ [Coc83].

Calculating the thermal conductivity of the weak thermal link from equation 4.4 at 0.15 K gives a conductivity (G) of 6.0 10^{-10} W/K. Therefore, using the heat capacity as displayed in Table 4.1 the thermal relaxation time is calculated as

$$\tau \approx \frac{C_P}{G} = 0.032 \text{ seconds.} \tag{4.5}$$

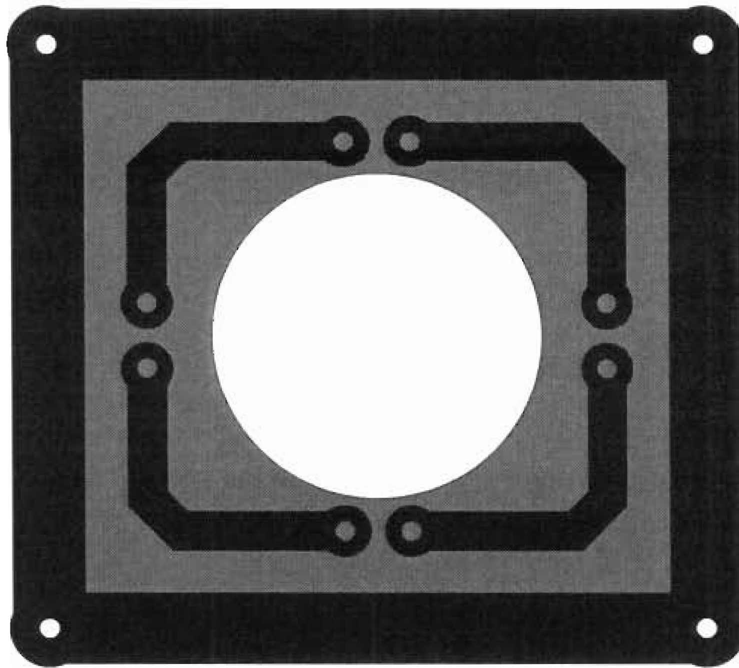

Figure 4.3: Chip carrier used for wirebonding the microcalorimeter.

4.3 Chip Carrier

A chip carrier is needed to hold the microcalorimeter during assembly and operation. We initially used a 28 pin, commercially-available leadless chip carrier[21] which had Au contact pads and Au coated leads. The carrier was held in place by a 28 pin socket which was shown to be able to maintain continuity at all operating temperatures. The carrier was used primarily for the initial RT-curve measurements as it provided an easy means of changing the test sample. The final chip carrier was made of standard circuit board material with a patterned copper layout. This holder is shown in Figure 4.3. The inner four copper pads allowed for electrical connection to the chip. The outer copper band was used to provide good thermal contact between the chip holder and the mixing chamber. The center of the chip holder was drilled out to a 1.3 cm (one half inch) diameter

[20] 5.6% Mg, 0.1% Mn, 0.1% Cr, balance Al [Coc83]

[21] Amp Part Number 821555-4

which allowed the thermistor absorber assembly to be suspended by the Al wires.

The chip holder was sanded, polished and ultrasonically cleaned to create a proper surface for wirebonding. The chip holder was then loosely taped onto a homemade brass vacuum chuck shown in Figure 4.4. In the center of the vacuum chuck, a 0.9 mm (0.035 inch) diameter hole was drilled to hold the chip during wire bonding. The entire surface of the holder was then cleaned and polished. The side of the chuck had a tube attached to allow a vacuum to be applied indirectly to the surface through the small capillary which secured the chip to the holder.

A manual wedge wirebonder[22] was used with Al wire to make the wirebond connection. The wire was first connected to the copper pads of the holder and then connected to the Au pads of the chip. This placed the excess wire created by the first bond on the copper pad so that it did not contribute to the heat capacity. The final setup is shown in Figure 4.5 with the wire bond connections from the chip connected to ends of two of the copper pads. After the wire bond connections were made, electrical leads were soldered to the other ends of the copper pads. While soldering, a heat sink was temporarily held in the middle of the copper pad to protect the Al wire-Cu pad bonds. The chip holder was then screwed down to a copper frame which was attached to the cold finger, providing good thermal contact with the mixing chamber.

[22]Kulick and Soffa: model 4123 wire bonder

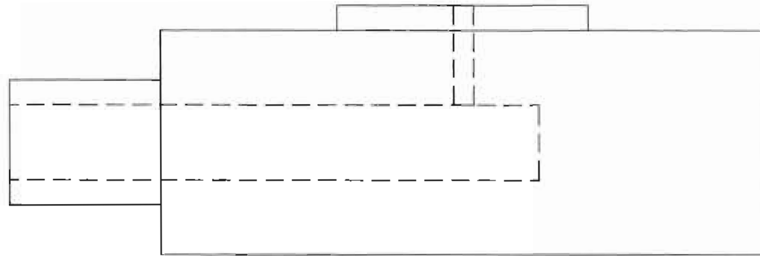

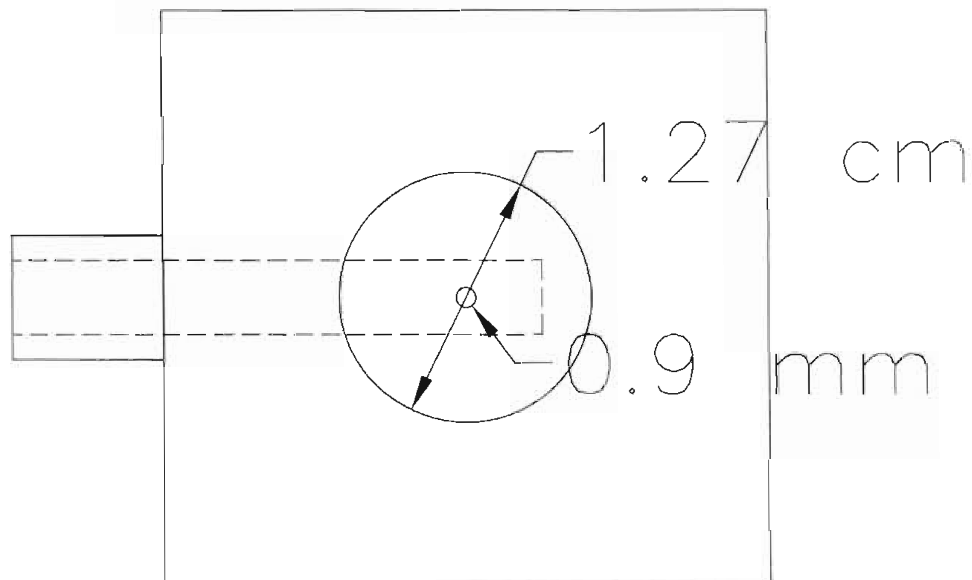

Figure 4.4: Vacuum chuck used for wirebonding.

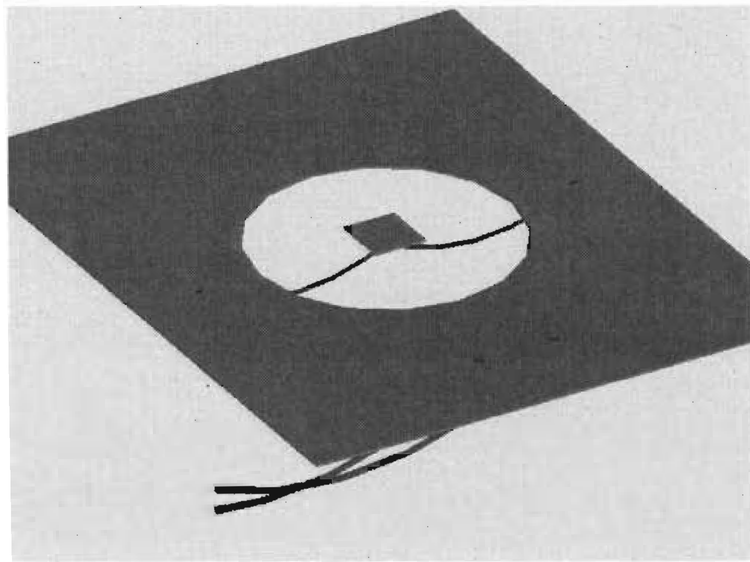

(a) Bottom view of microcalorimeter setup showing the back of the chip carrier and the absorber attached to the microcalorimeter.

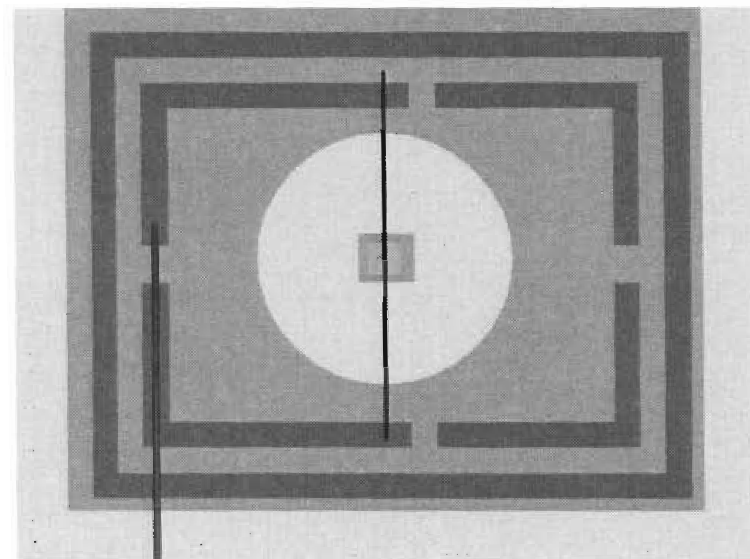

(b) Top view of microcalorimeter setup showing the copper thermal conduction strip around the edge of the chip carrier with the copper contact pads inside that square. The Al wires connect the thermistor to two of the four copper pads. The electrical wires connecting the device to the rest of the electronics are soldered to the ends of both of these copper pads.

Figure 4.5: Chip carrier and microcalorimeter setup.

Chapter 5

Data Acquisition and Analysis

5.1 Electronics

The electronics are composed of two parts: the biasing circuit and the amplifier circuit. The biasing portion provides a bias current through the microcalorimeter thermistor. The amplifier system is designed to measure the voltage across this device.

To measure the change in resistance, the thermistor is placed in a symmetrically biased voltage divider as shown in Figure 5.1. The bias resistors used were small 1% tolerance metal film resistors[23]. The bias resistors were directly attached to both the incoming signal lines and to the electrical leads of the microcalorimeter, and were located on the mixing chamber in order to reduce the Johnson, or thermal, noise of the system. The root mean square thermal voltage noise is

$$v_n = \sqrt{4k_B T R B_W} \tag{5.1}$$

where k_B is Boltzmann's constant, T is the absolute temperature, R is the resistance and B_W is the band width of the measuring instrument [Die79].

Shot noise, which arises from the statistical distribution of the finite charge carriers, has the behavior

$$v_n = \sqrt{2I_o e R^2 B_W} \tag{5.2}$$

[23] Dale CMF-55 Resistors

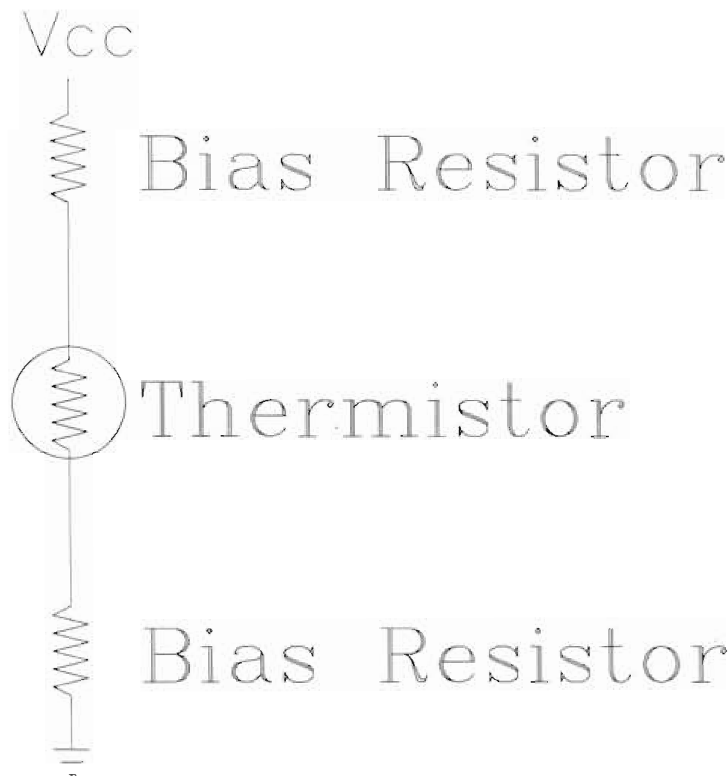

Figure 5.1: Bias resistor arrangement for the thermistor.

where the voltage is again rms voltage. I_o is the average DC current through the resistors and e is the charge of the electron. [Sim87].

Another noise source is flicker noise, or $\frac{1}{f}$ noise which can be troublesome at low frequencies. The magnitude of this component was reported for the amplifiers used, and was experimentally measured for the given experimental setup.

For the setup in consideration, one is concerned with measuring the voltage across the thermistor. In order to calculate the noise produced by the bias system, the setup can be reduced to a Thévenin's equivalent circuit as shown in Figure 5.2 [Die79]. The effective resistance is approximately 1 MΩ, the DC current is 3 nA, the temperature is 150 mK and the band width is 100 kHz.[24] The lower limit on the total noise from these two sources is shown in table 5.1.

[24]The bandwidth is typically calculated to be the inverse of the sampling time. For the data acquisition card being used, the time for one analog to digital conversion is at most one half the sampling cycle as determined by the sampling frequency. So, using a sampling frequency of 50 kHz, $\Delta T = 10\ \mu sec$ and therefore

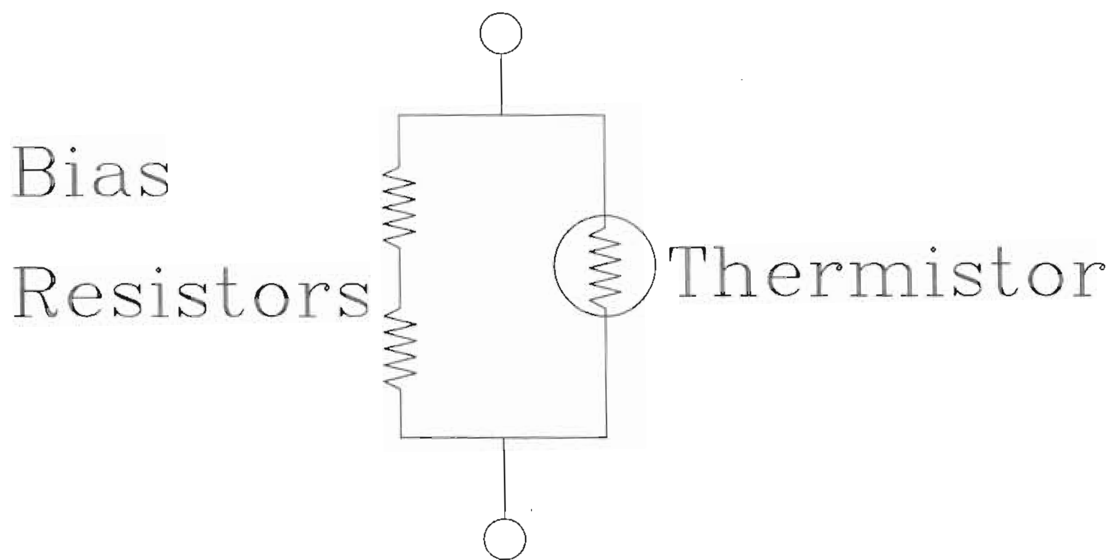

Figure 5.2: Thévenin's equivalent for the bias circuit.

Noise Source	rms noise	rms noise density
Johnson noise	1 μV	$2.8\ 10^{-9}\ \frac{V}{\sqrt{Hz}}$
Shot noise	10 μV	$3.1\ 10^{-8}\ \frac{V}{\sqrt{Hz}}$
Total noise	10 μV	$3.1\ 10^{-8}\ \frac{V}{\sqrt{Hz}}$

Table 5.1: Noise sources for bias circuitry.

The total is just the square root of the sums of the squares because both sources have a Gaussian distribution. The values shown are the values measured at the input of the first amplifier stage, the JFET preamplifier, so these values will be amplified by all the pre-amplifier and amplifier stages.

5.1.1 JFET Preamplifier

The preamplifier was composed of a pair of matched junction field effect transistors (JFET), configured as a source follower. The primary purpose of this preamplifier was to reduce the impedance seen by the signal to prevent attenuation as it exited the cryostat. This also prevented the thermistor bias circuit

B_W =100 kHz.

from being capacitively loaded by the signal lines coming out of the cryostat. The two input signals coming from either side of the thermistor were connected to the gates of the transistors. The output signal was connected to the source line. The source resistance and hence the current through the JFET was designed such that the gate-to-source junction would be reverse-biased. In this mode, the preamplifier has its maximum input impedance [Sim87]. The JFETs used for this project were n-type,[25] biased with the source at 1.5 volts relative to ground. This was done by using a dual source supply of $\pm$ 9 volts with the proper choice for the source resistance (80 kΩ). As long as the voltage through the bias circuit was kept below a few volts, the junction was reverse biased having an input impedance of 150 MΩ [Cal].

Since the JFET is not able to operate near LHe temperatures, additional heat was applied using resistive heating. The source voltage of the JFET was very temperature dependent until it reached its operating conditions at about 100 K (which was measured using a platinum thermistor on the pre-amp board). This temperature dependence allowed an additional method of monitoring the temperature to establish the ideal operating conditions. The input power supplies were both filtered by capacitors on the board. Figure 5.3 shows electrical and thermal considerations of the biasing and JFET circuitry. The signals to the gates of the JFETs were connected to the microcalorimeter through a series of thermal anchors as described in section 3.3.

The signals from the JFETs were carried out of the cryostat by microcoax cable.[26] The leads were directly soldered to the preamplifier board and connected at the top of the cryostat to electrically isolated BNC connectors to allow for connection to the room temperature differential preamplifier.

[25] Model 2N6483 from Calogic Corporation

[26] LakeShore type "S1" stainless steel low temperature micro coaxial cable.

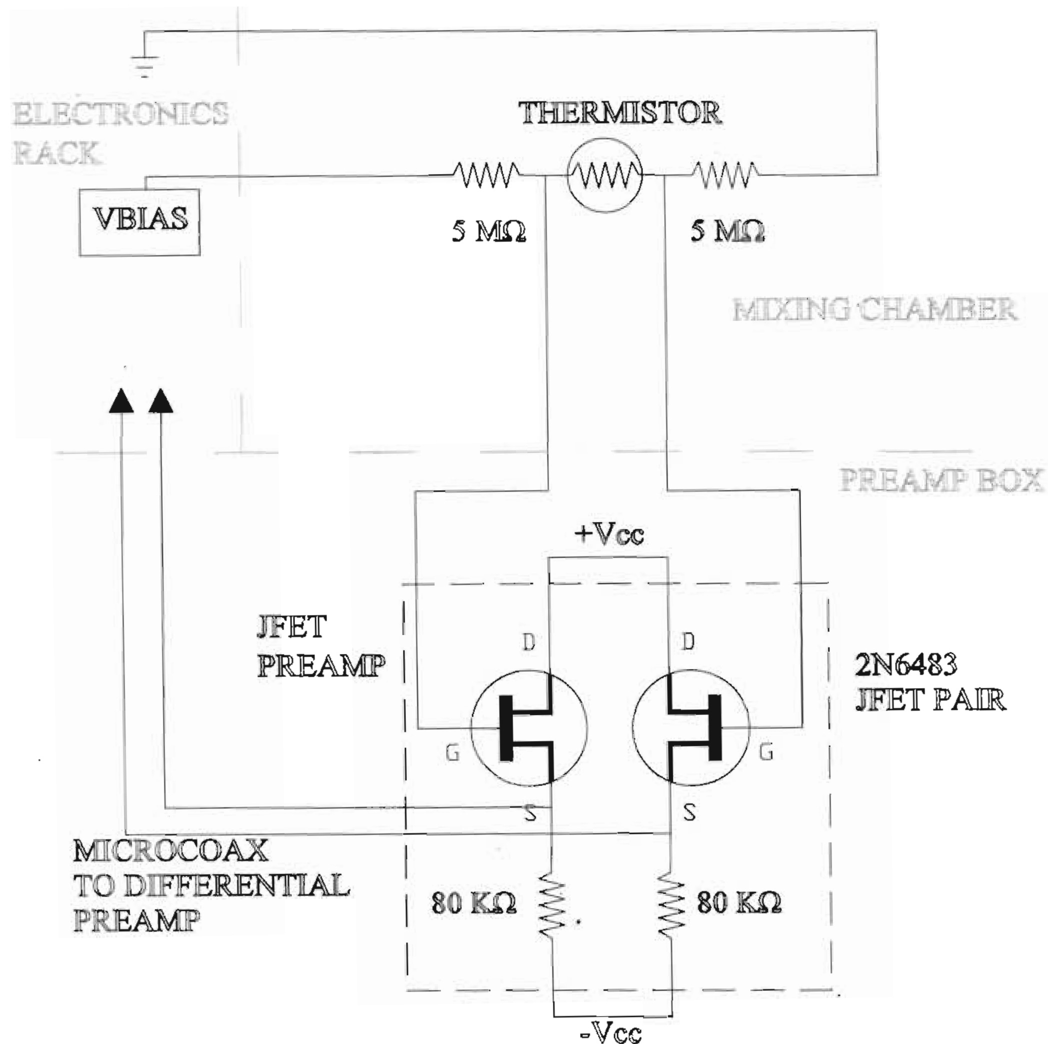

Figure 5.3: Biasing and JFET preamplifier.

5.1.2 Differential Preamplifier

The differential preamplifier was dc coupled to the JFET preamplifier output. BNC connections were made from an electrical isolation plate on the top of the cryostat to the differential preamplifier box. The preamplifier box was directly grounded to the cryostat. The power for this preamplifier was supplied by two 9 V batteries located inside this box. These batteries were able to effectively operate the preamplifier for 100 hours before requiring replacement.

The schematic of the differential preamplifier is shown in Figure 5.4. This

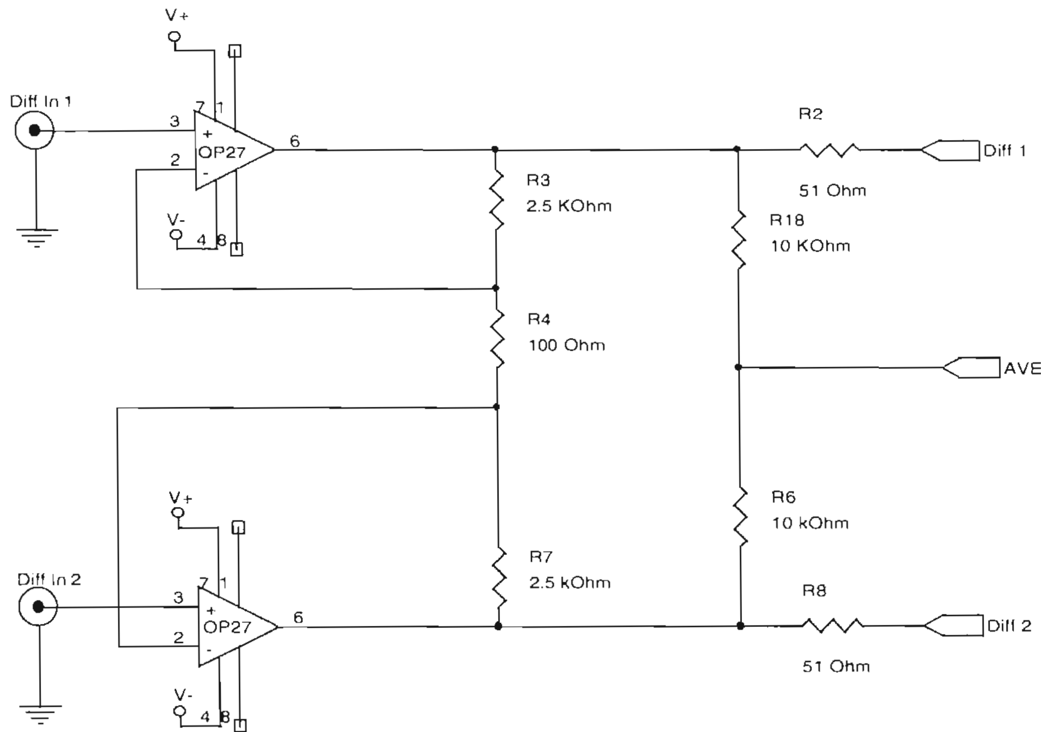

Figure 5.4: Differential Preamplifier.

design provides for a differential gain of 51. The OP-27 operational amplifiers were chosen for their excellent low input voltage noise characteristics [PMI]. The 51 Ω resistors on the two output lines were used to limit the effective capacitance of the output as the OP-27 was unable to drive a significant load. The "AVE" output was used to monitor the average voltage of the two input signals. This allowed for another method of measuring of the JFET's operating temperature. Further documentation and discussion of this amplifier design is provided by Deptuck [Dep94].

5.1.3 Differential Amplifier

The second amplification stage is shown in Figure 5.5. This stage utilized two capacitively coupled operational amplifiers with a gain of 201. This stage was powered by an external twelve volt dc power supply. Resistors R10, R11,

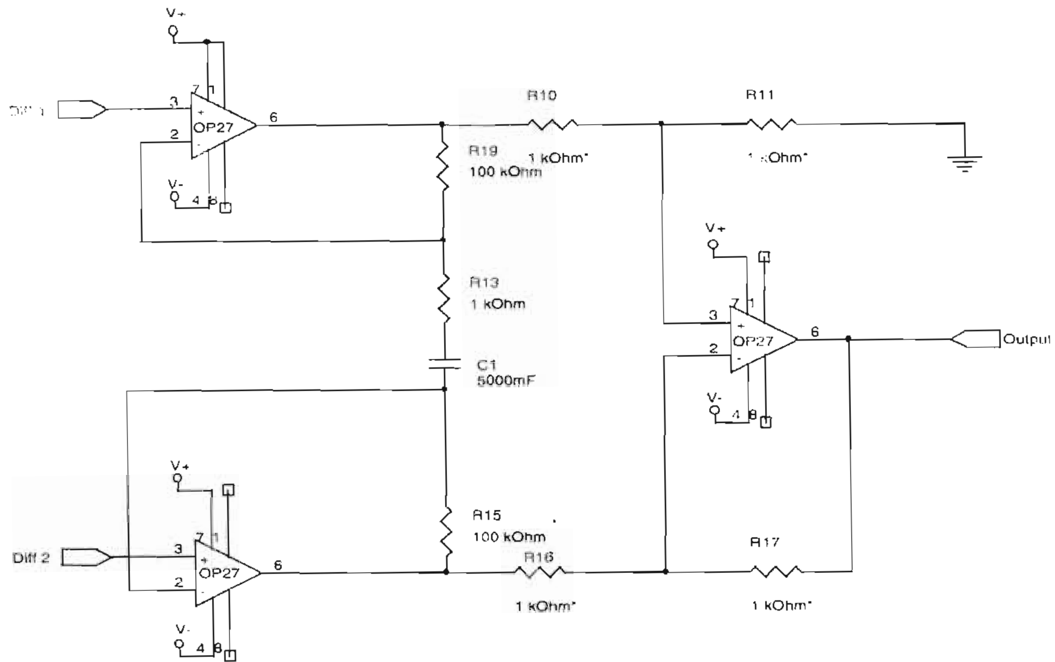

Figure 5.5: Differential Amplifier.

R16, and R17 were all matched to better than 0.1% to reduce the common mode rejection ratio for the system, which was limited by the input impedance of the OP-27 to be 120 dB. The capacitor C1 and resistor R13 determined the low frequency cut-off limit of this device.

Another version of the second stage was constructed and is shown schematically in Figure 5.6. This amplifier provided a variable gain of 201, 21 or 2, and allowed for the amplifier to be either dc or ac coupled. DC coupling was used to remove the amplifier time constant from the system to look at pulses with long decay times. The smaller gain options were used to perform resistance versus temperature curves using an low frequency AC bias voltage. A version of the differential amplifier was also constructed with a variable resistor between the positive and negative power supplies with the tap connected to R11. This allowed the dc offset to be removed since they posed a problem when operating at large gains. Locating the variable resistor at the final stage of the system ensured that there was not a substantial increase in noise.

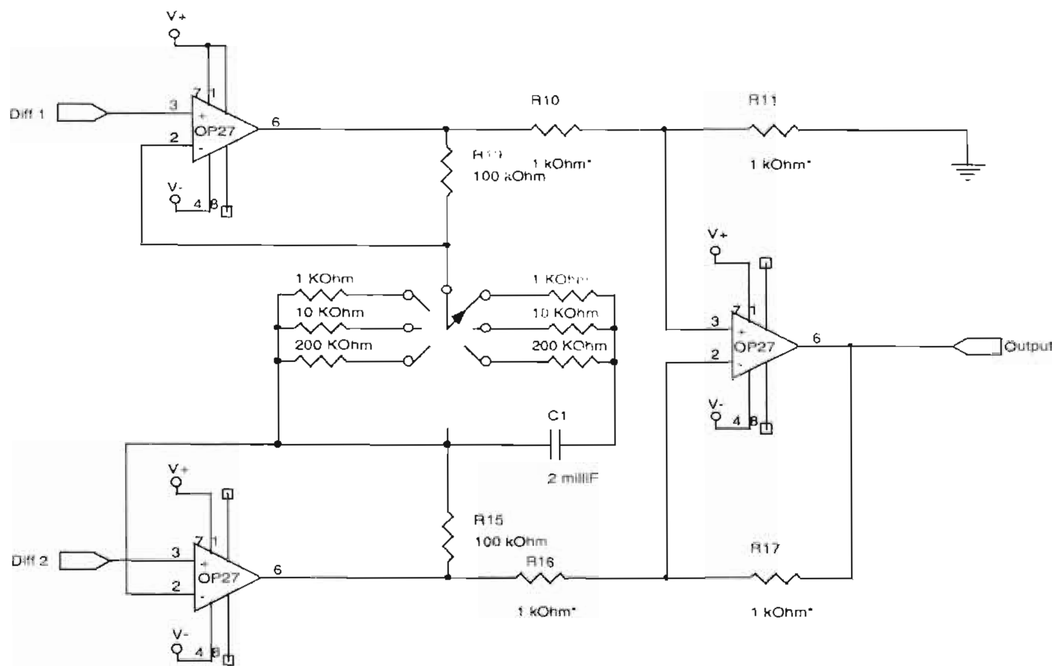

Figure 5.6: Variable gain differential amplifier.

The OP-27 was used for this experiment, but the AD797 was an equally suitable replacement for all except for the initial stage [PMI, Ana94a]. The AD797 was measured to have slightly more noise at low frequencies than the OP-27.[27]

The total gain versus–frequency for the amplifier system is shown in Figure 5.7. The low frequency roll off is due to the capacitive coupling of the final amplifier stage. The high frequency roll off is due to the limit of the gain versus frequency of the operational amplifiers.

The noise of the system is shown in Figure 5.8. The horizontal line at $3.4\ 10^{-8}\ V/\sqrt{Hz}$ shows the theoretical contribution from the thermal and shot noise (from Table 5.1). The other two curves show the actual measurements

[27] The pin–out of the two chips allow for interchangeability as long as one does not connect a null offset circuit. The default offset of the chip was satisfactory for the needs of these circuits and additional adjusting would introduce additional noise.

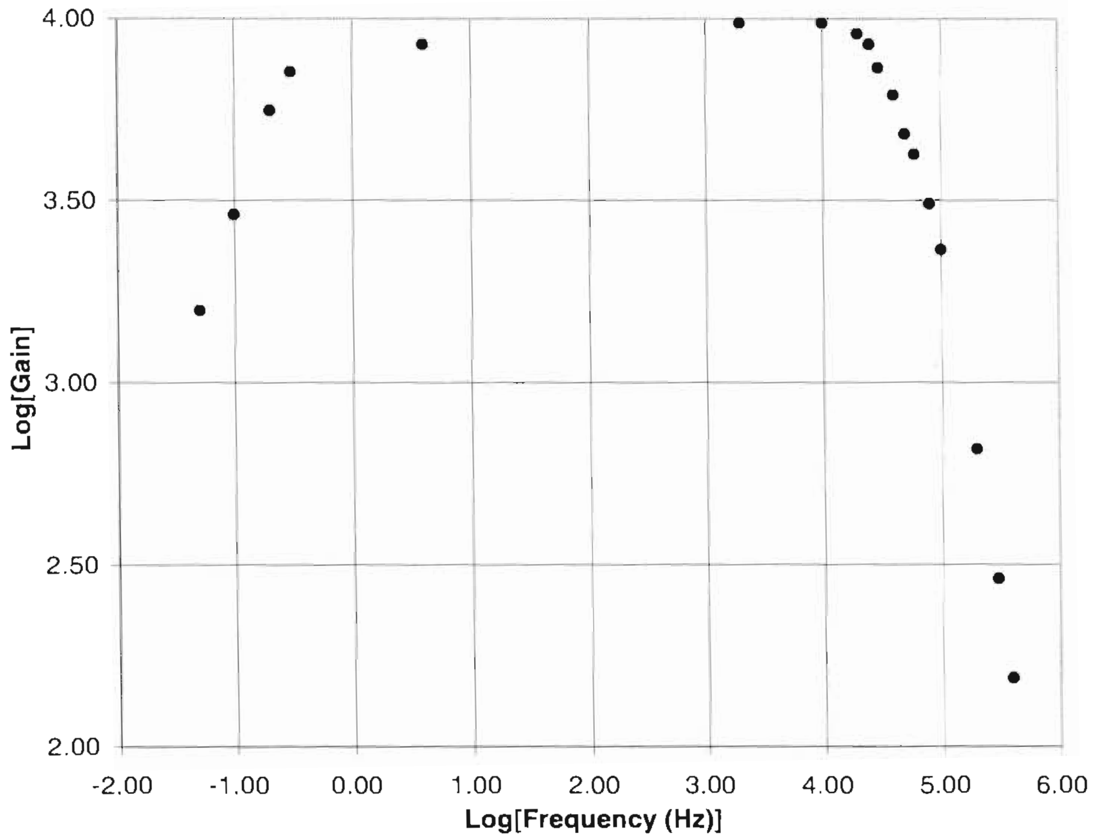

Figure 5.7: Gain versus frequency for the amplifier system.

of the noise of the system. The lower curve is the noise contribution from the preamplifier and differential amplifier.[28] The top curve is the measured noise of the entire system with the microcalorimeter biased and at its proper operating temperature. This data were extracted from the baseline sweeps made during data acquisition. The fact that the system noise curve is below the theoretical limit due to the Johnson and Shot noise contributions at high frequencies indicates that there is a band-width limit from the JFET preamplifier. The deviation above the theoretical limit at low frequencies is due to 1/f noise.

[28]The measured signals were normalized by replacing the OP-27 preamplifier with a comparable amplifier of significantly more input noise voltage. The input noise of the standard operational amplifier dominated the system. This value was then used to normalize the reported values for the described amplifiers [Ana94b, Ana94c].

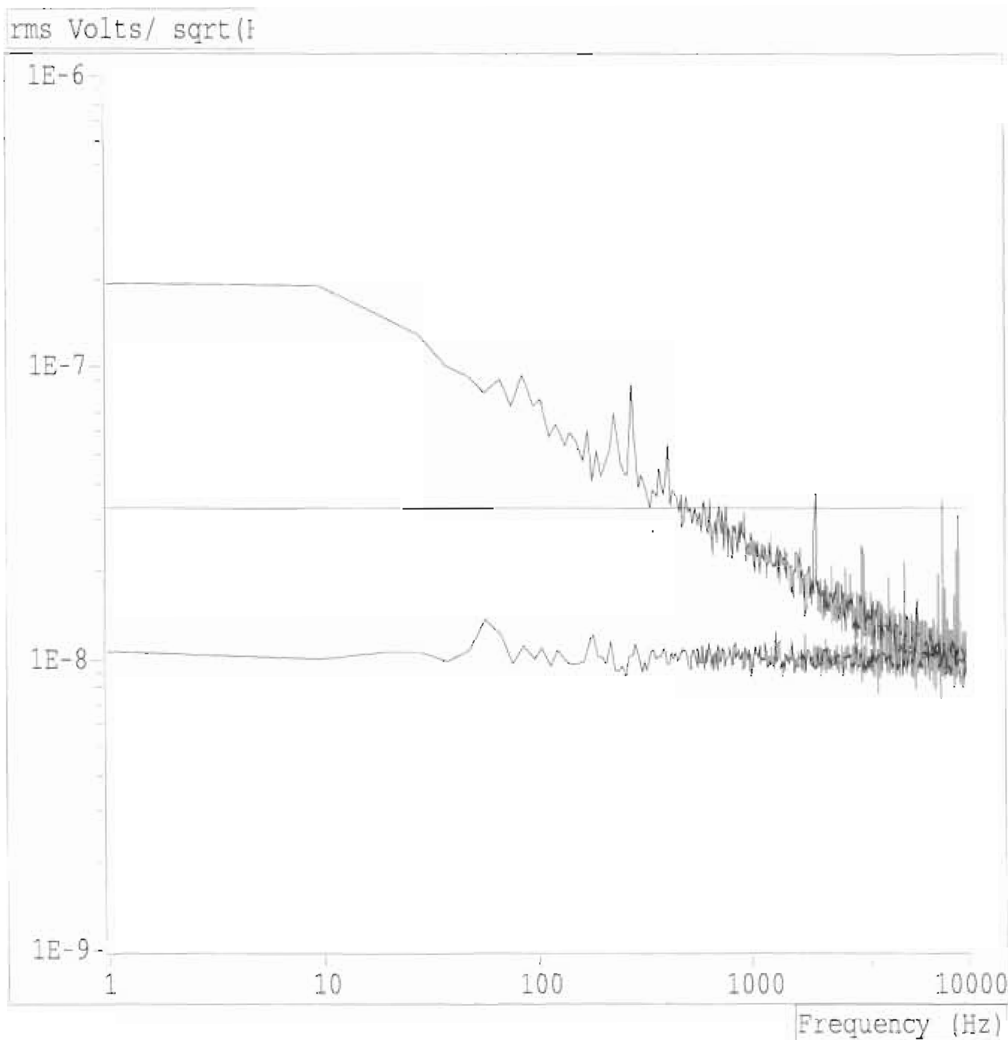

Figure 5.8: Voltage noise spectral density

5.2 Data Acquisition

The voltage signals that are produced from the amplifiers are indicative of the amount of energy that has been deposited into the microcalorimeter. These voltage signals have to be digitized, stored and processed in order to produce an energy spectrum. For this project, two separate computers were used. One was responsible for digitizing the signal and temporary storage and the other machine was responsible for analysis and permanent data storage.

Data acquisition is performed by an IBM PC clone with an internal National

Instruments card operating in a Windows environment.[29] The card has a 12-bit analog–to–digital converter capable of performing 200 ksamples/sec/channel [Nat94]. This device was operated in a differential mode to provide isolation between the computer and electronic grounds. The software controlling the card was written in G, the graphical programming language used by LabVIEW [Nat96a]. LabVIEW is a multiplatform programming language developed as a platform independent data acquisition and analysis package [Nat96b]. The acquisition machine was connected with a 10-base-2 ethernet line to the data analysis machine. The system is shown in Figure 5.9.

The data acquisition card was set up to mimic the function of a storage oscilloscope. An untriggered voltage sweep is made of the amplified signal. This signal is used to set the background level and the trigger level for pulses. The trigger level is then chosen to be above the noise level and determines the minimum pulse height that can be detected. The master data acquisition program records the voltage sweep of pulses that are above the trigger level. The voltage sweeps are composed of 100 pretrigger samples followed by 924 post-trigger samples for a total of 1024. The sampling frequency, pretrigger scans, and sweep length are all variable within the limits of the data acquisition card. The typical data acquisition rate was set at 50 ksamples/s which allows 20 μsec per sample for a total of a $\approx$ 20 ms per sweep. The binary data from the 12 Bit DAC for these 20 ms voltage sweeps were saved directly to a signal file. The binary data, instead of the actual voltage data were saved in order to reduce the amount of calculation required of the acquisition computer. This also reduced the amount of disk space required for storage of the data files. These files were named using the day and time with a common extension of ".sgn". The master data acquisition program was also set up to record the baseline every eighth sweep to be used for background determination. Five hundred pulses were typically stored in

[29]The card was an AT-MIO-16F-5 operating in an 486DX-33 with Windows 3.11

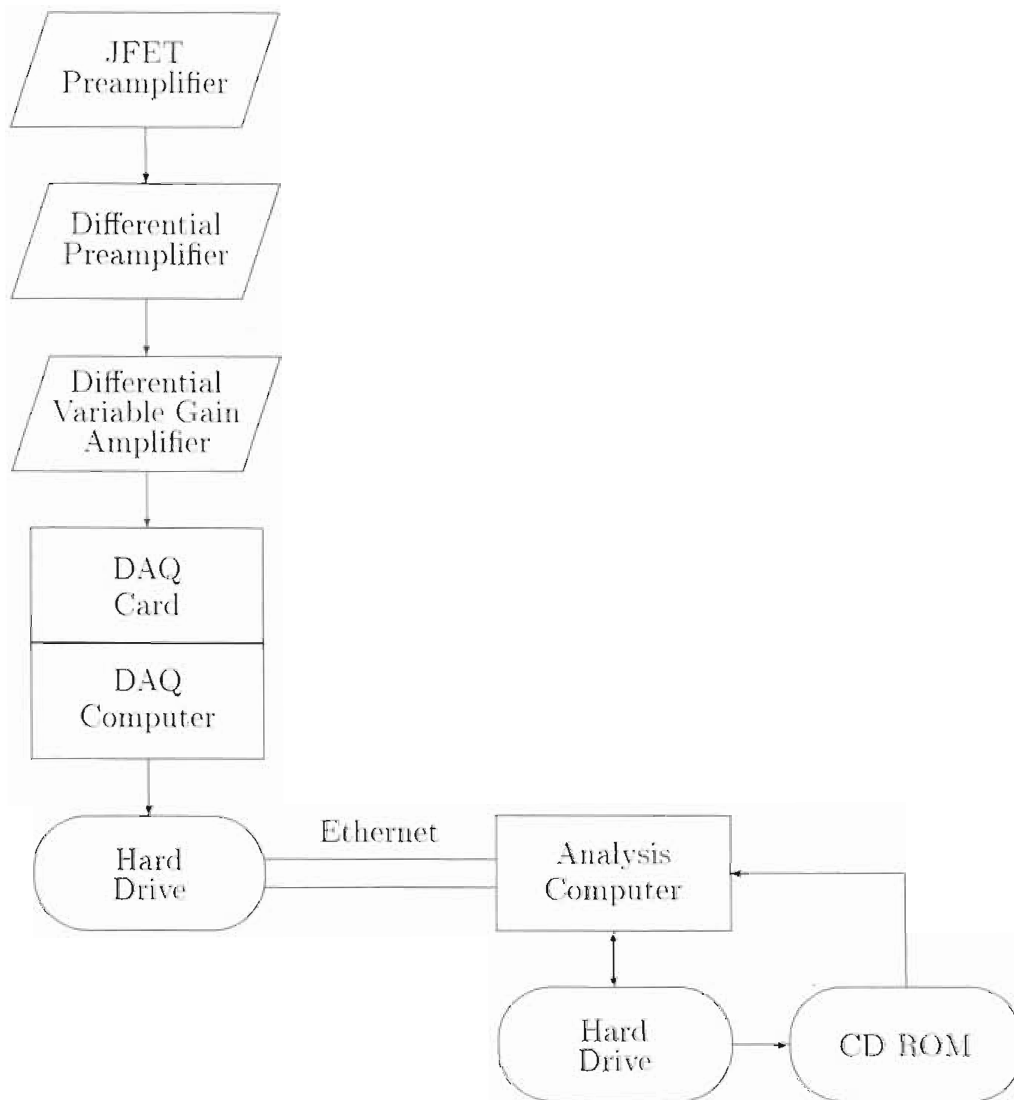

Figure 5.9: Data acquisition and analysis computer system.

a single signal file.[30] The program was then automated to continue to reacquire data until stopped by the user.

A schematic of a signal file is shown in Figure 5.10. The information stored in each of the individual files was required to contain the information to reproduce the voltage data of all of the recorded sweeps. For this reason, the beginning of each file contained four single precision floating point numbers (4 bytes each) to

[30]These files were additionally written as single precision floats. Therefore, these files were originally *single signal single* files.

Delta T (seconds)
Wavelength in scans
Pretrigger length
Scaling Factor

background sweep
triggered sweep
triggered sweep
triggered sweep
triggered sweep
triggered sweep
triggered sweep
triggered sweep
background sweep
triggered sweep
triggered sweep
triggered sweep
triggered sweep

Figure 5.10: Schematic of a signal data file.

describe the data: the sweep length in samples, the data sampling rate, the time offset of the start of the sweep (a product of the number of pretrigger samples and the sampling rate), and the multiplicative factor to convert from the binary data to the voltage data. The rest of the file was the binary data from the sweeps listed consecutively (allowing 2 bytes for the storage of each of the 12 bit numbers). This allowed the 500 voltage sweeps to be stored in 1-MB files.

At the completion of each signal file, the master data acquisition program copied the files to the data acquisition machine for analysis. The data acquisition computer had a 500 megabyte hard drive which was cleaned off daily after the files were analyzed and backed up.

5.3 Data Analysis

The data analysis machine was a 586 generation personal computer operating in a Windows environment. This machine was equipped with an additional 2-GB hard drive dedicated for data storage that was able to be accessed directly by

the data acquisition machine. A compact disc recorder was also added to allow for backing up and storing data (640 Mbyte per disk).[31]

The data analysis software was also written using software written in G, utilizing the LabVIEW programming language. The analysis involves a number of independent steps that ultimately produce an energy spectrum. The programs were designed to analyze an entire run directory of signal files. The final output was a histogram of the voltages from the individual pulses.

The initial portion of the analysis consists of routines to reread the binary data files (see Figure 5.10) created by the data acquisition program. These files were reconstructed into the acquired voltage sweeps. The pretrigger scans were then averaged to provide for a baseline voltage level for each of the individual pulses. The pulses were then reread individually and normalized, by subtracting the baseline from each of the voltage sweeps. The baseline was determined independently for each pulse.

These normalized signal files are analyzed using three different methods: exponential fit, average, and maximum. These routines all processed the data in the same basic way: A time window is set for all of the pulses to delimit the region where the appropriate fit routine will be applied. This window is usually located in the decay portion of the pulse, typically chosen to be from 0.2 to 2 ms following the trigger (as can be seen in Figure 5.11).

The windowed area can then be analyzed using three different methods. The first method is to fit an exponential to the region. If the entire region is not entirely above (or below for negative pulses) the baseline, now renormalized to zero volts, then this method will generate a response of "not a number." The signals can also be filtered using the decay time constant. The pulse amplitude from this method was extracted by using the voltage amplitude at $t = 0$. In order to accurately account for all the pulses, the value of -99 was used for any

[31] Dell Dimension©Pentium©-133 operating under Windows 95. The CR-Recorder was a Philips Easywriter model 2600.

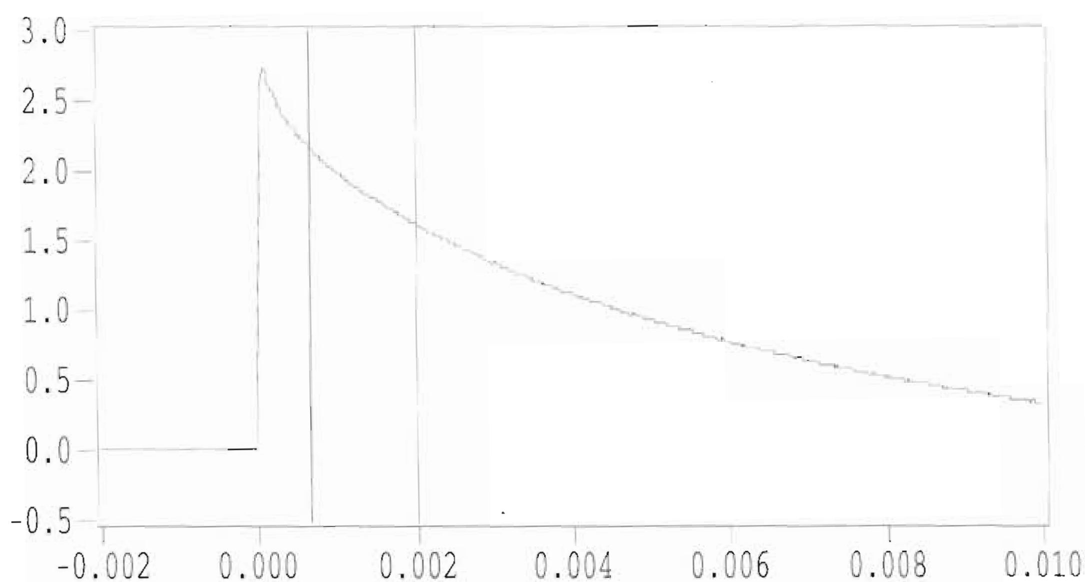

Figure 5.11: Windowing a voltage sweep of a pulse in the signal file. Time is chosen to be equal to zero at the trigger.

"not a number" response.

The second method was to average the sweep region between the cursors. This method was capable of analyzing all of the sweeps, including the baseline. The value stored for this method was dependent on the window settings. As the windows were adjusted the average varied, as one would expect from averaging different regions of an exponential. Because of this, the voltage amplitude derived was only indirectly related to the maximum voltage of the pulse. In order for this method to produce the same amplitude for two identical pulses, they would have to have the same decay rate and the same windowed region. Using this method, it was possible to make an estimate of the baseline noise by later fitting the baseline instead of the triggered peaks.

The third form of analysis was to simply find the maximum voltage (or minimum for negative pulses). The window was positioned around $t = 0$ and the maximum (or minimum) voltage recorded was used as the voltage amplitude.

The voltage amplitudes produced by each of these methods were stored as single-precision numbers in a data file. These data files, referred to as histogram

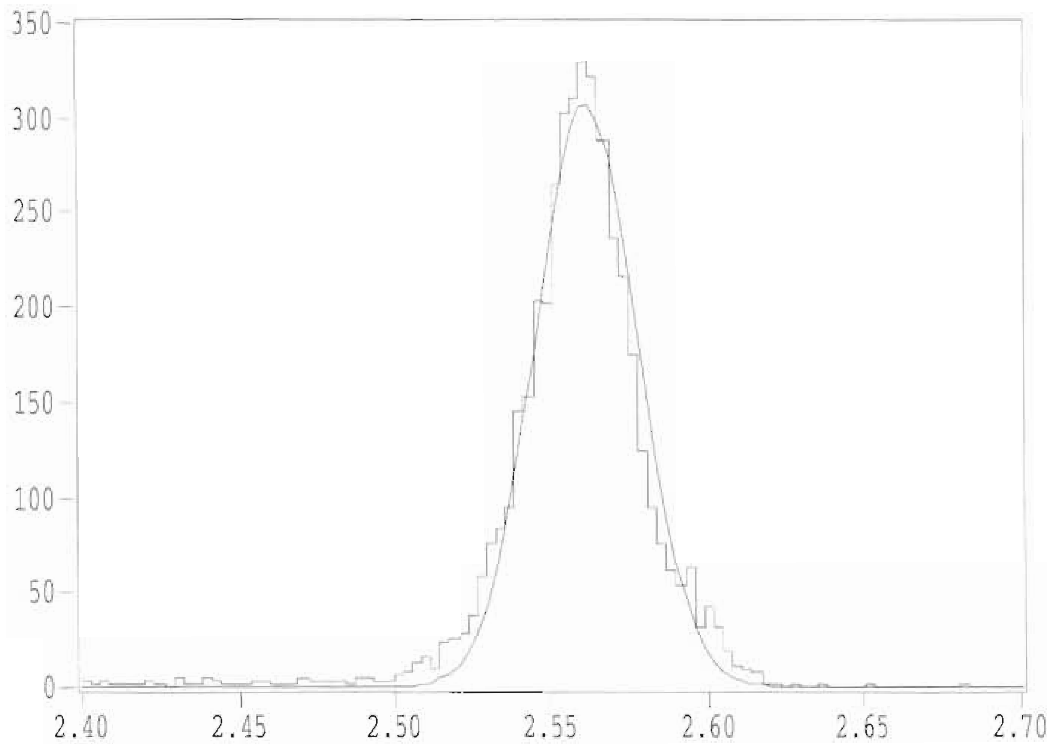

Figure 5.12: Gaussian least squares fit a histogram data file. The histogram fit is shown by the smooth curve and the data file is the step function. The histogram is artificially displayed as a smooth function, despite the fact that it was only evaluated at the discrete histogram bin values.

files (".has")[32]. In this file, all -99 values were known to be caused by "not a number" fits and were therefore ignored by all histogram fitting routines.[33]

The histogram files were read into memory and assembled into a histogram with a specified number of bins. At this point, the histograms were automatically fit with a Gaussian (A sample is shown in Figure 5.12).

The histogram fit parameters (i.e. the peak location, the peak width, and

[32]The files were called "*.has" for Averaged HiStogram files using the identical naming convention as the signal files (except for the file extension).

[33]It was impossible for there to be any true -99 volt pulses, as the maximum voltage difference that the data acquisition card could measure was 20 volts. It was possible, however, for a sweep to have a pulse amplitude when fit by an exponential of exactly -99 volts; but it was highly unlikely.

the overall normalization (or peak height)) were then extracted from:

$$Gaussian = \frac{norm}{\sigma\sqrt{2\pi}} exp\left[-\left(\frac{x - peak}{4\sigma}\right)^2\right]. \tag{5.3}$$

The normalization is needed because a portion (a least one eighth) of all the data will not be located in the peak region. This relationship gives a full-width half maximum of $\sqrt{8ln(2)}\ \sigma$. This is the value that will be considered to be the voltage resolution. In order to encourage the fit to arrive at the global minimum, the peak value was initially seeded to be the maximum bin number. The parameters are then all repetitively varied in order to find the least squares fit for the histogram [Bev92]. The program that calculates the Gaussian fit was written primarily in LabVIEW. However, to increase speed considerations, the repeated routines were written in C[34] and were linked and compiled as stand alone subroutines. These C routines were then called by the LabVIEW program to perform the iterative fitting function.

Additional filtering of the data files before processing was performed for data sets with large count rates relative to the decay times in order to remove pulses that were positioned on the tails of previous pulses. The pretrigger scans were linearly fit and the associated sweeps were rejected if the fit had an appreciable slope. Further filtering methods have been proposed by a number of groups, but were not found to yield a significant improvement on the energy resolution [Dep93, Mas94, Szy93].

5.4 Software

Because it was written using a graphical programming language, the software for this project can not be displayed in text format. However, as an example of

[34]LabVIEW allows for the inclusion of optimized compiled external routines, code interface nodes, to be called from within a LabVIEW VI. This has been shown to greatly increase the speed of non-graphical numerical routines.

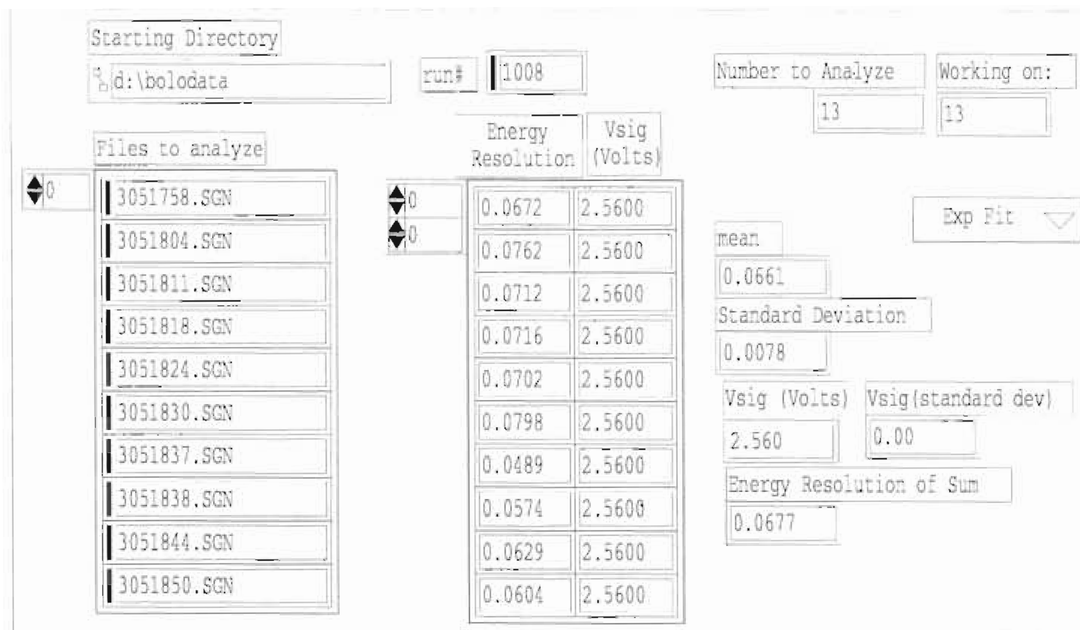

Figure 5.13: This shows the front panel of the master data analysis routine.

this code. the main data analysis routine front panel and G code are shown in figures 5.13 and 5.4. The code is currently available via the web.[35] The Gaussian fit routine is an exception as it was written in C and is listed in Appendix A. This code must be compiled and linked to the LabVIEW routines for the data analysis routines to run properly on any platform not operating in a 32 bit Windows operating environment. Except for this one routine. the code should be platform independent.

[35] http://www.physics.unc.edu/~junkin/labview/ or http://www.tunl.duke.edu/~junkin/labview/

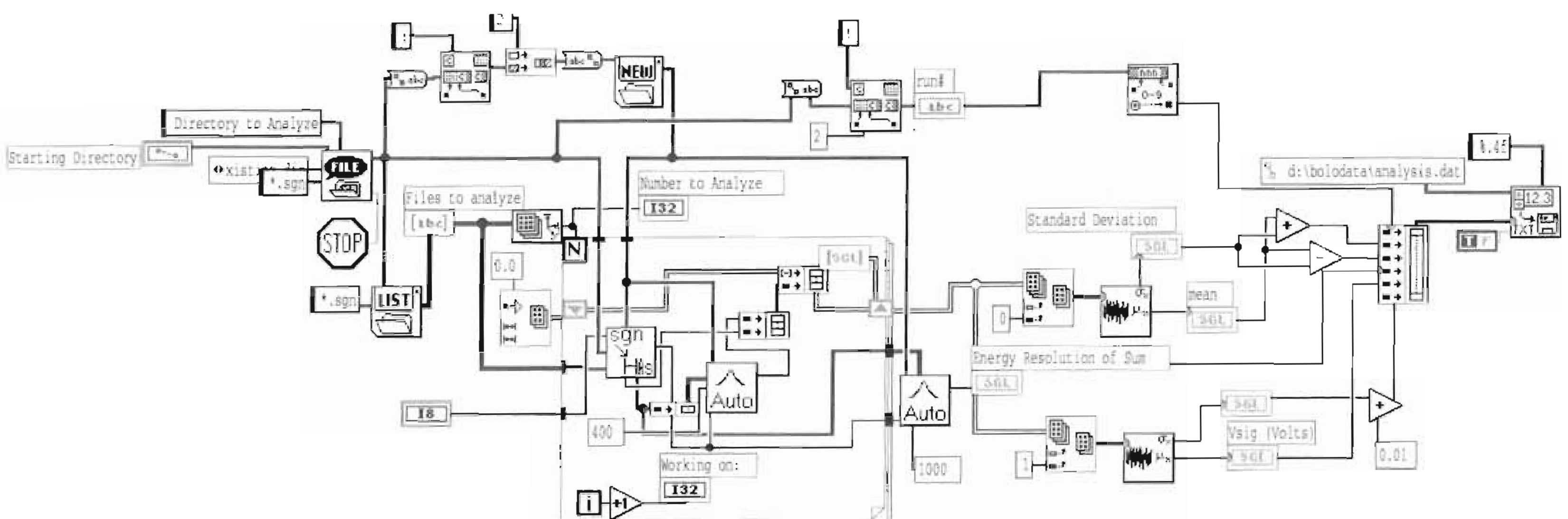

Figure 5.14 This shows the diagram for the master data analysis routine. The individual pulses are fit using the prescribed method in the SGN→HIS subroutine and the histogram is displayed and fit with a Gaussian in the auto Gaussian routine (AUTO).

Chapter 6

Data

Through the course of this work more than forty successful cool-downs of the dilution refrigerator have been performed, during which a variety of measurements of dynamic and static device properties have been measured. The results that are presented here are merely the most recent of a series of improvements and tests undertaken in order to gain an understanding of the electronic and thermal responses of microcalorimeters. With this work, there have been far more experiments conducted than can be presented in detail here. We have performed tests using three different types of thermistors heated by both radioactive sources and by resistive heating. A collection of more than fifteen amplifiers and preamplifiers have been constructed and characterized using both single-sided and dual symmetric biasing circuits. The data will be presented as a single contiguous path from tests that determined the initial bias current, to the final linear voltage response of the devices. This section will not document the many paths that have lead to this point in the research.

This chapter will present only the measurements obtained with the $Au_xGe_{(x-1)}$ devices, as the failures and short-comings of the P:Si chips have already been documented in section 2.1. There were two different sizes of $Au_xGe_{(x-1)}$ chips used in this work: 6 mm × 6 mm and 1 mm × 1 mm. Initial tests were performed with the larger chips using the resistive patterns designed by Wang and

Martoff [Wan95]. The data presented here were collected using the small chips developed specifically for this project.

6.1 Determining Bias Conditions

The initial step in acquiring data was to determine the optimum bias current for the microcalorimeters. In order to determine the bias current, runs were performed at the minimum stable operating temperature (130 mK) while varying the bias voltage and hence bias current. The detector was irradiated by alphas from ^{241}Am. A few pulse sweeps were acquired in order to determine the average voltage peak height and energy resolution of the α peak, which are shown in Figure 6.1. The minimum energy resolution was realized with a bias voltage of approximately 30 mV, yielding a bias current of $\approx$ 3 nA.

One important feature to glean from these plots is that the energy resolution is inversely dependent upon the voltage response of the device. To first order, this is a function of a relatively constant noise level and so the increased voltage response will increase the signal to noise ratio. A second piece of information to notice from Figure 6.1(a) is that as the bias increases, the sensitivity reaches a maximum of around 30 mV. The rolloff at higher bias is the result of an increase of the base operating temperature of the microcalorimeter as a result of resistive heating. From equation 1.4 it can be realized that as the temperature increases, the sensitivity decreases. Since the voltage response is dependent upon both the sensitivity and the bias current, an ideal operating bias voltage is realized at the maximum voltage response. Having determined the ideal bias conditions, this bias value was utilized in future measurements.

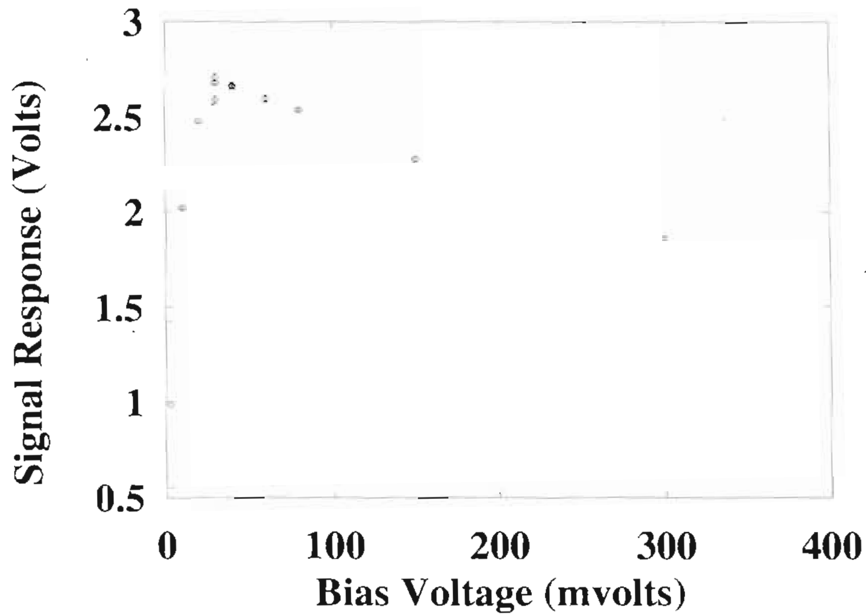

(a) Voltage (× 1020) versus bias voltage.

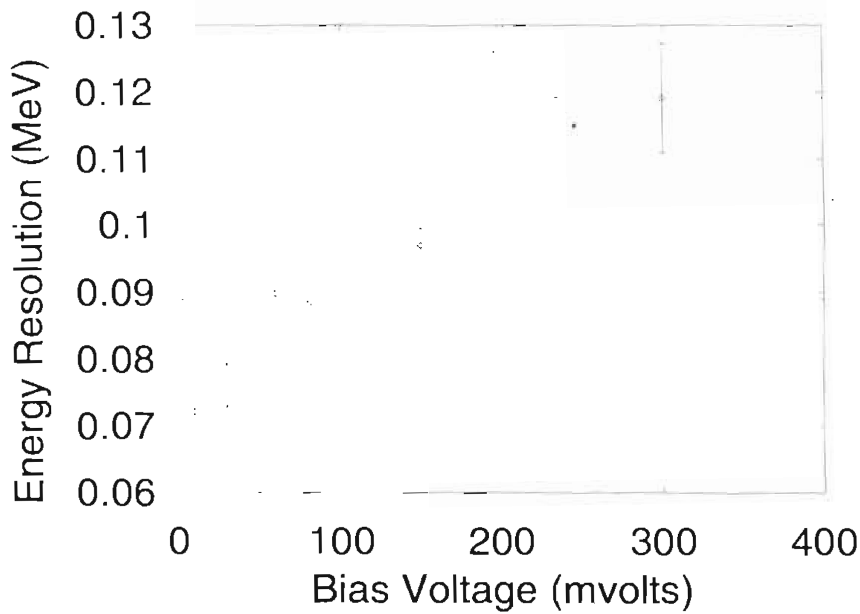

(b) Energy resolution versus bias voltage.

Figure 6.1: The microcalorimeter voltage response and energy resolution due to a 5.5 MeV α-particle versus bias voltage.

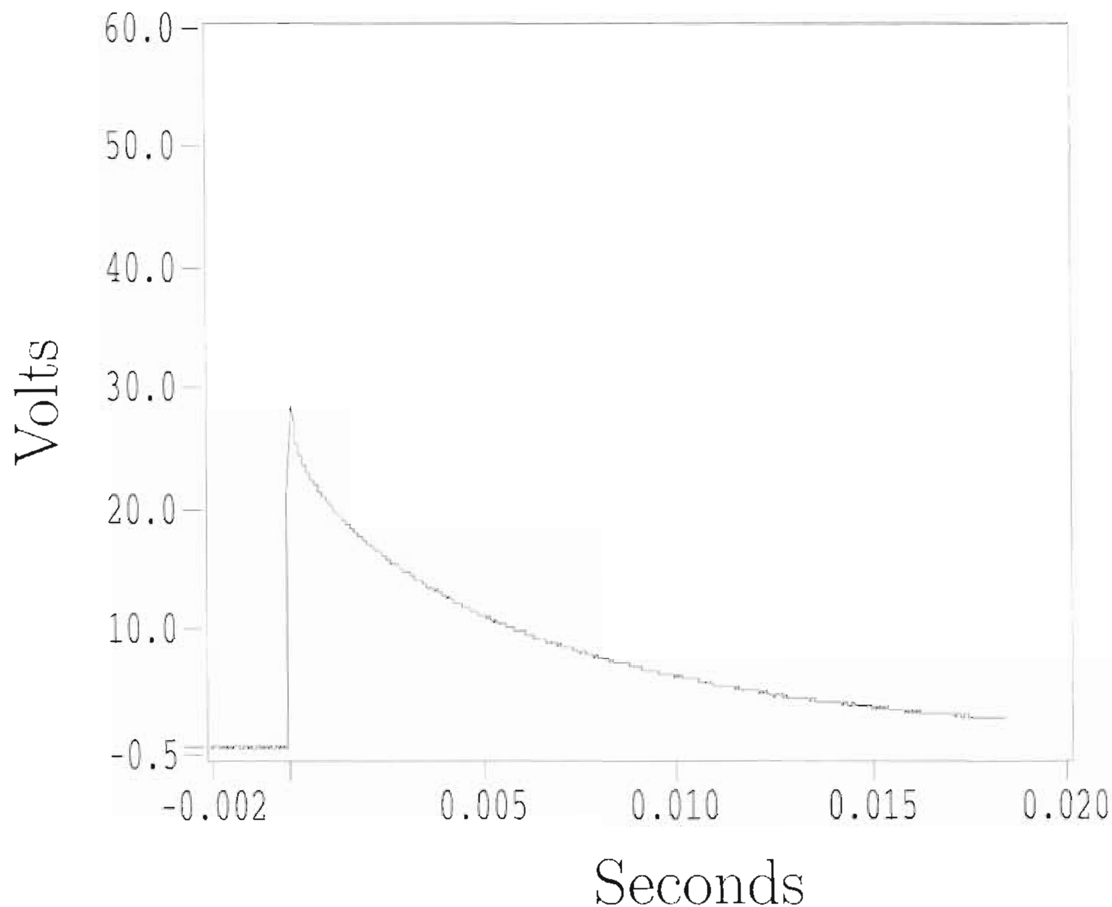

Figure 6.2: Amplified voltage response due to an incident α particle.

6.2 Comparison of Analysis Methods

The small $Au_xGe_{(x-1)}$ chip was exposed to a 3 kBq (0.1 μCi) ^{241}Am source[36] at a distance of 1.27 cm (0.5 inches). This geometry corresponded to a solid angle of $1.9 \times 10^{-1}\ \pi$, which implies an α particle count rate of 2.3/s.[37] For these measurements, a count rate of 2.4 ± 0.2 α particles/s was measured. The voltage response from absorption of a single α-particle is shown in Figure 6.2. This pulse has a primary thermal relaxation time of 8.6 ms compared to the

[36] This is an open source with a total contained radioactivity 3.91 kBq [Iso94].

[37] Using a computer model (BABEL) α particles of energies less than 30 MeV were calculated to stop in the Si chip. This does not take into account particles that hit the Al wires or near the edge.

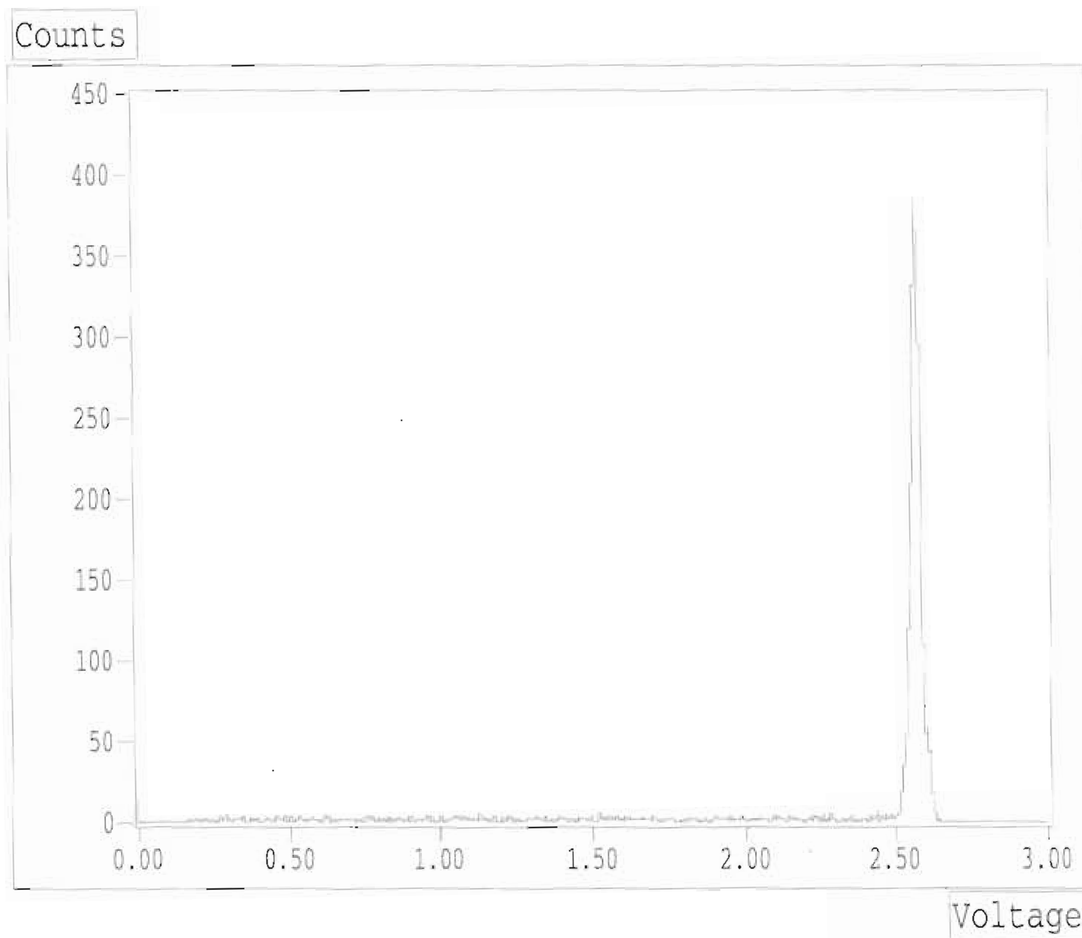

Figure 6.3: Voltage histogram of data analyzed using the *exponential* fit method.

predicted value of 32 ms calculated in section 4.2. The measurement of the rise time of this pulse is limited by the sampling rate of our data acquisition card (see section 5.2) and the high frequency limitation of the electronics (see Figure 5.7). The voltage sweeps from an entire run are then converted to a histogram as discussed in section 5.3.

A single data set has been analyzed using the three different methods: exponential, average, and peak fit, as discussed in section 5.3. The voltage histogram is normalized to the 5.5 MeV α-peak from the source. The voltage spectrum for the exponential fit is shown in Figure 6.3. This is calibrated to an energy spectrum in Figure 6.2 which is compared to the average and peak method in

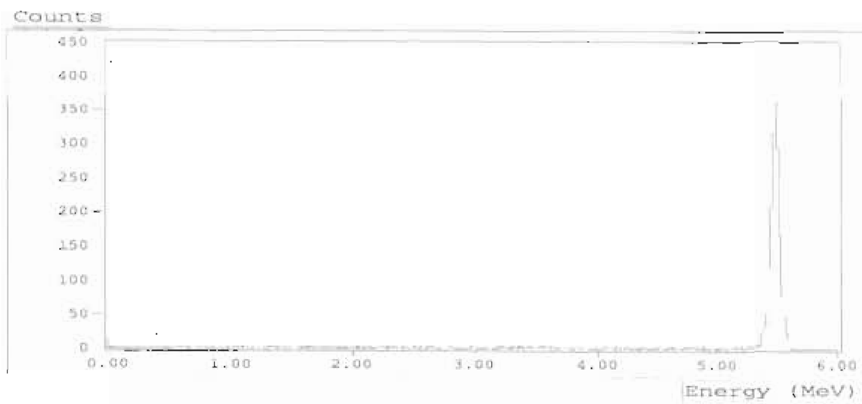

(a) Histogram of data analyzed using the *exponential* fit method.

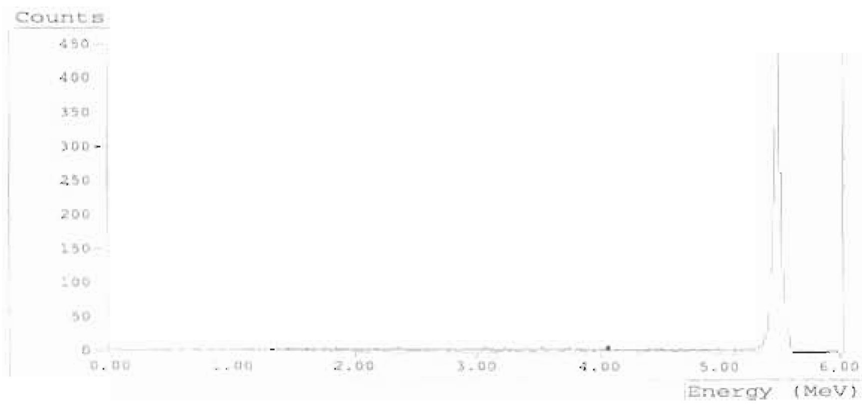

(b) Histogram of data analyzed using the *average* fit method.

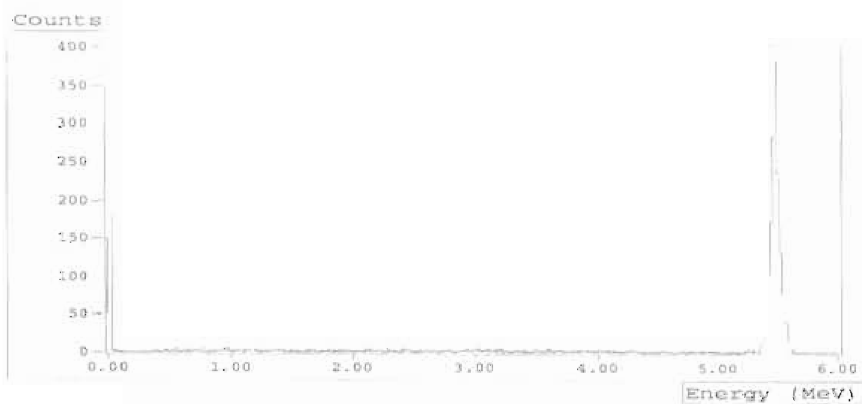

(c) Histogram of data analyzed using the *peak* fit method.

Fitting method	Voltage Peak (Volts)	Peak Energy Resolution (keV)	Baseline Resolution (keV)
Exponential	2.54	66.1	
Average	2.10	60.8	8.9
Peak fit[38]	2.78	68.4	20.5

Table 6.1: Comparison of the three analysis methods.

Figure 6.2. Data have been analyzed using all three analysis methods and the comparison is shown in Table 6.1. Since the three methods are all shown to produce relatively similar energy resolution, the exponential fit will be used to analyze the remaining data. Recall that the voltage returned by the fit is not dependent upon the window settings. The exception to this will be the baseline analysis used to determine the zero point energy which will be analyzed using the average method.

6.3 Voltage and Energy Correlation

In order to determine the voltage response of our microcalorimeters, pulses from a variety of sources have been analyzed. The measured voltage is then correlated to an energy using the known or predicted energy of the given source. Regardless of the source used, the zero energy value can be determined by analyzing the steady state condition which is acquired in every eighth voltage sweep while acquiring data. These baseline sweeps are analyzed using both the peak method and the average method. These peaks are visible in these two respective histograms and are located around zero voltage. The fit to the baseline using the two methods is shown in Table 6.1. These numbers also establish a maximum achievable limit for the energy resolution due to background electrical noise. As would be expected from random fluctuations in the noise, the averaged baseline

[38]This method requires the window to be reset (see section 5.3 for details

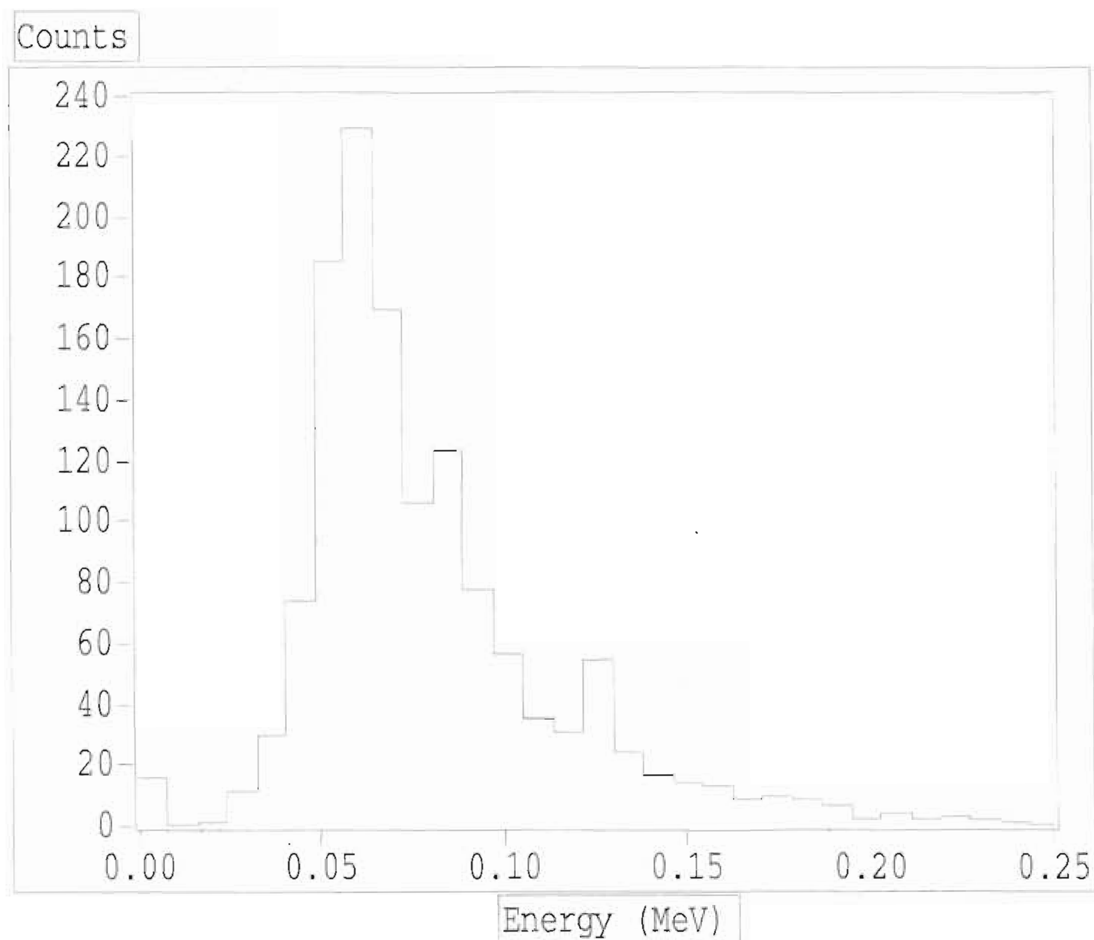

Figure 6.4: Histogram showing the lower region of the energy spectrum from an open source ^{241}Am. The lower energy cutoff in the measured spectrum is caused by the threshold of the trigger during data acquisition.

data has a significantly better resolution than the peak method.

6.3.1 Energy Calibrations from ^{241}Am Photons

Lowering the trigger voltage threshold allowed measurements of the low energy region of the ^{241}Am spectrum as shown in Figure 6.4. The energy for the lower region is calibrated using the 5.5 MeV α peak. There are also low-energy events produced by the γ-rays and x-rays from the daughter nucleus (^{237}Np). The photon and α particle energies are shown in Table 6.2 with their decay percentages relative to the total decay rate of ^{241}Am. Since the ^{241}Am source is

Energy (keV)	Source	Percentage
5485.6	α	85.2%
5412.9	α	12.8%
5388	α	1.4%
59.5	γ	35.8%
26.4	γ	2.4%
20.8	X Ray	4.9%
17.8	X Ray	19.4%
13.9	X-Ray	13.3%

Table 6.2: α and photon intensities from ^{241}Am relative to an ^{241}Am decay [Fir96, Kno89].

not covered, it is possible for the recoiling ^{237}Np nucleus to escape, carrying up to 90 keV of kinetic energy which makes up the balance of the measured spectrum.

A spectrum was then collected in which the source was covered with a 0.025 mm (1 mil) stainless-steel foil, sufficent to stop all of the α particles and recoils while only slightly attenuating the photons [Sto70]. This spectrum is shown in Figure 6.5. It is worth noting that the upper voltage region shown in Figure 6.5(a) is relatively clean, showing that there is very little background above the 0.4 V peak (corresponding to 60 keV).

6.3.2 Energy Calibration from ^{137}Cs γs

A ^{137}Cs source with a dominant high energy gamma of 661.6 keV was placed against the side of the cryostat. And a combined ^{137}Cs/^{241}Am spectrum is shown in Figure 6.6. The low energy photons from the ^{241}Am are removed by normalizing the data shown in Figure 6.5 by the acquisition time and subtracting those from the combined ^{241}Am and ^{137}Cs data. The net data can be compared to the

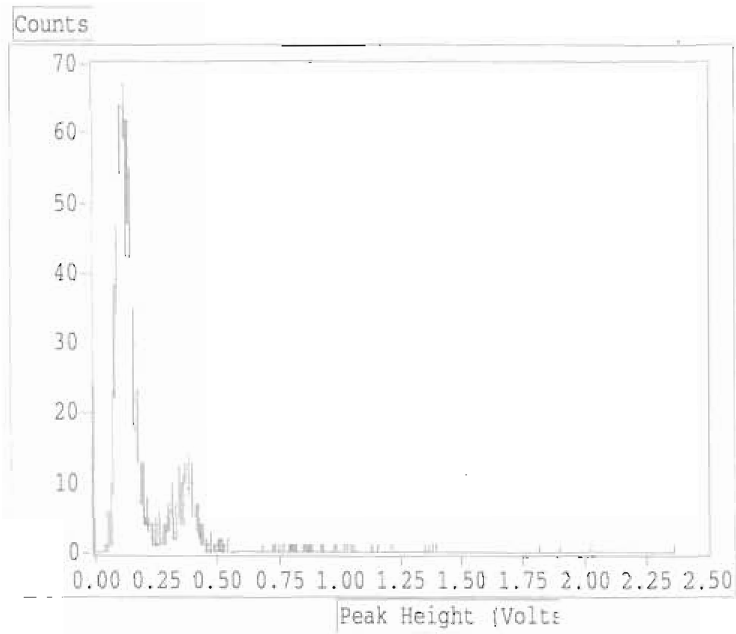

(a) ^{241}Am voltage spectrum.

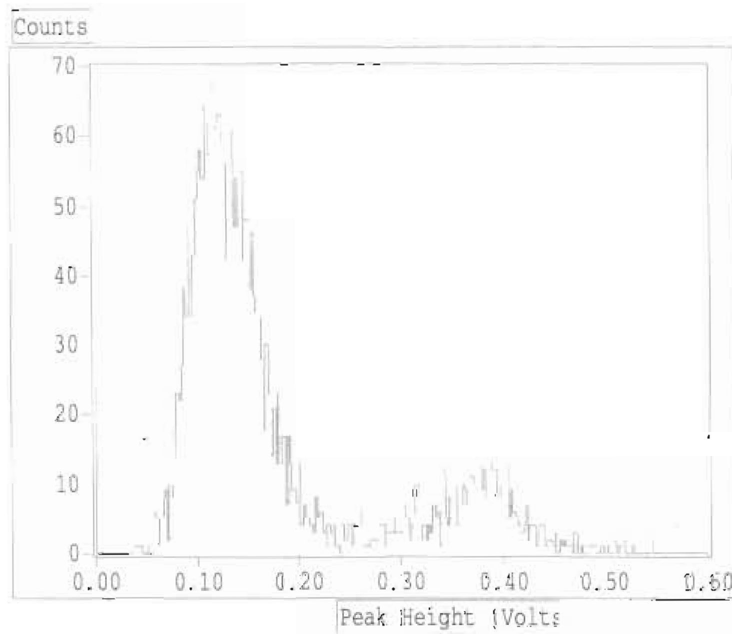

(b) Low energy portion of the ^{241}Am voltage spectrum.

Figure 6.5: ^{241}Am voltage spectra which are proportional to energy spectra. This data was acquired using the covered ^{241}Am source.

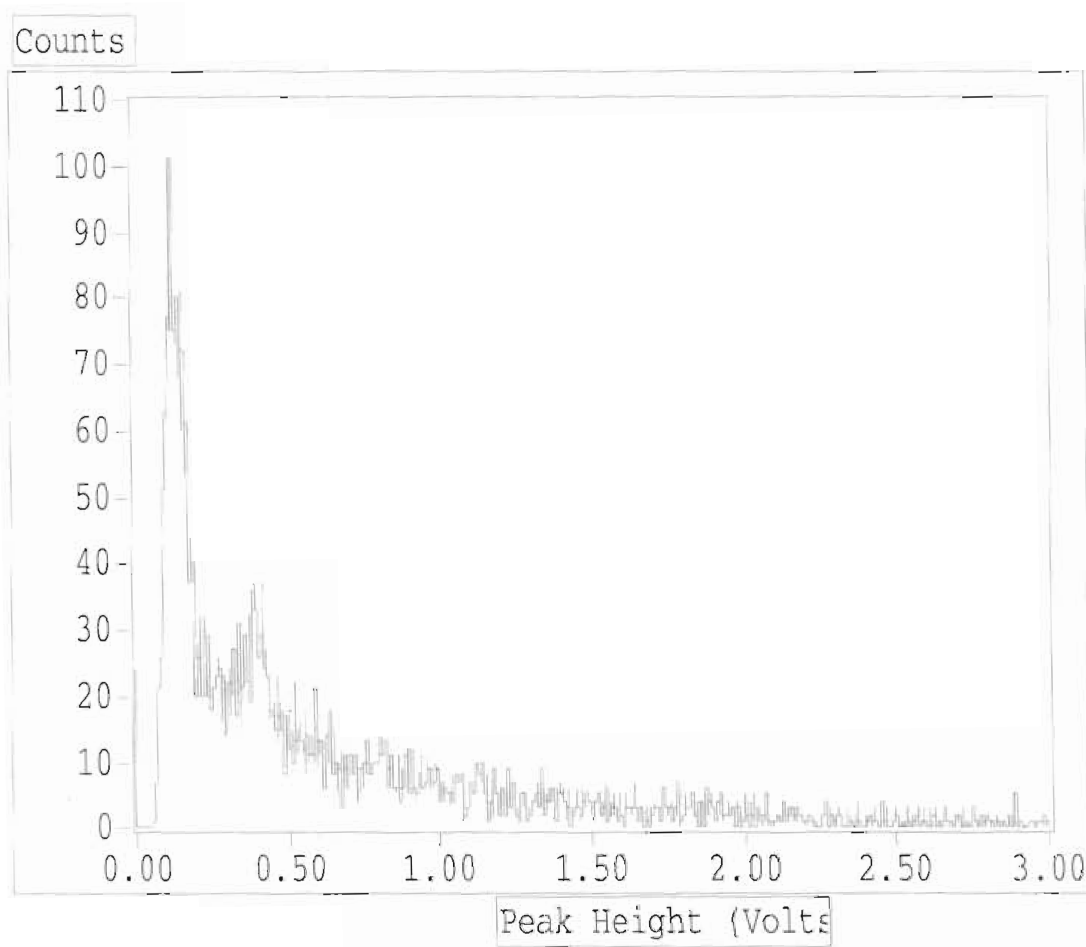

Figure 6.6: ^{137}Cs and ^{241}Am voltage spectrum acquired in 12.1 hours.

predictions made from EGS4[39] for a 661 keV gamma ray beam incident on a Si plane 0.04 cm thick shown in Figure 6.7. The maximum amount of energy that these high energy γs can deposit is from 180° Compton scattering. Therefore, this Compton edge from the 661 keV γs occurs at 480 keV. There is not a sharp absorption peak at this edge because the electrons that are produced at these high energies are typically too energetic to stop in the Si chip. [Kno89, Kra88]

[39]EGS4 [Bie92] is a routine package designed to assist with the development and production of FORTRAN code for tracking high energy photons, electrons and positrons through a medium using a Monte Carlo simulation [Nel85]. Because EGS4 was designed for high energy reactions, it was unable to produce a realistic model of the low energy photons emitted from the ^{241}Am

The energy calibration is performed by normalizing the measured data to predicted data. The log of the data is shown in Figure 6.8 in order to emphasize the Compton edge which dominated the fit.

6.4 Linearity of Microcalorimeter Response

The voltage response as a function of energy with a linear fit to the data is shown in Figure 6.9. The data comes from the sources listed in Table 6.4. The voltage peak from the 5.5 MeV αs are determined from a Gaussian fit of the data as discussed in section 5.3. The error bars represent the uncertainty in the peak fit,[40] and the discretization effects arising from binning into histograms. This same technique is used for determining the energy resolution of the 59.6 keV γ peak and the baseline (at zero voltage). The energy resolution for the 29.6 keV γ peak is determined by fitting the upper edge of the low energy peak. The entire peak could not be fit for two reasons: the low voltage cutoff is a manifestation of the trigger level, and the peaks are broad enough that the individual ^{241}Am photon peaks are not discernible. The ^{137}Cs data is represented with a single coefficient which is plotted at the Compton edge energy; this cutoff energy predominantly determines the fitting coefficient. The error in this measurement is determined by the fit uncertainty. The equation used to fit the data is

$$Energy(keV) = 214 \pm 12 \left(\frac{keV}{V}\right) Voltage - 0.67 \pm 3.04 (keV) \qquad (6.1)$$

with the errors coming from the uncertainty in the fit [Bev92].

[40] Error analysis of these various fits was obtained using both MATHEMATICA [Wol91, Wol97] and the autogaussian LabVIEW routines.

[41] The actual voltage was 2.56 V recorded with a gain of 1071 (21×51).

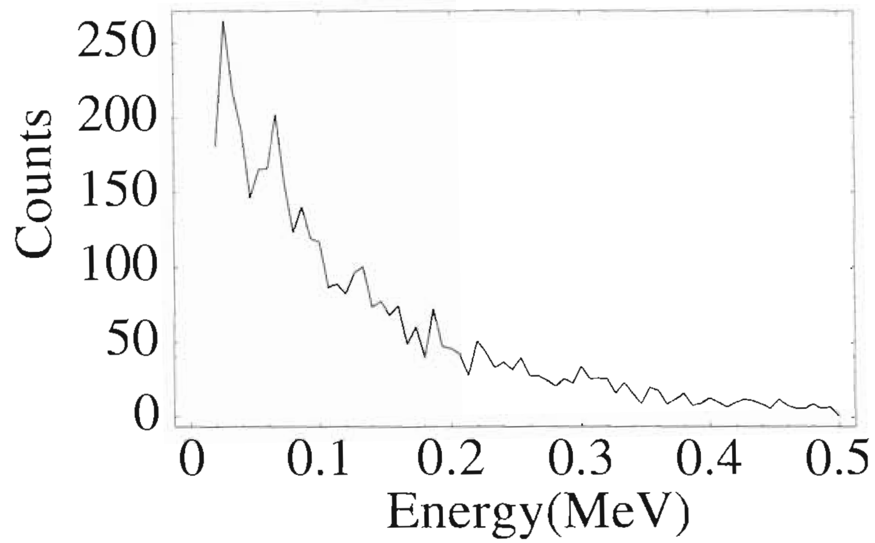

(a) Energy spectrum (scaled using the predicted ^{137}Cs data) produced by γs from ^{137}Cs with the ^{241}Am background removed.

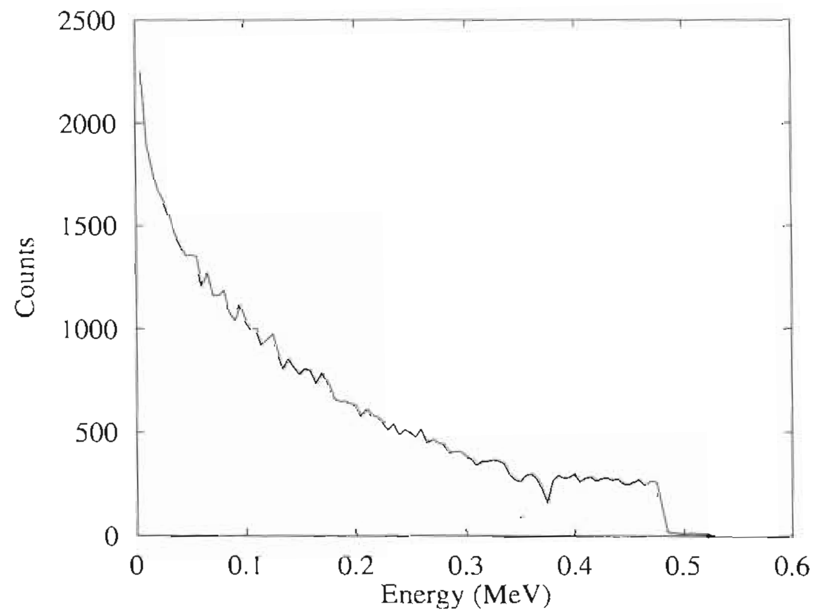

(b) EGS4 prediction of the energy deposited in on a 0.4 mm^3 Si chip by γs from ^{137}Cs.

Figure 6.7: Comparison of predicted and recorded energy spectrum from ^{137}Cs.

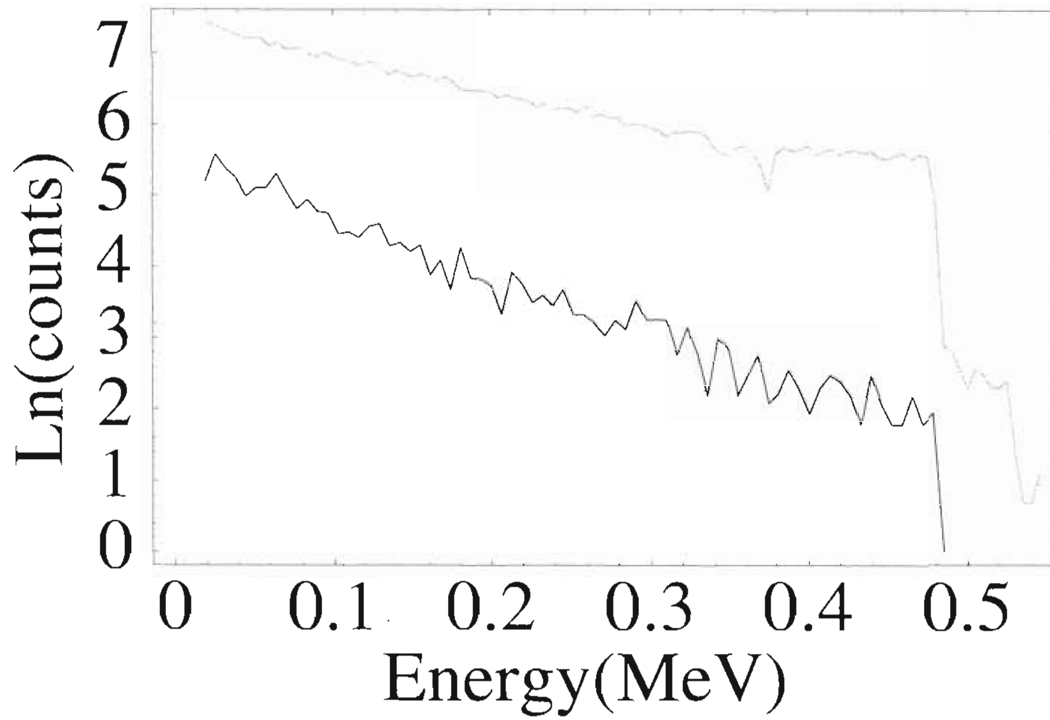

Figure 6.8: Log plots of spectrum used for energy calibration from the ^{137}Cs data. The dark line is the measured data and the solid line is the EGS4 prediction.

Particle	Source	Energy (MeV)	Measured Peak (Volts)	Error (Volts)	FWHM (MeV)
α	^{241}Am	5.5	24.541	0.26	0.06
γ	^{137}Cs	0.478	2.899	0.071	0.036
γ	^{241}Am	0.0596	0.3533	0.0631	0.032
γ	^{241}Am	0.0296	0.104	0.0418	0.021
	Baseline	0	0.00242	0.00035	0.009

Table 6.3: Energy and voltage peak values (gain = 10251) used for energy calibration.

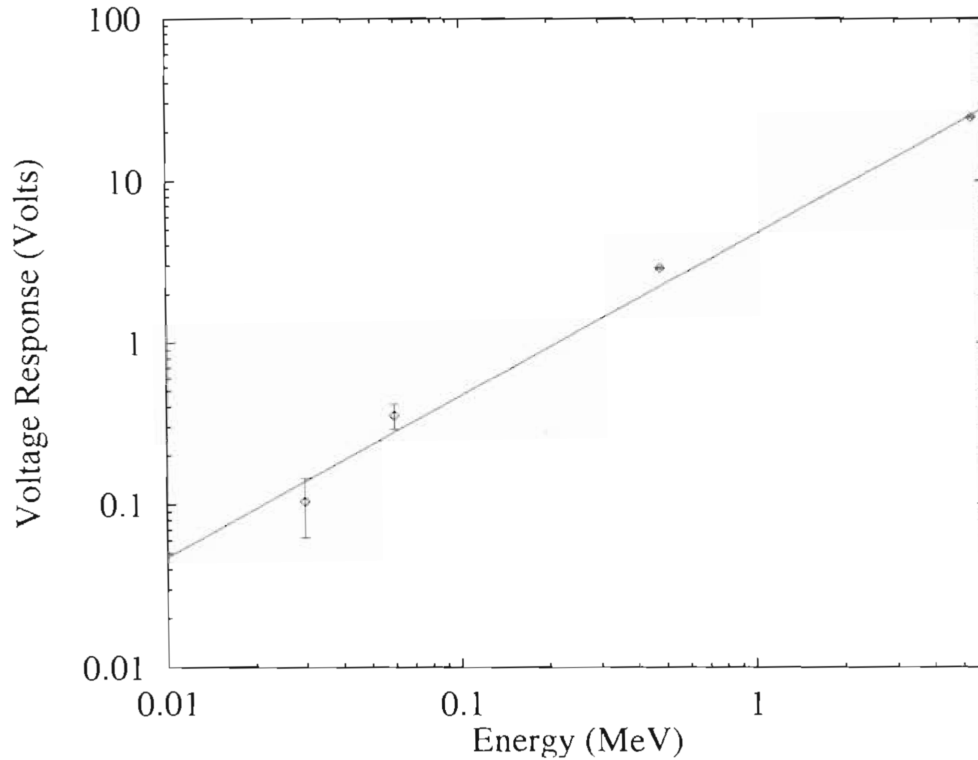

Figure 6.9: Voltage response of microcalorimeter (gain of 10251) versus energy deposited from the ^{241}Am and ^{137}Cs sources.

6.5 Improving the Resolution

The desired energy resolution of our devices was approximately 1 keV. Improvements in this energy resolution are possible from three different sources: the thermistors, the operating temperature, and the electronics, that will allow the realization of this goal. From Table 5.1 the theoretical minimum noise for these devices was shown to be resistor noise which places a limit of $\approx$10 μV at the input of the JFET-preamplifier. This translates to a total energy resolution (using the voltage energy relationship derived in section 6.3) of 20 keV. Future work should minimize the bias current and bias resistance in order to limit the dominance of this term.

As discussed in section 2.3 the desired sensitivity for the thermistor is between 3 and 4 which contrasts with the present devices that have values of $\approx$ 6. In order

to have devices that operate with the desired sensitivity, additional $Au_xGe_{(1-x)}$ thermistors with slightly lower Au concentrations would need to be produced.

In order to improve the resolution of the *current devices*, the stable base operating temperature for the dilution refrigerator should be decreased to permit microcalorimeter operation below 0.1 K with the JFET-preamplifier maintaining the current operating temperature. This will require better thermal isolation of the preamplifier and additional heat sinking of the leads attached to the mixing chamber.

Chapter 7

Conclusion

Through interdisciplinary work in nuclear physics, low temperature physics, statistical mechanics, electronics and computer science, this project has produced functioning microcalorimeters. P:Si thermistors have been developed and tested. These have been found to have unpredictable resistance versus temperature curves and are therefore not well suited for mass-produced microcalorimeters. In contrast, $Au_xGe_{(1-x)}$ thermistors have been fabricated, tested, and found to have predictable performance that enables them to be used in cryogenic detectors. A dilution refrigerator has been constructed that is able to continuously cool the detector system to 130 mK. Electronics have been developed that operate inside the dilution refrigerator and amplify voltage changes across the thermistor. A data acquisition and analysis system has been constructed, and corresponding software written to collect and convert the acquired voltage pulses into an energy spectrum.

These microcalorimeters have measured α and γ particles from 20 keV to 5.5 MeV. Nuclear sources have been used to calibrate these devices demonstrating their linear energy response over a range of more than two orders of magnitude.

The next step for this project is to optimize the bias resistors for use with the present $Au_xGe(1-x)$ thermistors in order to reduce the effects of the electronic noise. This should enable the microcalorimeter resolution to be improved to a

level that the individual low energy photons in the ^{241}Am spectra will be clearly resolved. This work will then concentrate on developing nondestructive methods of attaching absorbers to microcalorimeters.

Appendix A

Gaussian Fit Routines

These routines were written to be used within a code interface node in LabVIEW. These procedures will then need to be compiled and linked for proper operation.

```
/*
 * CIN source file fullgfit.c
 */
#include "extcode.h"
/* stubs for advanced CIN functions */

UseDefaultCINInit
UseDefaultCINDispose
UseDefaultCINAbort
UseDefaultCINLoad
UseDefaultCINUnload
UseDefaultCINSave

/*
 * typedefs
 */

typedef struct { /*Data*/
int32 dimSize;
int32 arg1[1];
} TD1;
typedef TD1 **TD1Hdl;

typedef struct { /*Gaussian Fit to Data*/
```

```
int32 dimSize;
float32 arg1[1];
} TD2;
typedef TD2 **TD2Hdl;

extern float32 gfitsub(int32 Number_of_Bins,
 int32  *Data,
 float32 *Fitting_Factor,
 float32 *Peak,
 float32 *Sigma,
 float32 *Gausian_Fit,
 int32 *Number_of_Counts);

CIN MgErr CINRun(float32 *Factor,
 float32 *delta_Factor,
 float32 *peak,
 float32 *delta_Peak,
 float32 *Sigma,
 float32 *delta_Sigma,
 int32 *Number_of_Counts,
 TD1Hdl Data,
 TD2Hdl Fit_Data,
 float32 *MSE);

CIN MgErr CINRun(float32 *Factor,
 float32 *delta_Factor,
 float32 *peak,
 float32 *delta_Peak,
 float32 *Sigma,
 float32 *delta_Sigma,
 int32 *Number_of_Counts,
 TD1Hdl Data,
 TD2Hdl Fit_Data,
 float32 *MSE)

{
int32 loopcount,*tempdata,datalength;
float32 oldmse,*tempfitdata;

tempdata = (*Data)->arg1;
tempfitdata = (*Fit_Data)->arg1;
datalength = (*Data)->dimSize;
```

```
*MSE=gfitsub(datalength,tempdata,Factor,peak,
Sigma,tempfitdata,Number_of_Counts);

/*
        Peak Adjustment------------------------
*/
loopcount = 50;
do                  /*Peak increase*/
   {
loopcount--;
*peak += *delta_Peak;
oldmse = *MSE;
*MSE=gfitsub(datalength,tempdata,Factor,peak,
Sigma,tempfitdata,Number_of_Counts);
} while((*MSE <= oldmse) & (loopcount>0));

loopcount = 50;

do                  /*Peak decrease*/
  {
loopcount--;
*peak -= *delta_Peak;
oldmse = *MSE;
*MSE=gfitsub(datalength,tempdata,Factor,peak,
Sigma,tempfitdata,Number_of_Counts);
} while((*MSE <= oldmse) & (loopcount>0));
*peak += *delta_Peak;
/*
Sigma Adjustment------------------------
*/
loopcount = 50;
do                  /*Sigma increase*/
   {
loopcount--;
*Sigma += *delta_Sigma;
oldmse = *MSE;
*MSE=gfitsub(datalength,tempdata,Factor,peak,
Sigma,tempfitdata,Number_of_Counts);
} while((*MSE <= oldmse) & (loopcount>0));

loopcount = 50;
do                  /*Sigma decrease*/
   {
```

```
loopcount--;
*Sigma -= *delta_Sigma;
oldmse = *MSE;
if (*Sigma>0)
*MSE=gfitsub(datalength,tempdata,Factor,peak,
Sigma,tempfitdata,Number_of_Counts);
} while((*MSE <= oldmse) & (loopcount>0) & (*Sigma>0));
*Sigma += *delta_Sigma;
/*
Factor Adjustment-----------------------
*/
loopcount = 50;
do                  /*Factor increase*/
   {
loopcount--;
*Factor += *delta_Factor;
oldmse = *MSE;
*MSE=gfitsub(datalength,tempdata,Factor,peak,
Sigma,tempfitdata,Number_of_Counts);
} while((*MSE <= oldmse) & (loopcount>0));

loopcount = 50;
do                  /*Factor decrease*/
   {
loopcount--;
*Factor -= *delta_Factor;
oldmse = *MSE;
*MSE=gfitsub(datalength,tempdata,Factor,peak,
Sigma,tempfitdata,Number_of_Counts);
} while((*MSE <= oldmse) & (loopcount>0));
*Factor += *delta_Factor;

return noErr;
}
```

```
/*
 * gfitsub.c for fullgfit.c  CIN
 */
#include "extcode.h"
/*
 * typedefs
 */
float32 LVSBMain(int32 Number_of_Bins,
 int32  *Data,
 float32 *Fitting_Factor,
 float32 *Peak,
 float32 *Sigma,
 float32 *Gausian_Fit,
 int32 *Number_of_Counts);

float32 LVSBMain(int32 Number_of_Bins,
 int32  *Data,
 float32 *Fitting_Factor,
 float32 *Peak,
 float32 *Sigma,
 float32 *Gausian_Fit,
 int32 *Number_of_Counts)
      {

int   i;                  /*loop counter used below */
float32 tempvar,temp2var;  /*two temp variables */
/* tempvar is used to store the constant figured out
from the input values */
/* temp2var is for temporary storage of MSE (Mean Square Error) */

temp2var=0.0;
tempvar = (*Fitting_Factor * (float32)*Number_of_Counts)/
(2.5066 * *Sigma);
for(i=0; i<Number_of_Bins; i++)
{
Gausian_Fit[i] = tempvar *
exp(- ((*Peak-i)*(*Peak-i))
/(2.0 * *Sigma * *Sigma));
temp2var += (Gausian_Fit[i] - Data[i]) *
      (Gausian_Fit[i] - Data[i]);
}
return  (temp2var / ((float32) Number_of_Bins));
      }
```

REFERENCES

[Ale88] A. Alessandrello et al. *Heat Capacity of P-Doped Si Thermistors at Low and Very Low Temperature Measured by Alpha-Particle and X-Rays.* Europhysics Letters, **7**(1988) 69–75.

[Ale93] A. Alessandrello et al. *TeO_2 bolometers to search for Double Beta Decay of ^{130}Te: status of art.* Journal of Low Temperature Physics, **93**(1993) 201–206.

[Ana94a] Analog Devices. *Design-in Reference Manual*, 1994. Ultralow Distortion, Ultralow Noise Op Amp:AD797.

[Ana94b] Analog Devices. *Design-in Reference Manual*, 1994. Low Noise, Precision Operational Amplifier: OP27.

[Ana94c] Analog Devices. *Design-in Reference Manual*, 1994. Next Generation OP07, Ultralow Offset Voltage, Operational Amplifier: OP77.

[And70] A. C. Anderson. *Elementary Dilution Refrigeration.* Review of Scientific Instruments, **41**(1970) 1446–1450.

[Ash76] N. W. Ashcroft and N. D. Mermin. *Solid State Physics.* Saunders College, Philladelphia, 1976.

[Bah87a] J. H. Bahcall. *Dark Matter Near the Sun: Is Ordinary Stuff the Right Stuff?*, volume four, pages 2–12. World Scientific, Singapore, 1987.

[Bah87b] J. H. Bahcall and S. Casertano. *Some Possible Regularities in Missing Mass*, volume four, pages 50–57. World Scientific, Singapore, 1987.

[Ban81] E. S. Banes, Jr. *LR-130 (Temperature Controller) Specifications.* Linear Research, San Diego, CA 92109, February 1981. Product users manual and additional private communication.

[Ber93] G. E. Berman et al. *New evidence against 17-keV neutrino emission in the β decay momentum spectrum of ^{35}S.* Physical Review C, **48**(1993) R1–R4.

[Bet76] D. S. Betts. *Refrigeration and Thermometry below One Kelvin.* Graduate Student Series in Physics. Sussex University Press, Toronto, 1976.

[Bet89] D. S. Betts. *An Introduction to Millikelvin Technology*. Number 1 in Cambridge Studies in Low Temperature Physics. Cambridge University Press, Cambridge, 1989.

[Bev92] P. R. Bevington and D. K. Robinson. *Data Reduction and Error Analysis for the Physical Sciences*. McGraw-Hill Book Co., New York, second edition, 1992.

[Bie92] A. F. Bielajew. *egs4unix_2.0*. (private communication), October 1992.

[Boo93] N. E. Booth et al. *Superconducting Tunnel Junction and Quasiparticle Trapping*. Journal of Low Temperature Physics, **93**(1993) 521–532.

[Boo96] N. E. Booth, B. Cabrera, and E. Fiorini. *Low-Temperature Particle Detectors*. Annual Review of Nuclear and Particle Science, **46**(1996) 471–532.

[Cal] Calogic Corp. *Dual N-Channel JFET Low Noise Amplifier*. 2N6483 2N6485.

[Cal76] F. P. Calaprice and B. R. Holstein. *Weak Magnetism and the Beta Spectra of ^{12}B and ^{12}N*. Nuclear Physics, **A273**(1976) 301–325.

[Cal88] D. O. Caldwell et al. *Dark Matter Search with Ge Detectors*. In *Low Temperature Detectors for Neutrinos and Dark Matter II*, pages 55–66, May 1988.

[Chi86] M. A. Chin et al. *Fast Response GeAu Heat Pulse Bolometer for Use in Ballistic Phonon, High MAgnetic Field Experiments*. In *Phonon Scattering in Condensed Matter V : Proceedings of the Fifth International Conference*, pages 395 – 397, June 1986.

[Coc83] E. Coccia and T. O. Niinikoski. *Thermal and Superconducting properties of an aluminum alloy for gravitational wave antennea below 1 K*. Journal of Physics E, **16**(1983) 695–9.

[Cor93] N. Coron et al. *Towards a Bolometric Dark Matter Detection Experiment: Underground Radioactive Background Measurements in the 3 keV - 5 MeV Energy Range with a Massive Bolometer at 55 mK*. Astronomy and Astrophysics, **278**(1993) L31–L34.

[Cro96] K. Croswell. *The Dark Side of the Galaxy*. Astronomy, **24**(1996) 41–45.

[DeB97] L. De Braeckeleer. *Phys 346: Electroweak Interactions in Nuclear,Particle and Astrophysics*. (and private communication), Spring 1997.

[DeL71] L. E. DeLong, O. G. Symko, and J. C. Wheatley. *Continuously Operating ^{4}He Evaporation Refrigerator*. Review of Scientific Instruments, **42**(1971) 147–150.

[Dep92] C. Depree. *A Feasibility study for the production of Cryogenic Bolometers*. Master's thesis, University of North Carolina at Chapel Hill, 1992.

[Dep93] D. Deptuck, M. M. Lowry, and I. C. Girit. *Signal Processing for Cryogenic Micro-Calorimetry*. Journal of Low Temperature Physics, **33**(1993) 275–280.

[Dep94] D. K. Deptuck. *Cryogenic Micro-Calorimeter Measurement of the 107Pd Beta Decay Spectrum*. Ph.D. thesis, Princeton University, November 1994.

[Die79] A. J. Diefenderfer. *Principals of Electronic Instrumentation*. Saunders, Philadelphia, second edition, 1979.

[Dod81] B. W. Dodson et al. *Metal-Insulator Transition in Disordered Germanium-Gold Alloys*. Physical Review Letters, **46**(1981) 46–49.

[Fab85] S. M. Faber. *Dark Matter: Key Issues*. In *Dark Matter in the Universe*, pages 1–12, June 1985.

[Fio93] E. Fiorini. *Physical Motivation for Thermal Detectors (Overview)*. Journal of Low Temperature Physics, **93**(1993) 189–200.

[Fir96] R. B. Firestone. *Table of Isotopes*, volume II: A = 151–272. John Wiley and Sons, Inc., New York, eighth edition, 1996.

[Fuk88] M. Fukugita. *Mass Density of the Universe and Dark Matter*. In *Dark Matter in the Universe: Proceedings of the third Nishininomiya-Yukawa Memorial Symposium*, pages 32–49, November 1988.

[Gal86] G. Gallinaro, C. Salvo, and S. Terreni. *Effect of heat link capacity on the energy pulse response of bolometers*. Cryogenics, **26**(1986) 9–11.

[Gar95] A. Garcia and B. A. Brown. *Shape of the β spectra in the A=14 system*. Physical Review C, **52**(1995) 3416–27.

[Ger95] G. Gerbier. *Dark Matter as Elementary Particles: To be or not to be*. In *Dark Matter in Cosmology Clocks and Tests of Fundamental Laws: Proceedings of the XXXth Rencontre De Moriond*, pages 139–148, January 1995.

[Glo90] K. Gloos et al. *Thermal Conductivity of Normal and Superconducting Metals.* Cryogenics, **30**(1990) 14–8.

[Gon88] L. Gonzalez–Mestres and D. Perret–Gallix. *Neutrinos,Dark Matter and Low Temperature Detectors.* In *Low Temperature Detectors for Neutrinos and Dark Matter II*, pages 1–36, May 1988.

[Hen71] H. E. Henrickson. *A Dilution Refrigerator Centering Device Which Introduces Minimal Heat Load.* Review of Scientific Instruments, **42**(1971) 1533–1534.

[Hus70] J. G. Hust. *Thermal Anchoring of Wires in Cryogenic Apparatus.* Review of Scientific Instruments, **11**(1970) 622–4.

[Irw96] K. D. Irwin et al. *X-ray detection using a superconducting transition-edge sensor microcalorimeter with electrothermal feedback.* Applied Physics Letters, **69**(1996) 1945–1947.

[Iso94] Isotope Production Laboratories, 30117 N. San Fernando Blvd.; Burbank, California 91504. *Certificate of Calibration Alpha Standard Source*, December 1994. Catalog No.: AF 241, Source No.: CC-169, IPL Ref. No.: 482-7.

[Jin88] Y. Jin et al. *^{14}C beta decay and the ^{14}N M1 from factors.* Physical Review C, **38(2)**(1988) 923–30.

[Kel93] R. L. Kelley et al. *Development of Microcalorimeters for High Resolution X-Ray Spectroscopy.* Journal of Low Temperature Physics, **93**(1993) 225–30.

[Khl95] M. Y. Khlopov. *Physical Arguments, Favouring Multicomponent Dark Matter.* In *Dark Matter in Cosmology Clocks and Tests of Fundamental Laws: Proceedings of the XXXth Rencontre De Moriond*, pages 133 – 138, January 1995.

[Kit86] C. Kittel. *Introduction to Solid State Physics.* John Wiley and Sons, Inc., New York, sixth edition, 1986.

[Kno89] G. F. Knoll. *Radiation Detection and Measurement.* John Wiley and Sons, New York, second edition, 1989.

[Kno93] W. B. Knowlton et al. *Ge-Au Eutectic Bonding of {100} Single Crystals.* Journal of Low Temperature Physics, **93**(1993) 343–348.

[Kot87] A. Kotlicki, M. Le Gros, et al. *SQUID Detection of Superheated Granules.* In *Low Temperature Detectors for Neutrinos and Dark Matter.* pages 37–43. May 1987.

[Kra88] K. S. Krane. *Introductory Nuclear Physics.* John Wiley and Sons, New York. 1988.

[Lou74] O. V. Lounasmaa. *Experimental Principles and Methods Below 1 K.* Academic Press, London, 1974.

[Lov87] M. S. Love and A. C. Anderson. *Heat Capacity of thick-film resistance thermometers below 1 K.* Review of Scientific Instruments. **58**(1987) 1113–4.

[Low61] F. J. Low. *Low Temperature Germanium Bolometer.* Journal of the Optical Society of America. **51**(1961) 1300–4.

[Low88] M. M. Lowry et al. *Status and applications of cryogenic detectors.* Hyperfine Interactions, **43**(1988) 507–517.

[Low93] M. M. Lowry, D. Deptuck, and I. C. Girit. *Beta Spectrum Studies with Cryogenic Micro-Calorimeters.* Journal of Low Temperature Physics. **93**(1993) 239–244.

[Lui93] A. Lui et al. *Technological Aspects Concerning the Realization of Ion Implanted Si-Bolometers.* Journal of Low Temperature Physics. **93**(1993) 331–336. (and additional private communication).

[Man94] P. D. Mannheim. *Microlensing, Newton-Einstein Gravity, and Conformal Gravity.* In *AIP Conference Proceedings 336: Dark Matter.* pages 505–508. October 1994.

[Mar93] H. J. Maris. *Phonon Physics and Low Temperature Detectors of Dark Matter.* Journal of Low Temperature Physics. **93**(1993) 355–364.

[Mar96] C. J. Martoff and X. X. Wang. *Discussions of Thermistor Performance.* private communication, Fall 1996.

[Mas94] D. Massé et al. *Further Investigation of Thermal Cryogenic Detectors in the Field of Ionizing Radiation Metrology.* Nuclear Instruments & Methods in Physics Research A. **339**(1994) 131–6.

[McC90] D. McCammon et al. *Thermal Detection of X-rays.* pages 213–225. Springer, Berlin, 1990.

[McC93] D. McCammon. *Optimization of Doped Silicon and Germanium Thermistors.* Journal of Low Temperature Physics. **93**(1993) 287.

[Mos84] S. H. Moseley, J. C. Mather, and D. McCammon. *Thermal Detectors as X-Ray Spectrometers.* Journal of Applied Physics, **56**(1984) 1257–62.

[Mot90] N. F. Mott. *Metal Insulator Transitions.* Taylor and Francis, London, second edition, 1990.

[Mou74] F. Mousty, P. Ostoja, and L. Passari. *Relationship between resistivity and phosphorous concentration in Silicon.* Journal of Applied Physics. **45**(1974) 4576–4580.

[Moy83] D. Moy and A. C. Anderson. *Use of a commercial metallic strain gauges as low temperature heaters.* Cryogenics. **23**(1983) 330–1.

[Mur93] T.P. Murphy. *Construction and Testing of a Novel Dilution Refrigerator.* Master's thesis, North Carolina State University, 1993.

[Nat94] National Instruments Corporation. *AT-MIO-16F-5 User Manual.* February 1994. Part Number 320266-01.

[Nat96a] National Instruments Corporation. *Labview User Manual*, January 1996. Part Number 321000A-01.

[Nat96b] National Instruments Corporation. *Labview User Manual*. January 1996. Part Number 320999A-01.

[Nel85] W. R. Nelson, H. Hirayama, and D. W. O. Rodgers. *EGS4 Users Manual.* (SLAC-265), December 1985.

[Ols93] J. R. Olson. *Thermal conductivity of some common cryostat materials between 0.05 and 2 K.* Cryogenics, **33**(1993) 729–31.

[ONe65] H. R. O'Neal and N. E. Phillips. *Low-Temperature Heat Capacities of Indium and Tin.* Physical Review. **137**(1965) A748–A759.

[PMI] PMI. *Ultra-Low Noise, Precision Operational Amplifier.* OP-27.

[Pob96] F. Pobell. *Matter and Methods at Low Temperatures.* Springer, Berlin, second edition, 1996.

[Pra95] N. Prantzos. *Primordial Nucleosynthesis.* In *Dark Matter in Cosmology Clocks and Tests of Fundumental Laws: Proceedings of the XXXth Rencontre De Moriond*, pages 3 – 11, January 1995.

[Pre93] K. Pretzl. *Superconducting Granule Detectors.* Journal of Low Temperature Physics. **93**(1993) 439–448.

[Ree94] M. J. Rees. *Introductory Survey.* In *AIP Conference Proceedings 336: Dark Matter*, pages 3–9. October 1994.

[Ric88] R. C. Richardson and E. N. Smith. *Experimental Techniques in Condensed Matter Physics at Low Temperatures.* Frontiers in Physics. Addison-Wesley Publishing Company. Inc.. Redwood City. 1988.

[Ros83] T. F. Rosenbaum et al. *Metal-insulator transition in a doped semiconductor.* Physical Review B. **27**(1983) 7509–23.

[Rot78] E. P. Roth, J. R. Matey. A. C. Anderson. and D. A. Johns. *Application of germanium resistance thermometers below 1 K.* Review of Scientific Instruments. **49**(1978) 813–816.

[Sad87] B. Sadoulet. *Cryogenic Detection of Particles, Development Effort in the United States.* In *Low Temperature Detectors for Neutrinos and Dark Matter*, pages 86–93. May 1987.

[Sha67] J. K. N. Sharma. *Heat Conductivities.* Cryogenics. **7**(1967) 141–56.

[Sim85] J. J. Simpson. *Evidence of Heavy-Neutrino Emission in Beta Decay.* Physical Review Letters. **54**(1985) 1891–1893.

[Sim87] R. E. Simpson. *Introductory Electronics for Scientists and Engineers.* Allyn and Bacon, Boston, second edition. 1987.

[Sta93] C. K. Stahle et al. *Thermalization of X-rays in Evaporated Tin and Bismuth Films Used as the Absorbing Materials in X-ray Calorimeters.* Journal of Low Temperature Physics. **93**(1993) 257–262.

[Sta97] C. K. Stahle and S. H. Moseley. *Discussions on the Response of Microcalorimeters using Tin Absorbers.* (Private communication), April 1997.

[Ste73] R. B. Stephens. *Low-Temperature Specific Heat and Thermal Conductivity of Noncystalline Dielectric Solids.* Physical Review B. **8**(1973) 2896–905.

[Sto70] E. Storm and H. I. Israel. *Photon Cross Sections from 1 keV to 100 MeV for Elements Z=1 to Z=100.* Nuclear Data Tables. **A7**(1970) 565–681.

[Sur91] B Sur et al. *Evidence for the Emission of a 17-keV Neutrino in the Beta Decay of ^{14}C.* Physical Review Letters. **66**(1991) 2444–7.

[Szy93] A. Szymkowaik et al. *Signal Processing for Microcalorimeters*. Journal of Low Temperature Physics, **93**(1993) 281–6.

[Wag94] T. Wagner, S. Götz, and G. Eska. *Thermal conductivity of wood at low temperatures*. Cryogenics, **34**(1994) 655–7.

[Wan93] X. X. Wang, C. J. Martoff, and E. Kaczanowicz. *All-Thin-Film GeAu Thermistors for Particle Detection*. Journal of Low Temperature Physics, **93**(1993) 349–354.

[Wan95] X. X. Wang. *Development of thin film Germanium-Gold Thermistors for Calorimetric Detection of Nuclear Radiation*. Ph.D. thesis, Temple University, June 1995.

[Whi79] G. K. White. *Experimental Techniques in Low-Temperature Physics*. Oxford University Press, New York, third edition, 1979.

[Wil67] J. Wilks. *The Properties of Liquid and Solid Helium*. Clarendon Press, Oxford, 1967.

[Wol91] S. Wolfram. *Mathmatica: A system for Doing Mathematics by Computer*. Addison-Wesley Publishing, Massachusetts, second edition, 1991.

[Wol97] Wolfram Research, Champaign, IL 61820. *TS 11181 –Re:Nonlinear Fit bug*, June 1997. Technical Suport Manual and additional private communication.

[Wu64] C. S. Wu. *The Universal Fermi Interaction and the Conserved Vector Current in Beta Decay*. Review of Modern Physics, **36**(1964) 618–632.

[Wu66] C. S. Wu and S. A. Moszkowski. *Beta Decay. Volume XVI of Monographs and Texts in Physics and Astronomy*. Interscience Publishers (Wiley & Sons), New York, 1966.

[Zem81] M. W. Zemansky and R. H. Dittman. *Heat and Thermodynamics*. McGraw-Hill Book Company, New York, sixth edition, 1981.